

LITHOLOGIC, CLIMATIC, AND BIOTIC VS. ABIOTIC CONTROLS ON
EROSION AND LANDSCAPE EVOLUTION

by

JILL ANN MARSHALL

A DISSERTATION

Presented to the Department of Geological Sciences
and the Graduate School of the University of Oregon
in partial fulfillment of the requirements
for the degree of
Doctor of Philosophy

June 2015

DISSERTATION APPROVAL PAGE

Student: Jill Ann Marshall

Title: Lithologic, Climatic, and Biotic vs. Abiotic Controls on Erosion and Landscape Evolution

This dissertation has been accepted and approved in partial fulfillment of the requirements for the Doctor of Philosophy degree in the Department of Geological Sciences by:

Joshua J. Roering	Chairperson
Rebecca J. Dorsey	Core Member
John M. Logan	Core Member
Daniel G. Gavin	Institutional Representative

and

Scott L. Pratt	Dean of the Graduate School
----------------	-----------------------------

Original approval signatures are on file with the University of Oregon Graduate School.

Degree awarded June 2015

© 2015 Jill Ann Marshall

DISSERTATION ABSTRACT

Jill Ann Marshall

Doctor of Philosophy

Department of Geological Sciences

June 2015

Title: Lithologic, Climatic, and Biotic vs. Abiotic Controls on Erosion and Landscape Evolution

The triumvirate of tectonics, lithology, and climate control landscape evolution. This study quantifies how lithologic variation and climate-mediated changes in ecosystems perturb steady state processes in the unglaciated, soil-mantled Oregon Coast Range (OCR). I first demonstrate that minor grain-scale differences in rock properties in a seemingly uniform sandstone control differences in rock strength, biotic bedrock-to-soil production efficacy and erosion rates and influence relief at the watershed scale. I then build on sedimentology, paleoecology, and isotopic-derived paleoerosion data I collected from a new 50 ka sediment archive at Little Lake, OR to explore climate controls on soil production and erosion rates 21 ka across the OCR and spanning 50 ky within a single watershed. In Chapter III, I combine a mechanistic frost weathering model with a regional Last Glacial Maximum (LGM) climate reconstruction and paleovegetation data to demonstrate that accelerated frost-driven erosion was pervasive across the OCR during the LGM. My findings provide a new framework to quantify how the late Pleistocene affects modern erosion and soil formation rates in unglaciated environments and implies that most landscapes reside in a transient state. In Chapter IV, I document climate-mediated ecosystem influence on erosion rates over 3 climatic intervals. ¹⁰Be-derived

erosion rates increase 3x (from 0.6 mm/yr to 0.21 mm/yr) as the OCR transitioned from the open forest-dominated Marine Isotope Stage (MIS) 3 climate interval (50-26 ka) into the periglacial subalpine MIS 2 glacial interval (26-13 ka). Measured erosion rates fell by more than half as the subalpine ecosystem gave way to the modern MIS 1 closed canopy Douglas-fir forest. Coupling paleovegetation-derived climate information with core observations I model frost weathering intensity from ~ 43 ka to 21 ka and establish a correspondence with increasing frost weathering intensity and increasing ¹⁰Be-derived erosion rates. Utilizing a transient mixing depth and erosion rate model, I am able to broadly replicate measured erosion rates at Little Lake through time. My findings contradict previous work that suggests climate has only weak control on erosion rates.

This dissertation includes previously published and unpublished co-authored material.

CURRICULUM VITAE

NAME OF AUTHOR: Jill Ann Marshall

GRADUATE AND UNDERGRADUATE SCHOOLS ATTENDED:

University of Oregon, Eugene
San Francisco State University, San Francisco, CA
California State University, East Bay, Hayward

DEGREES AWARDED:

Doctor of Philosophy, Geosciences, 2015, University of Oregon
Master of Science, Geosciences, 2009, San Francisco State University
Bachelor of Science, Geosciences, 1995, California State University, East Bay

AREAS OF SPECIAL INTEREST:

Geomorphology

PROFESSIONAL EXPERIENCE:

Graduate Teaching & Research Fellow, University of Oregon, 2010-2015

Geomorphologist/Engineering Geologist, California Water Quality Control Board, 2000-2009 (variable time)

River Science Coordinator, California Bay Delta Program (CALFED) Science Program, Sacramento CA, 2000-2005 (variable time)

Fluvial Geomorphologist, Urban Creeks Council, 1999-2000

Engineering Geologist/Environmental Specialist, California Water Quality Control Board, 1994-1999

GRANTS, AWARDS, AND HONORS:

Service Award, University of Oregon, 2014

Critical Zone Observatory International Scholar, NSF-International Programs-Europe, 2012

Weiser Scholarship, University of Oregon, 2009

National Center for Airborne Laser Mapping, Graduate Student Seed LiDAR, 2007

Outstanding Student Presentation Award, American Geophysical Union Fall Meeting, 2007

Outstanding Student Presentation Award, American Geophysical Union Fall Meeting, 2007

National Fish and Wildlife Foundation, Budweiser Conservation Scholarship, 2007

PUBLICATIONS:

Harpold, A. A., **J. A. Marshall**, S. W. Lyon, T. B. Barnhart, B. Fisher, M. Donovan, K. M. Brubaker, . . . N. West, (accepted for publication), Laser Vision: Lidar as a transformative tool to advance Critical Zone science, Hydrology and Earth System Sciences

Marshall, J.A., and J.J. Roering (2014), Diagenetic variation in the Oregon Coast Range: Implications for rock strength, soil production, hillslope form, and landscape evolution, *Journal of Geophysical Research - Earth Surface*, 119, 1395–1417, doi: 10.1002/2013JF003004.

Roering, J.J., B.H. Mackey, **J.A. Marshall**, K. Sweeney, A.M. Booth, N. Deligne, A.M. Handwerker, and C. Cerovski-Darriau, (2013), 'You are HERE': Connecting the dots with airborne lidar for geomorphic fieldwork, *Geomorphology*, 2012 Binghamton Symposium, "The Field Tradition in Geomorphology", doi: 10.10106/j.geomorph.2013.04.009.

Marshall, J.A. and L.S. Sklar (2012), Mining soil databases for landscape-scale patterns in the abundance and size distribution of hillslope rock fragments, *Earth Surface Processes and Landforms*, 37(3), 287-300, doi: 10.1002/esp.2241.

Roering, J., **J. Marshall**, A.M. Booth, M. Mort, and Q. Jin (2010), Evidence for biotic controls on topography and soil production, *Earth and Planetary Science Letters*, v. 298, p. 183-190, doi: 10.1016/j.epsl.2010.07.040.

Marshall, J. A., P. DeVries, and N. Milner (2008), Spawning habitat remediation as part of national and regional scale programs to recover declining salmonid populations. (pp 275 – 300), in *Salmon spawning habitat in rivers: physical controls, biological responses and approaches to remediation*, edited by P. DeVries and D. Sears, American Fisheries Society, Symposium 65. Bethesda, MD.

Marshall J. (2003), Moving from the past into the future: a functional approach for protecting California streams. in P.M. Faber (ed.) California riparian systems: Processes and floodplain management, ecology, and restoration (pp. 158-162). Riparian Habitat and Floodplains Conference Proceedings, Riparian Habitat Joint Venture, Sacramento

ACKNOWLEDGMENTS

I am thankful for the support of many mentors, colleagues, friends and family members, without whom this dissertation and the underlying scholarly pursuit would surely have been diminished. Foremost I thank my advisor, Josh Roering, for placing few limits on my curiosity, encouraging me to exceed my perceived limits, and serving as an exemplar rigorous and kind scholar. Many thanks to the rest of my committee members Dan Gavin, Becky Dorsey and John Logan, each of whom provided critical advice and counsel. Thanks in particular to Dan Gavin for welcoming me to the world of paleoecology and providing me with an enhanced way to view earth processes.

My parents, Grace Goldberg and David Marshall (nee Goldberg) encouraged my propensity for curiosity and scholarship and for this I will always be in their debt. The familial support continued with my second mother, Betty Marshall and extends to my entire family. Numerous friends provided encouragement, love, and graduate student support. In particular I want to thank Kim Taylor, Bob and Linda Spencer, Bruce Orr, Lisa Nelowet, Angie Thompson, and Carol Holt for their rock solid support, guidance, and clarifying advice over the years, plus the time spent in non- scholastic pursuit of happiness.

I could not have wished for a better, more supportive environment than I received during my time at the University of Oregon. Thanks to my wonderful cohorts in the Roering Lab group. In particular discussions and field time with Adam Booth, Alex Handwerger, Corina Cerovski-Darriau, Kristin Sweeney and Georgie Bennett enhanced and expanded this dissertation, and my overall knowledge. The entire Department of

Geosciences from faculty to the administrative staff to my graduate student cohort contributed to a wonderful joyful five plus years.

The work was supported by a National Science Foundation award, NSF EAR-0952186, to Josh Roering and Dan Gavin.

TABLE OF CONTENTS

Chapter	Page
I. INTRODUCTION.....	1
II. DIAGENETIC VARIATION IN THE OREGON COAST RANGE: IMPLICATIONS FOR ROCK STRENGTH, SOIL PRODUCTION, HILLSLOPE FORM, AND LANDSCAPE EVOLUTION.....	3
1. Introduction.....	3
2. Study Area: Sink to Source to Sink	7
3. Methods.....	12
4. Results.....	18
5. Discussion.....	32
6. Conclusions.....	40
7. Bridge.....	40
III. FROST, NOT PRECIPITATION, DROVE INCREASED EROSION IN UNGLACIATED TERRAIN 21,000 YEARS AGO.....	42
1. Seeking the Elusive Signature of Glacial Intervals in Unglaci- ated Terrain	42
2. Little Lake Sediment Core Results	44
3. Accelerated Sediment Production Due to Frost Weathering Rather than Precipitation	44
4. Conclusions.....	49
5. Materials and Methods.....	49
6. Bridge.....	52

Chapter	Page
IV. LATE QUATERNARY CLIMATIC CONTROLS ON ECOSYSTEMS, PROCESSES, AND EROSION RATES OVER MILLENNIAL TIME SCALES IN THE PACIFIC NORTHWEST.....	53
1. Introduction.....	53
2. Background.....	54
3. Geographic Setting and Previous Studies.....	60
4. Methods.....	64
5. Theoretical Framework – Measured vs. Actual ¹⁰ Be-Derived Erosion Rates ...	71
6. Results.....	77
7. Discussion.....	84
8. Conclusions.....	96
APPENDICES	
A. SUPPLEMENTARY MATERIAL FOR CHAPTER II.....	98
B. SUPPLEMENTARY MATERIAL FOR CHAPTER III.....	101
REFERENCES CITED.....	111

LIST OF FIGURES

Figure	Page
2-1. Lidar-derived gradient map of Harvey and Franklin Watersheds	5
2-2. Conceptual model illustrating the Oregon Coast Range delta-fed submarine ramp setting.	10
2-3. Petrology and tensile strength test results	19
2-4. Hillslope gradient probability density functions	21
2-5. Channel longitudinal profiles and χ plots	23
2-6. Slope-drainage area plots	24
2-7. Valley width vs. drainage area	26
2-8. Functional relationship between dimensionless relief.....	27
2-9. Topographic profiles and power spectra	29
2-10. Relief comparison.....	31
2-11. Mean relief vs. fraction of resistant beds.....	32
3-1. Map showing extent of ice sheets 21 ka, study area and Little Lake, OR.....	43
3-2. Comparison of annual temperature curves based on mean monthly temperature data	45
3-3. Model output of frost cracking intensity	47
3-4. Maps showing elevation, MAT, annual amplitude and frost cracking intensity 21 ka	48
4-1. Little Lake catchment and sample sites.....	59
4-2. Models of cosmogenic nuclide accumulation and loss in vertically well-mixed soils	72
4-3. Model applying the transient solution for nuclide-derived erosion rates.....	77
4-4. Compilation of Little Lake core observations and data.....	78

Figure	Page
4-5. Depth-age model based on ^{14}C and OSL dates	81
4-6. Little Lake ^{10}Be -derived erosion rates vs. time	83
4-7. Comparison of annual temperature curves	88
4-8. Frost cracking intensity and paleoclimate reconstructions.....	89
4-9. Transient erosion rate and mixing model output.....	94
4-10. Climate fluctuations over the last 400 ka.	96

LIST OF TABLES

Table	Page
4-1. ^{14}C data	67
4-2. OSL data and calculated ages.....	68
4-3. Cosmogenic nuclide data and calculated erosion rates	69

CHAPTER I

INTRODUCTION

The Critical Zone, often described as the thin terrestrial skin of the earth, is where water and rock meet life. This near-surface zone is deemed critical due to the ecosystem services it supplies (e.g. carbon storage, soil development, terrestrial and aquatic habitat and hydrologic metering) as well as the import as a framework for quantifying the interplay of biotic and abiotic processes in shaping landscapes over multiple temporal and spatial scales. Embedded in this general description is the role rock properties and climate-mediated controls on ecosystems exert over both modern and longer scale landscape evolution. In this dissertation, I seek to quantify the role of rock properties and climate in modulating the mechanisms that convert bedrock to soil, control erosion rates and thus control landscape evolution.

While lithology is often invoked as a control on landscape processes, the invocation implies that rock properties such as porosity, permeability, grain size, and material strength are uniform within each lithology. Lithology in principle is an attractive analogue for rock properties, with expectations of weak mudstones and shales when compared to strong granites and basalts. However, in reality, variations in material properties and fractures or weathering imposed by difference in petrology and tectonic or climatic regimes may control rock properties variability such that lithology is a poor descriptor of rock property control on landscape processes.

The second chapter, co-authored with Dr. Josh Roering and published in the *Journal of Geophysical Research – Earth Surface* demonstrates how lithologic variability within a single sandstone formation modulates geomorphic processes from the meter to landscape scale. This work provides a framework to quantify how seemingly subtle variations in rock properties can impose first-order controls on landscape form and evolution.

In Chapters III and IV, I explore the role of climate change on bedrock weathering mechanisms and erosion rates over glacial and interglacial intervals in the soil-mantled unglaciated Oregon Coast Range. The third chapter was co-authored with Dr. Josh Roering, Dr. Dan Gavin, Dr. Pat Bartlein, Dr. Darryl Granger, Dr. Alan Rempel,

Dr. Sarah Praskievicz, and Dr. T.C. Hales and is currently submitted to the journal *Science Advances*. In this interdisciplinary contribution, by combining a mechanistic frost weathering model with a regional Last Glacial Maximum (LGM) climate reconstruction derived from a paleo-Earth System Model, paleovegetation data, and a paleoerosion archive, I demonstrate that frost-driven sediment production was pervasive during the LGM in our unglaciated Pacific Northwest study site, coincident with a 2.5x increase in erosion relative to modern rates. The findings provide a new framework to quantify how the late Pleistocene affects modern erosion and soil formation rates in unglaciated environments and implies that many landscapes reside in a transient state.

The final chapter, coauthored with Dr. Josh Roering, Dr. Dan Gavin, and Dr. Darryl Granger demonstrates that erosion rate changes track changes in climatic intervals over the past 50 ky. Importantly, ^{10}Be -derived erosion rates increase 3x (from 0.6 mm/yr to 0.21 mm/yr) as the OCR transitioned from the open forest-dominated MIS climate interval (50-26 ka) into the periglacial subalpine MIS 2 glacial interval (26-13 ka) and LGM erosion rates are $\sim 2.5x$ greater than modern erosion rates in the Little Lake Basin. While other studies have shown only weak climatic influence on erosion rates it is challenging and potentially problematic to use a space-for-time substitution framework to infer climate controls on geomorphic change, as this study demonstrates. Our findings encourage a re-evaluation of what constitutes steady state in soil-mantled unglaciated settings. Importantly, lengthy glacial intervals with their highly efficient abiotic erosion mechanisms relative to short interglacial intervals and biotic-driven erosion mechanisms may be the ultimate pacesetters controlling landscape evolution in unglaciated terrain.

This work contributes to a mechanistic understanding of how variations in rock properties and climate-mediated processes control erosion rates and important Critical Zone attributes such as architecture and soil sustainability.

CHAPTER I

DIAGENETIC VARIATION IN THE OREGON COAST RANGE: IMPLICATIONS FOR ROCK STRENGTH, SOIL PRODUCTION, HILLSLOPE FORM, AND LANDSCAPE EVOLUTION

Reproduced with permission from Marshall, J. A., and J. J. Roering (2014), Diagenetic variation in the Oregon Coast Range: Implications for rock strength, soil production, hillslope form, and landscape evolution, *J. Geophys. Res. Earth Surf.*, 119, 1395–1417, doi:10.1002/2013JF003004. Copyright 2014, American Geophysical Union.

1. INTRODUCTION

In addition to tectonics and climate, it is oft-stated that lithology is a fundamental control on landscape evolution. Intuitively, we expect that harder rock will resist erosion such that all else being equal, harder rock will tend to produce steeper slopes. This simple observation is not limited to those with geologic expertise as non-scientists frequently surmise that rock hardness shapes landscapes. When Nathaniel Hawthorne [1854], an American novelist of the 17th century, wrote: “Mountains are Earth’s undecaying monuments”, he captured the concept that harder rock endures and underlies the Earth’s rugged high points. In the scientific literature, *G.K. Gilbert* [1877], in his seminal work on the Henry Mountains, conceptualized process laws to describe observed patterns in landscape concavities, declivities, and divides, but he also noted how hard rocks caused deviations from these patterns. Strictly speaking, Gilbert observed that the main factors that control erosion rates are declivity (gradient), climate, and the character of the rock, with softer rocks weathering more rapidly than hard ones. Of Mt. Ellsworth, Gilbert noted that the mountain “survives the general degradation of the country only in virtue of its firmer rock masses.” While lithologic control on landscape evolution has been noted by many observers, functional relationships between rock properties, geomorphic processes, and landscape form have seldom been tested, and surprisingly little progress

has been made since Gilbert first penned his observations on hard rock, weathering, and topographic form.

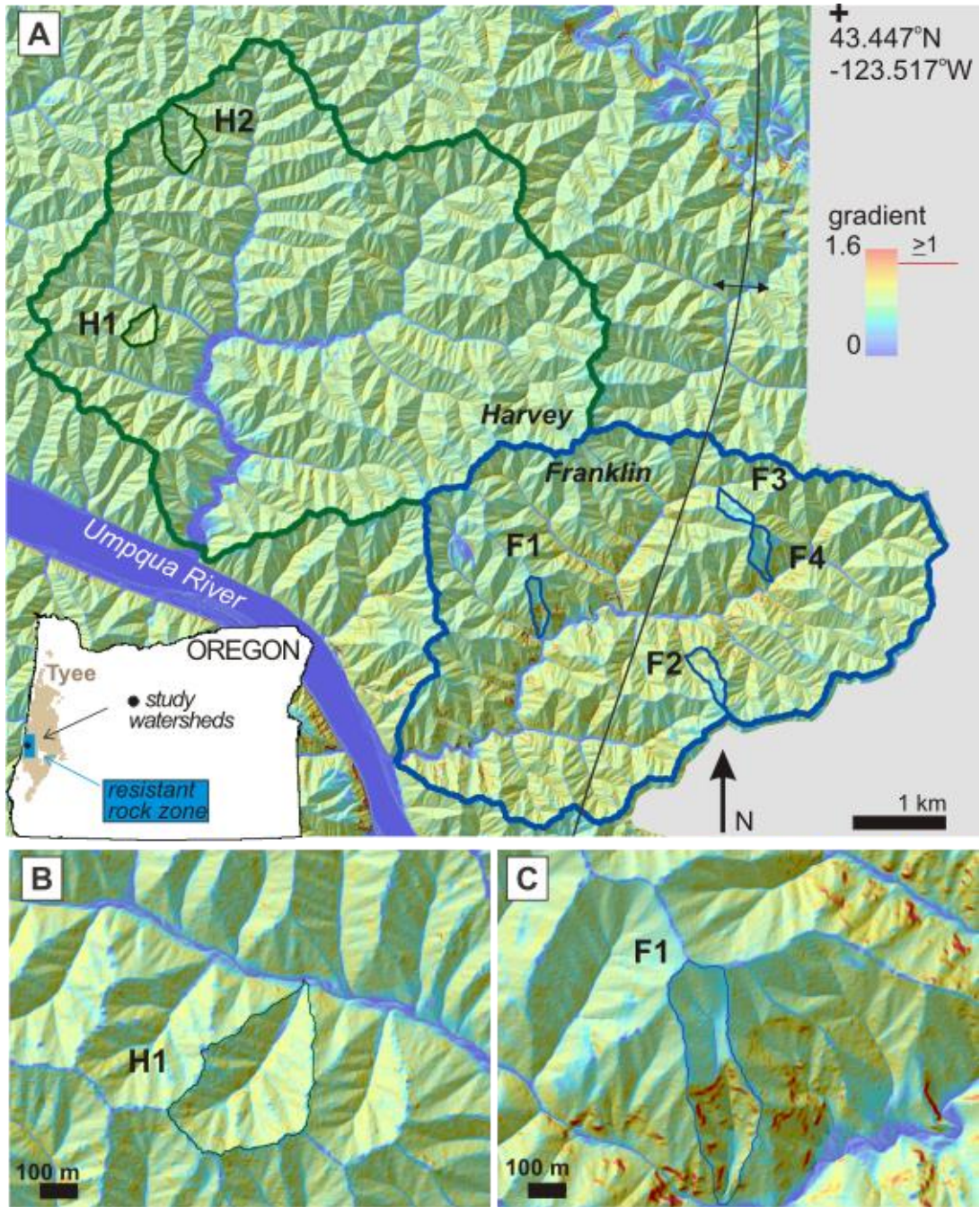
Rock strength indices, including strength tests (e.g., Schmidt hammers) and other proxies based on lithologic classification and fracture characteristics [e.g., *Selby*, 1993], have been used to explain rock controls on hillslope relief [*Schmidt and Montgomery*, 1995], landslide frequency and magnitude [*Korup*, 2008; *Clarke and Burbank*, 2010], alpine cliff retreat rates [*Moore et al.*, 2009], topographic metrics [*Hurst et al.*, 2013b], and basin sediment yield [*Aalto et al.*, 2006]. With the exception of *Aalto et al.* [2006], who adapted a lithologic index for sediment yield data, a framework for making predictions and parameterizing models based on these studies is lacking and few studies have analyzed variations within a given watershed to better constrain the role of rock properties. *Hack* [1957, 1973] recognized the role of a resistant quartzite ridge in ‘propping up’ local Appalachian base level thus leading to changes in channel profile form. *Ahnert* [1987] inserted zones of resistant rock within a 1D-hillslope evolution model and concluded that denudation rates must exceed the resistant rock weathering rates to influence hillslope form. By contrast, measured soil production rates can vary widely with depth and rock hardness, suggesting a more complex relationship between hillslope weathering processes, bedrock strength, and form [*Heimsath et al.*, 2001].

Duvall et al. [2004] collected over 1000 Schmidt hammer measurements in channels crossing both resistant and non-resistant sedimentary units and found channel concavity and steepness index values exceeding those predicted by the stream incision model for streams without lithologic variation. Using a Schmidt hammer, *Stock and Dietrich* [2006] documented along-channel strength variations related to rock properties, weathering, and debris flow frequency. *Allen et al.* [2013] used a Schmidt hammer, hand compression and hammer blows to estimate rock strength in rivers along the Himalayan front crossing weak to resistant lithologic units and found that substrate strength influences channel form and width, with narrow channels forming upstream of resistant knickpoints. Surprisingly, none of these studies explored the actual rock properties that facilitated these geomorphic patterns, and few questioned the degree to which lithologic variation modulates landscape evolution. As a result, we have little predictive capability to foresee when rock property contrasts become geomorphically relevant.

Spatially extensive high-resolution (~1 m) digital elevation models (DEMs) are increasingly being used to evaluate hypotheses on functional relationships between form and process [e.g. *Heimsath et al.*, 1997; *Dietrich et al.*, 2003; *Roering et al.*, 2007; *Roering*, 2008; *Perron et al.*, 2009; *Gabet and Mudd*, 2010; *Hurst et al.*, 2012], ecosystem services [*May et al.*, 2013], and the signature of soil production mechanisms [*Roering et al.*, 2010]. However, process models in use since the 1990s [e.g. *Dietrich et al.*, 2003] typically ignore lithologic variations when considering attributes that control bedrock to soil conversion or denudation. In reality, as every geologist learns after placing nose to rock, when we step away from our maps and modeled landscapes and into the field, apparently uniform bedrock often varies in ways both obvious and subtle, ranging from visible differences in fracture density or grain size, to microscopic petrologic variations. Thus, it is worth asking - when applying geomorphic process laws - is it appropriate to ignore lithologic variations?

In this study, we focus on two adjoining watersheds, within a single geologic unit, in the central portion of the well-studied Oregon Coast Range (Figure 2-1). We explore how previously discounted variations in rock properties control geomorphic processes and thus landscape evolution. Regionally, patches of unfractured, unvegetated rock, characterized by loggers as ‘bedrock meadows’, ecologists as ‘rocky balds’ [e.g. *Aldrich*, 1972; *Franklin and Dryness*, 1988], and land managers as ‘non-timber producing patches’ crop out amongst the soil-mantled, closed-canopy fir forests of the Oregon Coast Range. We first describe the geologic and depositional setting responsible for producing

Figure 2-1 (next page). A) Lidar-derived gradient map of Harvey and Franklin watersheds with individual study catchments identified for Harvey watershed in green and with H-identifiers and for Franklin watershed in blue with F-identifiers. Resistant rock beds are defined as having a gradient ≥ 1 (100%) and are delineated by red tones on the map. Approximate location of anticline axis is described by thin curved line bisecting Franklin watershed from NW to SSE. Inset map delineates the extent of the Tyee Formation in tan, the general extent of resistant beds in blue and a closed circle marks the study area location. B) Close-up of Harvey catchments, including H1 catchment outlined in green on the gradient map. Note the topography, with catchments of uniform size and shapes with well-ordered drainage networks. C) Close-up of Franklin catchments, including the F1 catchment outlined in blue on the gradient map. Note the dis-organized topography, with low-gradient basins perched above the red bands defining resistant rock beds, varied sized and shaped catchments, and variable valley density. ‘Typical’ Tyee bedrock underlies the soil-mantled basins perched above the resistant rock beds.



variations in rock properties. We then present observations and analyses from fieldwork, petrology, rock mechanics, and airborne lidar to characterize differences in rock properties, geomorphic processes, and topographic attributes. This paper explores how minor, grain-scale differences in rock properties that account for a relatively small percentage of hillslope length and occur discontinuously throughout a watershed can

modulate bedrock-to-soil conversion processes, channel form and incision rates, sub-catchment erosion rates, and catchment-scale relief.

2. STUDY AREA: SINK TO SOURCE TO SINK

2.1. The Oregon Coast Range - geologic setting

Our study area watersheds, Franklin and Harvey, are located in the central Oregon Coast Range and drain directly into the Umpqua River just west of Scottsburg. The Oregon Coast Range (OCR) is an unglaciated, humid soil-mantled landscape characterized by steep, highly dissected mountains [*Dietrich and Dunne, 1978, Reneau and Dietrich, 1991*]. The underlying deposits of the Eocene Tye basin include trench and rift margin sediments and overlying forearc basin fill deposits that accumulated as the region transitioned from a dominantly convergent tectonic regime to a broad forearc basin. The Tye Formation also includes overlying delta deposits commensurate with a reduction in sedimentation rates during the late Oligocene growth of the Cascade volcanic arc [*Heller et al., 1987; Ryu and Niem, 1999*]. The rhythmically bedded Eocene turbidity deposits of the Tye Formation overly a thick accreted volcanic basement termed Siletzia [*Orr et al., 1992*]. The Tye Formation extends over 10,000 km² and has been studied in detail due to its distinct, well exposed assemblage of sedimentary facies [*Snively et al., 1964; Heller and Ryberg, 1983; Heller and Dickinson, 1985; Lovell, 1969b*] and reservoir potential [*Rogers, 1969; Ryu and Niem, 1999*]. The turbidite beds formed from a series of delta-fed channels at the base of submarine ramps along the continental slope such that lateral (east- west) and facies variability is minimal [*Heller and Dickinson, 1985*]. The lithology is remarkably uniform [e.g. *Snively et al., 1964; Dott Jr, 1966; Lovell, 1969b*] with a proximal to distal, south to north reduction in formation thickness and sand to siltstone ratio [*Lovell, 1969a*]. The ~3 km thick formation [*Snively et al., 1964*] contains sand-rich, arkosic lithic material sourced from the Idaho batholith, mixed with immature volcanoclastics from the Klamath Mountains [*Heller and Ryberg, 1983; Heller et al., 1985*]. Clockwise basin rotation of more than 50° has occurred since the middle Eocene [*Simpson and Cox, 1977; Wells and Heller, 1988*]. The OCR is currently undergoing east-west oriented compression due to ongoing

subduction and forearc rotation and has been deformed into a series of gentle folds trending NE to SW with beds dipping 4 to 10 degrees along fold flanks [Baldwin, 1961].

2.2. Rock uplift and erosion rates in the Oregon Coast Range

The Oregon Coast Range has been proposed to approximate steady state [e.g. *Reneau and Dietrich*, 1991; *Montgomery*, 2001; *Roering et al.*, 2007] as numerous studies suggest that long-term erosion rates [e.g. *Bierman et al.*, 2001; *Heimsath et al.*, 2001] approximately balance rates of rock uplift [Kelsey et al., 1994]. Long-term coastal uplift rates derived from shore platform surveys range between 0.05 to 0.3 mm yr⁻¹ over the last 100 kyr [Kelsey et al., 1994]. Millennial-scale OCR erosion rates, derived from cosmogenic nuclides, range from 0.03 to 0.3 mm yr⁻¹ for hillslopes and from 0.11 to 0.14 mm yr⁻¹ for basin-averaged erosion rates via stream sediments [Bierman et al., 2001; Heimsath et al., 2001]. *Reneau and Dietrich* [1991] analyzed colluvial hollows and estimated hillslope erosion rates of 0.07 mm yr⁻¹ and bedrock exfoliation rates of 0.09 mm yr⁻¹ over the last 4,000 to 15,000 years. Short-term erosion rates derived from river sediment yields range from 0.07 to 0.19 mm yr⁻¹ [Wheatcroft and Sommerfield, 2005]. Together, these findings suggest that the average lowering rate of approximately 0.1 mm yr⁻¹ is broadly consistent with rock uplift rates across the Oregon Coast Range over 1,000-yr timescales. However, there is scant theory constraining how rock properties, which can present in a watershed as knickpoints [Stock et al., 2005], rocky balds [e.g. Aldrich 1972], or resistant cliffs [Chan and Dott, 1983], may modulate erosion rates.

2.3. Pacific Northwest forearc sedimentary units - diagenetic processes, products, and rock properties

Understanding controls on bedrock composition and mechanical behavior is critical for unraveling how anomalous landform patterns and dynamics emerge in the absence of climate and/or tectonic variations. Our observations and previous contributions [e.g. *Lovell and Rogers*, 1969; *Galloway*, 1974; *Heller et al.*, 1985; *Ryu and Niem*, 1999] suggest that the Tyee Basin source rock and subsequent diagenetic processes influence rock composition. As such, an examination of sedimentary architecture, burial history, and diagenesis, will presumably enable us characterize and predict bedrock

exhumation patterns as well as implications for landscape evolution at the local and regional scale.

Sandy turbidite deposits sourced from immature volcanoclastic sediments along the Cascadia margin have been well-studied for their characteristic diagenetic sequences [e.g. *Galloway*, 1974, 1979; *Ryu and Niem*, 1999]. Diagenetic alteration products are a function of the complex interplay between source minerals, depositional setting (e.g. shallow delta systems, submarine turbidity deposits on a continental shelf, or distal deepwater fan deposits), fluid flow and burial depth [*Hutcheon*, 1993]. *Galloway* [1974, 1979] described three progressive stages of diagenesis based on shallow to moderate burial depth within the terrigenous and volcanic clastic deposits of the northeast Pacific arc-related basins. *Ryu and Niem* [1999] extended the diagenetic sequence to the Tye forearc depositional system; the three progressive stages of diagenesis include: 1) calcite and calcite cement, 2) authogenic clay coats and rims, and 3) pore-filling zeolite cements (Figure 2-2). The authogenic clays include mixed layer chlorite/smectite (corrensite), which is compositionally related to palygorskite and sepiolite [*Weaver*, 2000], fibrous rimming clays mined industrially for their binding strength [*Galan*, 1996]. While matrix-filling clays tend to reduce rock strength [*Al-Tahini et al.*, 2006], overgrowth (rimming) fibrous clays as we describe here, often increase rock strength [*Yatsu*, 1971, 1988; *Al-Tahini et al.*, 2006].

2.4. Local petrology, mineralogy and depositional setting

Previous petrology and mineralogy studies in the OCR noted the presence of rock strengthening or fibrous minerals in a zone extending from just north of Roseburg (latitude 43°) to Eugene, OR (latitude 44°), a region that roughly corresponds with the coarse-bedded slope and proximal ramp deposits of the Tye [*Heller and Dickinson*, 1985]. Below, we consider the Pacific Northwest diagenetic phase model [*Galloway*, 1974, 1979; *Ryu and Niem*, 1999] in conjunction with several references describing patches of anomalous chlorite- calcite-rich, fibrous clays, and resistant rock beds found in a 100-km swath in the southwest portion of the Tye formation (inset Figure 2-1a). Together, this information provides a regional context for diagenetically-driven resistant

bedrock in the OCR and allows us to constrain the spatial extent of potential morphologic and process effects.

Lovell [1969b] found no significant regional or local variation in the Tye mineralogy with the exception of authogenic chlorite, but this does not preclude variations in minor secondary authogenic alteration products, oft- noted, but deemed unimportant to petrologic studies [e.g. *Lovell*, 1969b]. From a petrologist's point of view these are minor differences, while from a geomorphologist's point of view, the resulting difference within a single formation may be as profound as a difference in lithology in terms of controlling rock properties and thus geomorphic function. These diagenetic artifacts include chlorite and calcite, which grade with depth into later phases of authogenic calcite cements, rimming clays, clinoptiolite and laumontite (Figure 2-2) [*Galloway*, 1974; *Chan*, 1985; *Ryu and Niem*, 1999].

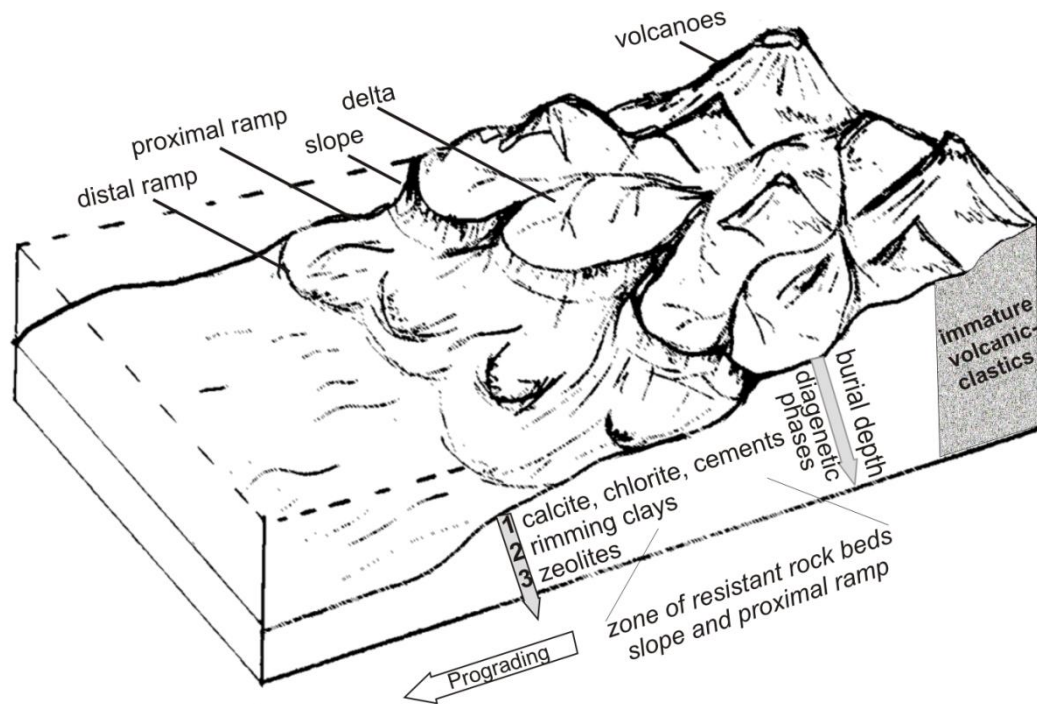


Figure 2-2. Conceptual model illustrating the Oregon Coast Range delta-fed submarine ramp setting during initial Eocene turbidite deposition along with the diagenetic phases found in the sand-rich slope and proximal ramp deposits underlying Franklin and Harvey watersheds. Figure based on Heller and Dickinson [1985] and Richards et al. [1997].

Tyee samples collected to the west of Roseburg, Oregon, commonly have a chlorite matrix and many have a radiating fibrous structure [Rogers and Richardson, 1964] suggestive of the rimming corrensite clays or the zeolite pore fill described by Ryu and Niem [1999]. Similarly, waterfall-forming Tyee sandstone beds in the South Coquille River (south of our study area) contain a fibrous authogenic mineral formed interstitially by the alteration of coarse volcanic grains [Dott Jr., 1966]. In addition, calcite cemented beds occur locally [Snively et al., 1964; Lovell, 1969a, b; Stock and Dietrich, 2006] in the ‘Smith River section’ deposits. Carbonate concretions are found in 23% of the sandstone beds in the Smith River section [Lovell, 1969a], which encompasses the watersheds that are the focus of this study. Nowhere else in the Tyee Formation is authogenic carbonate found in more than 4% of the beds sampled [Lovell, 1969a]. Taken together, these studies suggest a well-defined zone for the resistant bed occurrence extending from 43°N to 44°N with a vertical extent limited by diagenetic phase zones (Inset Figure 2-1a). The extent of the resistant beds should migrate northward as deeper sections of the unit are exposed, tracking the delta submarine ramp deposition progression through time.

2.5. Geologic structure and resistant beds in Franklin and Harvey watersheds

In our central OCR study area, the Harvey and Franklin watersheds present an ideal opportunity to characterize the influence of variable rock properties, specifically rock strength, on landscape processes at the local (outcrop) to watershed scale, as meter-scale bands of diagenetically-derived cliff-forming resistant rock, previously masked by surrounding dense vegetation, are now easily mapped using airborne lidar. The two watersheds occur within the Tyee Formation, are similarly orientated, and experience similar climatic and tectonic controls. Comprised primarily of massive sandstone turbidite beds of variable thickness (ranging from ~ 1 to 10 m), with minimal siltstone innerbeds, both Franklin and Harvey watershed stratigraphy exemplify turbidity deposits formed in the proximal region of a submarine ramp setting (Figure 2-2) [Heller and Dickinson, 1985]. Structurally, a broad (>1km) anticline defines the region, with a minor fold axis trending N-NNE superimposed on the larger broad anticline. As the beds dip gently (~ 4-6°) away from the fold, resistant beds exposed in the Franklin Creek

watershed have yet to be exhumed in the adjoining Harvey watershed to the west (Figure 2-1). Resistant cliff-forming rock beds ranging from a meter to tens of meters in thickness crop out in Franklin and extend into the eastern side of Harvey watershed. The beds are massive with a mean vertical fracture spacing of 12.9 ± 1.7 m (mean \pm std err) compared to the mean vertical fracture spacing of 0.6 ± 0.02 m (mean \pm std err) for the ‘typical’ Tyee (Figure 2-S1, 2-S2). The beds are horizontally continuous but not contiguous. The resistant beds form knickpoints within the mainstem channel of Franklin Creek and at varying elevations in tributaries. In general, resistant beds crop out at increasingly higher points in the drainage network moving from north to south (Figure 2-1).

3. METHODS

3.1. Rock properties: petrographic and mechanical strength

To characterize rock properties in the resistant and typical sandstone we collected in-situ samples using a combination of sledges, rock hammers, and a diamond-bit corer. For petrographic analysis, we used thin sections for standard and polarized microscopy as well as SEM (scanning electron microscopy) for energy-dispersive X-ray spectrometry (EDS) line scanning and 2D mapping. We also infused all thin sections with blue epoxy to quantify variations in porosity. We estimated rock strength using two types of tensile failure tests, point load and Brazilian splitting tests. While both of these procedures measure tensile strength, the values differ depending on the testing procedure, and therefore the results are best interpreted as indexes of strength [*Butenuth, 1997*].

3.2. Topographic characterization

3.2.1. Lidar data and topographic noise

Our lidar-based topographic analysis of lithologic controls on landscape form used different methods to characterize topographic metrics depending on the process regime (e.g., hillslope vs. valley) and scale. Our analysis of airborne lidar data (acquired by Oregon Department of Geology and Mineral Industries) required smoothing of the 1x1 m gridded bare earth dataset. Noise in the bare earth data arises from two sources: 1) errors in point classification, and 2) natural topographic roughness associated with tree

throw pit and mounds, animal mounds, sediment piles, and large woody debris jams. In the OCR, the topographic signature of pit and mound features from tree turnover dominates at length scales < 7.5 m [Roering *et al.*, 2010]. Thus, for our calculations of hillslope gradient, curvature, drainage area and relief, we smoothed the topography with a 2-D, 2nd order polynomial applied to a 10x10 m moving window [Wood, 1996; Hurst *et al.*, 2012].

3.2.2. Mapping resistant beds

From field observations on hillslopes and in channels, we consistently find that the resistant rock beds form cliff-like, vertical faces. Combining these field observations with airborne lidar data, we defined the resistant beds as having gradients equal to or greater than 1.0 (100%) based on smoothed slope values. This approach is similar to the method employed by [DiBiase *et al.*, 2012; Heimsath *et al.*, 2012]. Based on our field observations and field maps, this slope threshold successfully identified resistant beds throughout the Franklin Creek watershed (Figure 2-1).

3.2.3. Channel network - longitudinal profiles and slope-area plots

River profiles that deviate from a smooth, concave-up form can potentially provide insight into tectonic and lithologic controls on valley network processes [e.g. Hack, 1957; Duvall *et al.*, 2004; Wobus *et al.*, 2006; DiBiase *et al.*, 2010; Kirby and Whipple, 2012]. Channel slope is commonly quantified as a function of contributing drainage area described by a power law:

$$S = k_s A^{-\theta} \quad (2-1)$$

where S is the local channel slope, k_s , a dimensional constant, is the steepness index [$L^{2\theta}$], A is contributing drainage area [L^2] and θ is the concavity index. Given steady state conditions, k_s is a function of rock uplift [Snyder *et al.*, 2000; Wobus *et al.*, 2006] as well as channel width, rock properties, climate, and sediment supply [Howard, 1998; Whipple, 2004; Sklar and Dietrich, 2006; Ferrier *et al.*, 2013]. Although a multitude of studies use k_s values to map relative variations in channel incision [e.g. Wobus *et al.*, 2006; Kirby and Whipple, 2012 and citations within], we used the same relationships to explore the role of resistant rock on channel profiles and channel processes [Duvall *et al.*, 2004; Allen *et al.*, 2013].

We followed standard network delineation procedures [Wobus et al., 2006], choosing a threshold area of 5000 m² in order to extend the valley network above the fluvial network and into low-order, debris flow-prone portions of the valley network [Lague and Davy, 2003; Stock and Dietrich, 2006]. We calculated channel slope, drainage area and the spatial integral of the drainage area versus elevation (chi plots) [Perron and Royden, 2013] using the Stream Profiler tool [Whipple et al., 2007] with a 10 m smoothing length scale and a vertical sampling interval of 0.1 m to capture knickpoints and resistant bedforms in the channel. Because the downstream portions of the channel network are alluvial, we restricted the slope-area plot fits to the bedrock portion of the channel network. Specifically in Harvey watershed the slope-area plots extend to an area ~ 3 km upstream from the river mouth and in Franklin the plots extend to an area ~ 1 km upstream.

3.2.4. Valley width

Valley width controls hyporheic exchange [Kasahara and Wondzell, 2003], sediment storage, and river features supporting aquatic function such as overwintering habitat during large flood events [e.g. Naimen and Bilby, 1998]. To measure valley width, we followed the methods employed by May et al. [2013], which entails using a slope gradient map derived from the smoothed lidar data set to identify valley floors from steep, adjoining hillslopes. We measured cross sections perpendicular to the valley axis on a hillshade map overlain with the gradient values along straight sections of stream reaches in the mainstem and tributary channels of Franklin Creek. For Harvey Creek, we used valley width data previously described in May et al. [2013]. We did not include valley width measurements in reaches with debris flow deposits as the aggraded sediment and large woody debris deposits are transient features that complicate interpretations of valley width.

3.3. Hillslope gradient-erosion model

To estimate the extent to which resistant beds retard channel incision and regulate upstream erosion rates, we employed a theoretical model for the relationship between erosion and average hillslope gradient previously calibrated in the OCR. At low gradients, the relationship between slope and erosion rate is linear and then becomes

highly nonlinear as slopes steepen to near critical values [e.g., *Montgomery and Brandon, 2002*]. In this nonlinear regime, small increases in erosion rates lead to rapid increases in sediment flux, such that hillslope gradients are not sensitive to erosion rate variations [*Roering et al., 1999; Ouimet et al., 2009; Dibiase et al., 2010*]. Based on a one-dimensional, steady-state solution, the functional relationship between dimensionless average hillslope gradient (R^*) and erosion rate (E^*) is given by *Roering et al.* [2007]:

$$R^* = \frac{S_h}{S_c} = \frac{1}{E^*} \left(\sqrt{1 + (E^*)^2} - \ln \left(\frac{1}{2} \left(1 + \sqrt{1 + (E^*)^2} \right) \right) - 1 \right) \quad (2-2)$$

where S_h is average hillslope gradient and S_c is the critical slope gradient. The dimensionless erosion rate, E^* , is given by:

$$E^* = \frac{2E \left(\frac{\rho_r}{\rho_s} \right) L_H}{K S_c} = \frac{2C_{HT} L_H}{S_c} \quad (2-3)$$

where E is erosion rate ($L T^{-1}$), ρ_r and ρ_s are rock and soil densities ($M L^{-3}$) respectively, L_H is average hillslope length (L), C_{HT} is hilltop curvature (L^{-1}), defined here as the Laplacian of elevation (L^{-1}) [See *Roering et al., 1999; Hurst et al., 2012*] and K is the soil transport coefficient ($L^2 T^{-1}$) which incorporates factors such as the vigor of soil disturbances, soil properties, and climate. In Franklin Creek, we applied this model to soil-mantled hillslopes developed on the typical Tyee units that are perched above resistant bedrock cliffs and knickpoints. In doing so, we assumed that baselevel imposed by erosion of the resistant beds is reflected in the upstream hillslopes.

To determine the average hillslope length (L_H) in subcatchments of both Harvey and Franklin, we directly measured the horizontal distance from ridgetop to the valley centerline along the path of steepest descent following the methodology of *Hurst et al.* [2012]. In Franklin, we measured L_H in 7 first-order basins; $L_H = 104.24 \pm 11.69$ m (mean \pm std dev). In Harvey watershed, we measured L_H in 5 first-order basins where $L_H = 73.01 \pm 8.98$ m (mean \pm std dev). For the remaining variables in equations 2 and 3, we used previously published values specific to the OCR [*Roering et al., 1999, 2007*].

3.4 Hilltop curvature erosion model

On soil-mantled hilltops, erosion rate increases linearly with hilltop curvature according to:

$$E = \frac{\rho_s}{\rho_r} KC_{HT} \quad (2-4)$$

We extracted curvature and gradient data from representative ridgetops throughout the Franklin and Harvey watersheds. In addition to the Harvey ridges in catchments H1 and H2, we sampled from the central and eastern portion of the watershed. In Franklin watershed, we extracted ridgetop data from study catchments F1-F4 and from a ridge in the southern portion of the watershed (Figure 2-1). Hilltops integrate erosion rates imposed from adjoining valleys via the shared ridgetop. Thus, when selecting hilltops in Franklin watershed, we were careful to select hilltops for which resistant bedrock cliffs modulate both adjacent valleys. In both Harvey and Franklin, we selected hilltops with gradients <0.4, restricting our analysis to regions where curvature is proportional to erosion rates [Roering *et al.*, 1999], and extracted curvature values along 5 ridges with an average length of ~80 m.

3.5. Spectral analysis - biotic signatures

We applied spectral analysis to quantify the extent to which resistant beds influence the biotic signature of tree rooting activity on the landscape. We hypothesize that the massive, soil-free sandstone beds limit soil production due to their unfractured character. With a measured fracture spacing ranging from 10 to 25 m (12.9 ± 6.3 m, mean \pm std dev) in the resistant rock compared to closely spaced fractures ranging from 0.5 – 1 m (0.6 ± 0.2 m, mean \pm std dev) in the typical Tye (Supplemental Figures 2-S1, 2-S2), we hypothesize that the lack of soil on the resistant beds may reflect resistance to tree root disturbance and turnover. To test whether resistant beds exhibit the characteristic topographic signature of tree turnover via pit and mound features, we used a 1D spectral analysis of the raw gridded data over both soil-mantled typical Tye areas and non-soil mantled, resistant slope patches. We extracted topographic profiles of elevation along horizontal hillslope transects from unsmoothed gridded lidar data in areas where the raw lidar point cloud data exhibits a high density of bare earth returns for both soil-mantled (n=3) and resistant rock (n=3) swaths. We then interpolated the profile data to a 1 m spacing and applied a 1D discrete Fourier transform (1D DFT). Fourier spectral analyses transform discrete information from the spatial domain into the frequency domain, which

quantifies how the amplitude of topographic features (such as tree disturbances or mima mounds) are distributed across a range of spatial frequencies or wavelengths [Rayner, 1972; Hanley, 1977; Harrison and Lo, 1996; Perron *et al.*, 2008]. The DFT of a one-dimensional data set, $z(x)$, consisting of N_x measurements at equal intervals of Δx can be written as:

$$Z(k_x) = \sum_{m=0}^{N_x-1} z(m\Delta x) e^{-2\pi i \left(\frac{k_x m}{N_x}\right)} \quad (2-5)$$

where k_x is wavenumber and m is the index in z [Priestly 1981].

To estimate the power spectrum of z , we used a DFT periodogram, which provides a measure of how the variance of z varies with the frequency. One common way of estimating the power spectrum is:

$$V_{DFT} = \frac{1}{N_x^2} |Z(k_x)|^2 \quad (2-6)$$

where V_{DFT} equals the variance with the units of amplitude squared. Parseval's theorem states that because the Fourier transform is unitary, the sum of the power spectrum is equal to the variance of z . In order to compare spectra variance between the resistant and typical rock we normalized the profiles to have a total variance of 1 (m^2).

3.6. Topographic relief

The length scale for calculating topographic relief is often determined *a priori* by using an ad hoc radius in order to describe elevation differences within a drainage basin [e.g. Ahnert, 1970, Montgomery and Brandon, 2002]. At the hillslope scale (100 m radius), relief is strongly correlated with mean basin gradients, while at larger window sizes, the steepness of tributaries (1-5 km), major rivers (>10 km) and range height is incorporated into the relief metrics [Whipple *et al.*, 1999; DiBiase *et al.*, 2010]. We performed an analysis of dominant length scales in Franklin and Harvey watersheds to determine whether pervasive resistant beds in Franklin could alter the competition between diffusive and advective processes, and therefore valley ridge spacing [Perron *et al.*, 2009]. We measured ridge-valley spacing at both the hillslope scale and the larger catchment scale (e.g. catchments F1-4 and H1-2, Figure 2-1) in ArcMap, recording 50 ridge-to-ridge lengths at both the unchanneled and major ridge-valley scales in Franklin

and Harvey for a total of 200 measurements. Given the generally ovoid catchment shapes, we chose the mean width when measuring ridge-to-ridge lengths.

4. RESULTS

4.1. Petrology and tensile strength

From thin section analysis, we found no significant difference in grain size, porosity, or mineral composition between the typical (n=5) and resistant (n=9) Tyee rock samples. All samples contain angular micaceous arksoic grains and immature volcanic clastics within patches of pseudomatrix. We observed no calcite or calcite cement in the typical or resistant rock, although chlorite and chlorite cement appears sporadically in resistant rock samples. A distinct difference between the resistant and typical samples is very minor (< 1%) amounts of diagenetic rimming clay in the resistant rock. The rimming clay is fibrous and forms an inter-grain framework (Figure 2-3).

Qualitative elemental analysis using the SEM energy-dispersive X-ray spectrometry function suggests that the rimming clays are from a class of mixed layer clays that includes: corrensite, heulandite/clinoptilolite and laumontite, any one of a group of fibrous clays that have been shown to cement and strengthen rock [Ryu and Niem, 1999; Al-Tahini et al., 2006]. These mixed layer clays are found in turbidite detrital deposits [Callen, 1984] and are closely related to clays used as industrial binders [Galan, 1996].

Tensile strength tests using a point load device and a Universal Testing Machine (Brazilian splitting test) reveal significant differences in rock strength. We ran two sets of tests, the first using a point load device on 25-28 mm diameter, 11-14 mm length cores of typical Tyee (n=7) and resistant Tyee (n=17) and the second using the Universal Testing Machine on 50-51 mm diameter, 25-39 mm length cores on typical Tyee (n=9) and resistant Tyee (n =6). Average tensile strengths using the point load device are 2.94 ± 0.12 MPa for the typical Tyee and 4.10 ± 0.28 MPa for the resistant samples. Using the Universal Testing Machine, we also observe a significant difference in tensile strengths, with the tensile strength for typical samples equal to 0.83 ± 0.04 MPa compared to 2.06 ± 0.27 MPa for resistant samples (Figure 2-3). (All values are mean \pm std err). The patchy

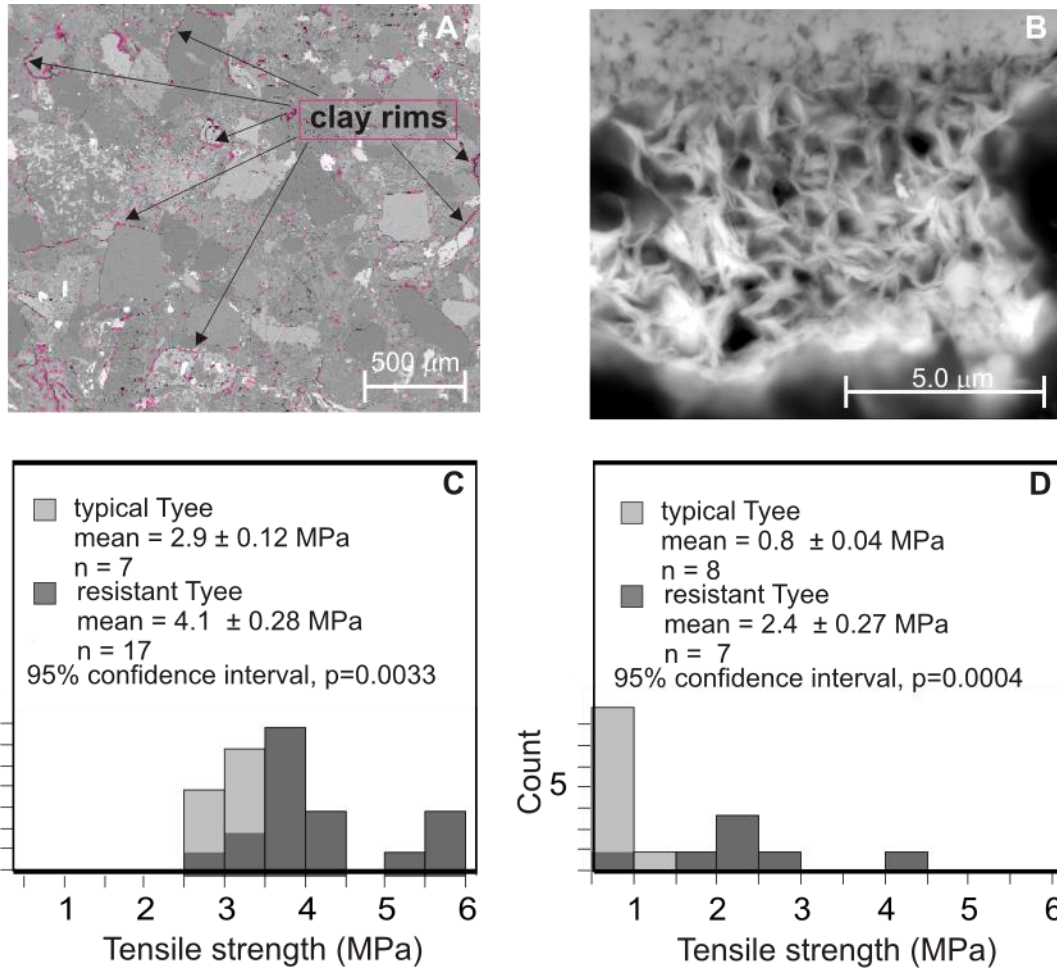


Figure 2-3. Petrology and tensile strength results. .A) Backscatter scanning electron (BSE) microscope image of resistant rock. Black arrows points to diagenetic clay rims. B) Close-up of fibrous rimming clay. Crystalline feature at the top and bottom of the BSE image are mineral grains cemented by the fibrous clays. C and D) Stacked histograms of rock tensile strengths for typical and resistant rock calculated from load measurements using a using a point load device (3C) and the Brazilian splitting test (3D). Reported values are mean \pm standard error.

nature of the diagenetic artifacts within the resistant rock samples likely results in the observed variability in tensile strength. The differences between the tensile strength mean values for the two sample populations are significant at the 99.6% and 99.9% level for the point loading and Brazilian splitting tests, respectively. Because the Brazilian splitting test is more common for geomorphic investigations such as bedrock valley erodibility [e.g. *Sklar and Dietrich, 2001; Stock et al., 2005*], and more importantly, produces valid results over the greatest range of rock strengths [*Vutukuri et al., 1974*;

Sklar and Dietrich, 2001], we favor the mean values of 0.83 MPa for the typical and 2.06 MPa for the resistant Tyee samples.

4.2. Rock controls on catchment morphology

4.2.1. Hillslope gradients

Visual inspection of airborne lidar for the two watersheds reveals remarkably consistent topography in Harvey watershed – with evenly spaced ridges and valleys and sharp and convex ridgetops giving way to planar hillslopes. By contrast, Franklin Creek is characterized by much less consistent ridge-valley spacing and importantly, perched, gentle soil-mantled valleys above resistant, steep bedrock outcrops (Figure 2-1). We calculated the fraction of resistant beds in each watershed and found that 12% of Franklin topography compared to <4% of Harvey is comprised of resistant beds. Furthermore, the resistant beds in Harvey crop out in a patchy and dispersed fashion along the eastern margin of the catchment, which contrasts with abundant, spatially extensive resistant beds in Franklin. To determine if catchment-average morphologic metrics such as average hillslope angles reflect the influence of resistant rock beds, we calculated the distribution of hillslope gradient in both Harvey and Franklin watershed (Figure 2-4). (All reported mean gradient values include the mean \pm std dev). Hillslope gradient distributions do not reveal a statistical differences between the two watersheds as the mean hillslope gradient in Franklin watershed is 0.80 ± 0.22 , while the mean hillslope gradient in Harvey watershed is 0.75 ± 0.20 (Figure 2-4). The similarity in hillslope gradient distributions exists despite a nearly three-fold difference in the proportion of resistant beds in Franklin compared to Harvey watershed.

We performed a similar hillslope gradient analysis focusing on small tributaries within both of our study catchments. Specifically, we targeted small catchments perched above resistant beds in Franklin Creek (Figure 2-1) and identified catchments of similar size in Harvey Creek for comparison. In contrast to the indistinguishable catchment-averaged slope distributions, small tributary hillslope gradients vary significantly depending on the presence or absence of the resistant rock. Two of the Harvey sub-watersheds with uniform ridge-valley spacing (H1 and H2) gradients are statistically indistinguishable from each other and from the mean Harvey watershed hillslope gradient

(Figure 2-4). The mean hillslope gradient for H1 is 0.81 ± 0.18 , and for H2 is 0.75 ± 0.19 . By contrast, the gradient distributions for the Franklin tributaries show consistently lower values of average gradient, with means of 0.62 ± 0.14 (F1), 0.59 ± 0.13 (F2), 0.58 ± 0.13 (F3) and 0.62 ± 0.13 (F4). Taken together, these results suggest that the resistant beds increase the variance of hillslope gradient.

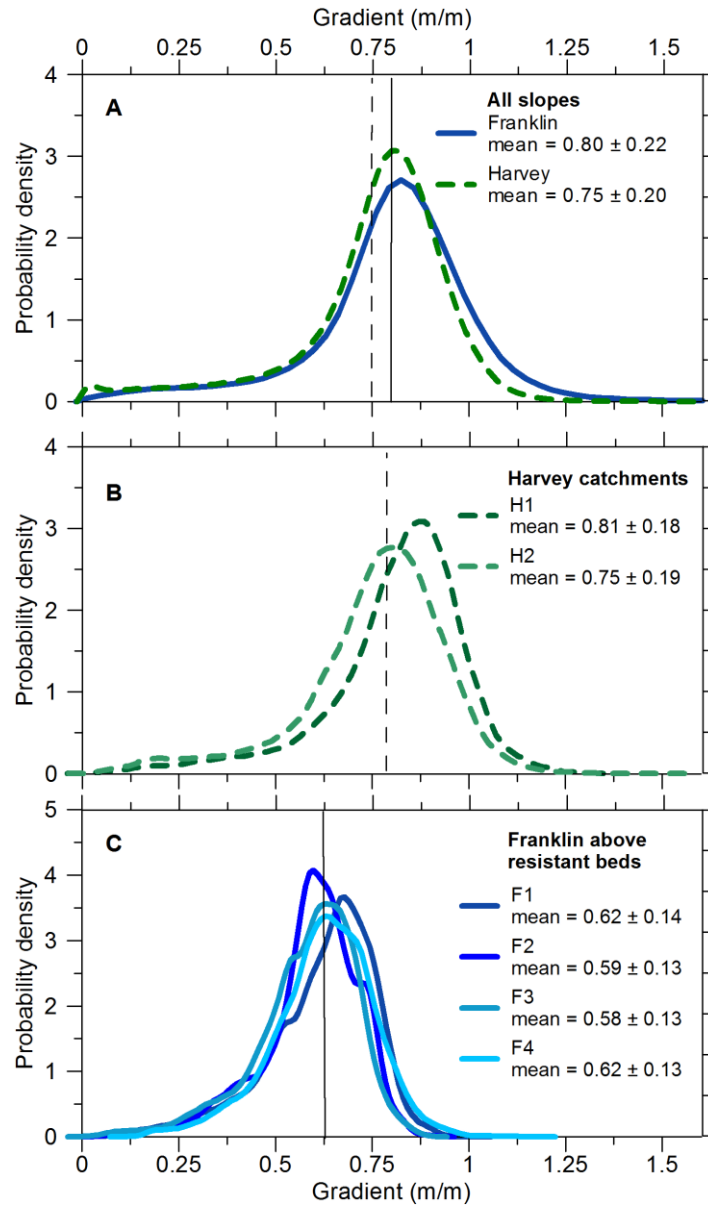


Figure 2-4. Hillslope gradient probability density functions with means and standard deviations for A) Franklin and Harvey watersheds, B) Harvey catchments H1 and H2, and C) Franklin sub-catchments F1-F4, above resistant rock beds. Solid lines and dashed lines refer to Franklin and Harvey PDFs respectively.

4.2.2. Influence of resistant beds on channel and valley network form

To explore the influence of the resistant beds on valley slope, we plotted longitudinal channel profiles for Franklin and Harvey watersheds as well as longitudinal profiles for individual sub-watersheds within the two larger basins (inset map, Figure 2-5a). The longitudinal profiles in Harvey exhibit smoothly varying, concave upward forms and show remarkable consistency. In contrast, Franklin watershed profiles shows a significant knickpoint approximately 2000 m upstream from the river mouth with a plethora of smaller knickpoints apparent further upstream (Figure 2-5a). In addition, we employed chi (χ) plots to examine the apparent elevation difference between the watershed longitudinal profiles. Chi plots linearize slope drainage area data by expressing the spatial integral of the drainage area against elevation [Whipple *et al.*, 2007; Perron and Royden, 2013]. Chi plots are only truly linear if erosion is steady and concavity and steepness are constant along the length of the analysis [Willett *et al.*, 2014]. The plots are beneficial for their ability to reduce noise common to slope-area datasets and to identify transitions in processes controlling channel form [Mudd *et al.*, 2014].

To compare the watersheds, we used the Harvey watershed longitudinal concavity value of -0.56, which reflects the fluvial bedrock portion of the networks (Figure 2-6). We first plot elevation against χ for the length of the entire valley network (Figure 2-5b), including both the debris flow and fluvial regimes. We observe an inflection in the chi plot that appears to correspond with the process transition between fluvial and debris flow regimes. This transition corresponds with the 1 km slope-area scaling break representing the transition between debris flow-and fluvial regimes (see below and Stock and Dietrich [2003]). To explore elevation differences in the fluvial portion of the channel network, we display the lower portion of the channel network at drainage areas $\geq 1 \text{ km}^2$ (Figure 2-5c). For the Franklin watershed, the χ plot exhibits a steeper slope and is offset relative to the Harvey data (Figure 2-5b and 2-5c) likely reflecting the ability of resistant bedrock beds to support the Franklin catchment at higher elevations. As the χ plot slope above the knickpoints in Franklin continues to steepen relative to Harvey, we interpret the systematic χ -elevation difference as a reflection of baselevel modulation by resistant beds limiting incision upstream.

Slope-area plots reflect process domains such as the transition between debris-flow and fluvial valleys [e.g. Montgomery and Foufoula-Georgiou, 1993; Stock et al., 2003] and incision rates as inferred from steepness indexes [e.g. Snyder et al., 2000; Kirby and Whipple, 2001,

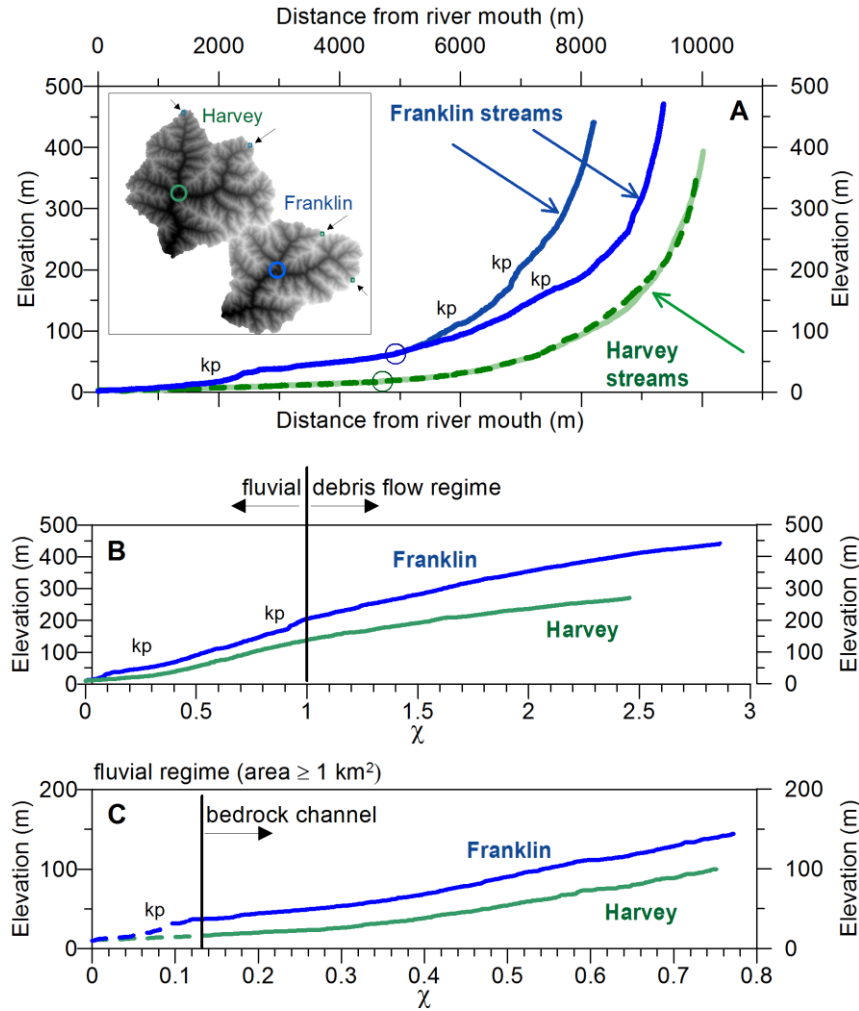


Figure 2-5. Channel longitudinal profiles and χ plots A) Longitudinal profiles extracted from Franklin and Harvey watersheds. Arrows on inset DEM identify the starting location for each of the four drainages plotted. Open circles on DEM and profiles delineate where drainages merge. We identify knickpoint locations with 'kp'. B) Elevation vs. the spatial integration of drainage area comparing data from two of the four drainages plotted in 5A. We plot data for valleys and channels with drainage area > 0.05 km². C) χ plots as in above, plotted for just the fluvial portion of the drainage network defined as drainage area > 1 km². Dashed lines identify the alluvial portions of the network. For all χ plots we use a concavity value of -0.56.

2012]. In both Franklin and Harvey watersheds, we qualitatively observe a scaling break at drainage areas $\sim 1 \text{ km}^2$ and slopes of 0.1, which likely represents the transition between debris flow and fluvial valley carving processes in the Oregon Coast Range (Figure 2-6) [Dietrich et al., 2003, Stock et al., 2003]. The slope-area plots for Franklin and Harvey are remarkably similar, especially for drainage areas $< 1 \text{ km}^2$ despite the prevalence of resistant rock beds and hanging valleys in the Franklin watershed. The ks (steepness) values for the fluvial portions of Harvey

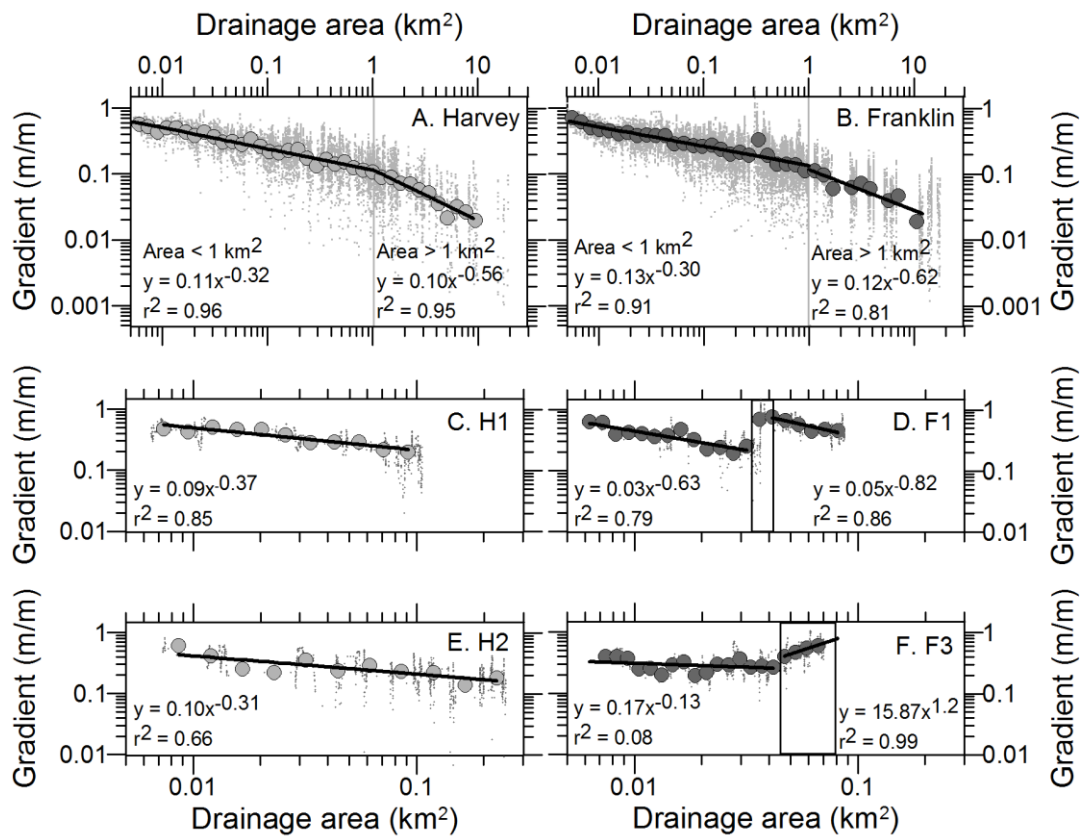


Figure 2-6. Slope-drainage area plots for A) Harvey and B) Franklin watersheds and subwatersheds H1 and H2 (C, E) and F1, F3 (D, F). Rectangles delineate location of resistant beds within Franklin catchment plots. We plot all raw slope area data with small markers. To minimize raw data noise, we log-bin the data by equal drainage area width (large circle markers) and fit regressions to the log-binned data. Bins for the alluvial sections are not included.

and Franklin are 0.11 and 0.13 respectively, while θ (concavity) values are -0.56 and -0.59, respectively. These concavity estimates are consistent with values previously measured in the central and southern OCR [Seidl and Dietrich, 1992; Kobor et al., 2004;

VanLaningham et al., 2006]. While we still lack a complete understanding of the functional relationship between slope and area in debris flow regimes [e.g. Stock et al., 2005], we can qualitatively assess differences in Harvey and Franklin debris flow slope-area plots. Similar to our hillslope gradient results, slope-area plots for individual sub-watersheds again correspond closely in Harvey watershed and exhibit variability in the Franklin watershed. Slope-area plots for Harvey watersheds H1 and H2 are nearly indistinguishable. In Franklin watershed however, slope-area plots for watersheds perched above the resistant beds exhibit significant variability and differ from those observed in Harvey. Most importantly, Franklin tributaries show an offset in slope-area data that separates terrain above the resistant beds from lower sections of catchments below resistant beds (Figures 2-6d, 2-6f). In F3, the resistant rock beds occupy a small fraction of the watershed and the downstream portion of the slope-area plot encompasses a band of resistant rock beds. In this case (F3), the θ value is positive (or convex), reflecting the strong influence of resistant bedrock on profile form.

As hillslope-channel interactions (e.g. lateral channel migration into hillslopes or channel avulsion due to landslides) influence valley morphology, we characterized the relationship between drainage area and valley width across for all basin orders in Franklin and Harvey watersheds (Figure 2-7). Following *May et al.* [2013], we focused on trends for drainage areas $> 0.1 \text{ km}^2$. We observe a power-law relation between drainage area and valley width for both watersheds (Figure 2-7) and this relationship is robust when restricting the analysis to the fluvial domain (areas $> 1 \text{ km}^2$). In essence, valley width increases more rapidly with drainage area in Harvey than in Franklin and this difference is significant at the 99% level. In Franklin watershed, we also observe greater variability in valley width with drainage area, likely reflecting the influence of the resistant beds [*Allen et al.*, 2013].

4.2.3. Hillslope model predictions of erosion rate

For the hillslope gradient-erosion model, we used equations 2 and 3 with previously calibrated transport model parameters [*Reneau and Dietrich*, 1991; *Roering et al.*, 1999]: $K = 0.004 \text{ m}^2 \text{ yr}^{-1}$, $S_c = 1.25$ and $\rho_r/\rho_s = 2.0$) to generate erosion rate estimates for sub-

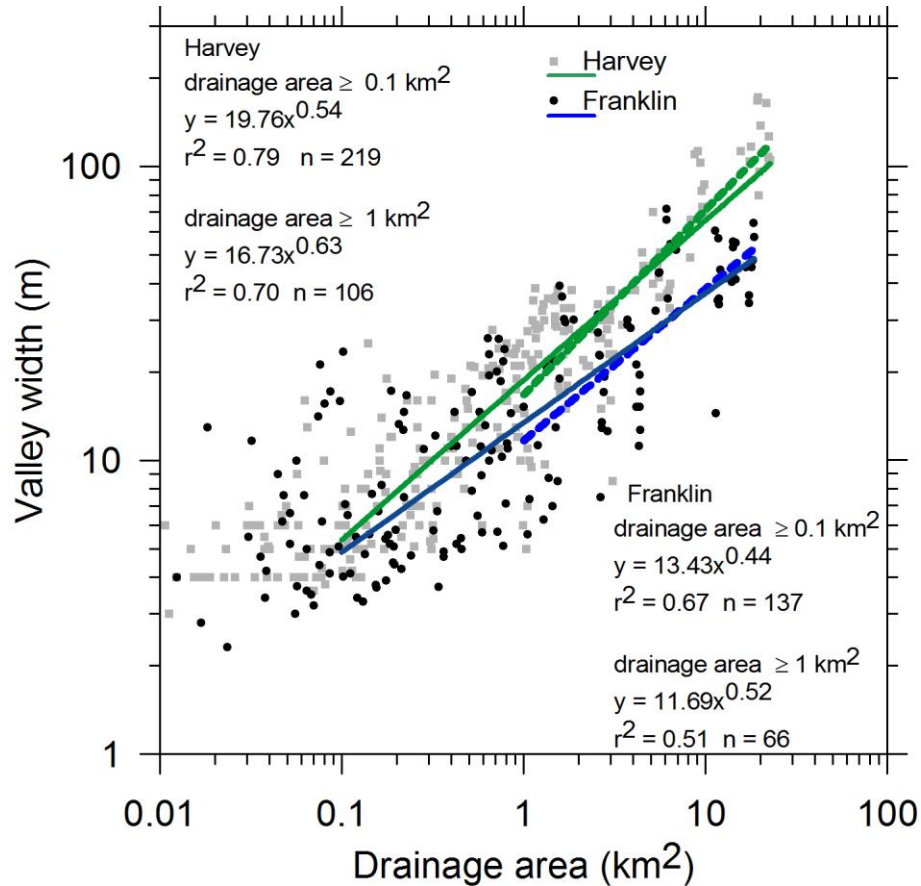


Figure 2-7. Valley width vs. drainage area values extracted from lidar data for Franklin and Harvey watersheds. We fit power laws to drainage areas $> 0.1 \text{ km}^2$ (following May et al., 2013) and to drainage areas in the $> 1 \text{ km}^2$ fluvial domain.

catchments in Harvey and Franklin. These equations apply to soil-mantled hillslopes that occur in areas that lack or are perched above the resistant beds. Analysis of smoothed lidar data indicates that hillslopes in Harvey watersheds are 1.3 times steeper than hillslopes above the resistant rock beds in Franklin (Section 4.31 and Figure 2-4). For these small watersheds in Harvey and Franklin, we used mean hillslope gradient values (S_h) of 0.75 and 0.60, respectively, calculated corresponding R^* values of 0.6 and 0.48, respectively, iteratively solved equation 2 for E^* , and then used the first half of equation 3 to calculate E . In Harvey, the predicted erosion rate is $0.087 \pm 0.19 \text{ mm yr}^{-1}$ (mean and std err). By contrast, for Franklin hillslopes above the resistant rock beds, the calculated erosion rate is $0.037 \pm 0.18 \text{ mm yr}^{-1}$, less than half the calculated erosion rate estimated in the Harvey watershed. To apply the hilltop curvature-erosion model, we estimated the

mean hilltop curvature in Harvey watershed as $-0.097 \pm 0.015 \text{ m}^{-1}$ (mean \pm std dev). The corresponding value for Franklin ridgetops is $-0.053 \pm 0.008 \text{ m}^{-1}$ (mean \pm std dev), implying a nearly two-fold difference in erosion rates (Equation 4) which is consistent with the hillslope gradient model result. From equation 4, hilltop erosion in Harvey watershed is calculated as $0.19 \pm 0.012 \text{ mm yr}^{-1}$ (mean \pm std err), while the corresponding value in Franklin is $0.10 \pm 0.016 \text{ mm yr}^{-1}$ (mean \pm std err).

We solved for E^* using the second half of equation 3 to explore how well R^* and E^* values for Franklin and Harvey compare with the nonlinear, dimensionless steady-state denudation curve (equations 2 and 3 and Figure 2-8). In essence, this calculation determines the extent to which landform properties (in this case slope, curvature, and slope length) are consistent with steady state erosion given a previously calibrated set of process parameters (e.g., K , S_c). A key caveat of this analysis is that it combines a 1D-model prediction of hillslope gradient with a 2D estimate of hilltop curvature. Nonetheless, R^* - E^* plots have been successfully used to assess erosion and hillslope adjustment in response to uplift and identify associated time lags in landscape response

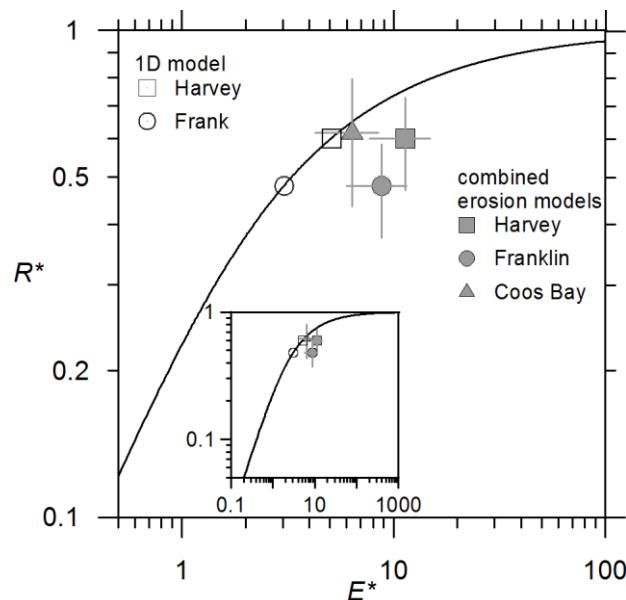


Figure 2-8. Functional relationship between dimensionless relief (R^*) and erosion rate (E^*). 1D gradient-erosion model results plotted with open symbols (Eqn. 2). Combined 1D and 2D gradient-curvature-erosion model plotted with filled symbols (Eqns. 2, 3) (See Section 4.2.3). Inset plot displays expanded domain of the R^* vs. E^* formulation. Note the Franklin 1D-2D data point falls well below the steady state curve, perhaps reflecting a transient condition.

[Hurst *et al.*, 2013a]. Calculated E^* values for Franklin and Harvey are 3.05 and 5.1, respectively, with corresponding calculated R^* values of 0.48 and 0.6 generated from $R^* = S_H/S_c$. The Franklin R^*-E^* value is significantly offset from the steady-state curve and its position indicates lower than predicted relief (or faster than predicted erosion), while the Harvey is sufficiently close the model curve such that steady erosion cannot be rejected (Figure 2-8). The offset Franklin R^*-E^* values may reflect transient adjustment of the hillslopes above the resistant beds. Consistent with this interpretation, hillslope lengths for the Franklin catchments are >25% longer than those observed in Harvey, which may result from changes in the scale of landscape dissection associated with a slower baselevel lowering rate.

4.3. The topographic signature of biotic vs. abiotic weathering

To determine whether cliff-forming, resistant beds are resilient to biotic weathering via tree root disturbances, we analyzed the roughness of topographic profiles. Most fractures in the Tyee Formation are vertical to sub-vertical, dissecting the horizontal beds. Average fracture spacing in the typical Tyee is less than 1m, in contrast to the high average fracture spacing of 12.9 m in the resistant Tyee (Supplemental Figure 2-S2). Horizontal contacts between turbidite beds in the typical Tyee is usually <1 m, facilitating detachment by tree roots or burrowing animals. The resistant rock beds lack the topographic signature of pit and mound landforms that dominate the form of soil-mantled hillslopes (Figure 2-9).

Specifically, the soil-mantled profiles generated atop typical bedrock slopes have higher spectral power at low (2 to 10 m) wavelengths compared to the resistant, bedrock profiles. In addition, the strong contrast in spectral slopes reflects the relative importance of different wavelength features in contributing to the total variance. Furthermore, the resistant rock spectra slope steepens at wavelengths of ~ 10 m, which corresponds to the fracture spacing obtained from field observations (Supplemental Figures 2-S1 and S2). In the typical Tyee profiles, high spectral power at low wavelengths likely incorporates the influence of sub-meter fracture spacing overprinted by biotic processes such as tree throw [Roering *et al.*, 2010].

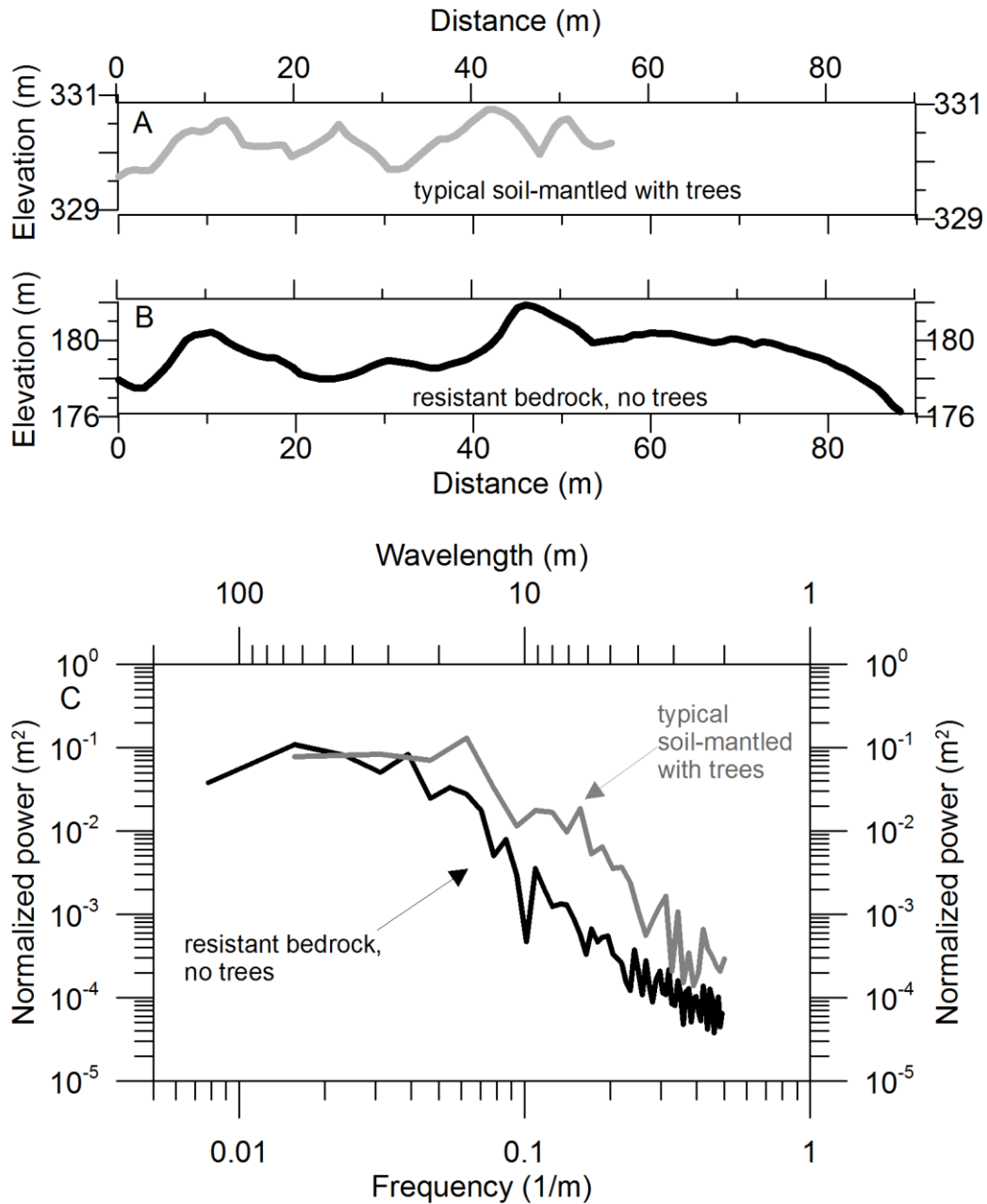


Figure 2-9. Topographic profiles and power spectra A) Topographic profiles of soil mantled and B) resistant rock extracted along horizontal profiles from the unsmoothed gridded lidar data in Harvey and Franklin watershed respectively. C) Averaged one-dimensional power spectra for soil-mantled (n=3) and resistant rock (n=3) profiles. Soil-mantled power spectra exhibit higher spectral power at wavelengths of 7m and less. Resistant rock power spectra steepens at 10 m.

4.4. Resistant beds and relief

To identify the dominant scales of dissection in our study catchments, we measured ridge-valley spacing at both the smallest hillslope scale and at the scale of

major ridge-valley sequences. In Franklin and Harvey, the hillslope spacing is essentially indistinguishable with mean lengths of 95 ± 4 m in Franklin (median = 88 m) and 97 ± 3 m in Harvey (median = 95 m) (mean \pm std err). In Harvey, we also observe a tight cluster of length scales for the major ridge-valley sequences with a mean of 351 ± 11 m and a median of 345 m. In Franklin, the major ridge valley spacing has a mean of 335 ± 21 m (median = 311 m). While the length scale is similar for both watersheds, Franklin values exhibit much greater dispersion, likely due to the prevalence of hanging valleys, cliff-dominated hillslope segments, and variable valley orientations. These results provide a length scale upon which to establish our local relief calculations.

Estimating topographic relief, here defined as the elevation range within a given area, enables us to evaluate how resistant rock beds influence landscape form at different scales in Franklin Creek. At the sub-watershed scale, resistant beds control baselevel for first and second order catchments perched above the cliff-forming units. The location of the resistant beds within the catchment will likely dictate their effect on landscape morphology. We calculated relief in both watersheds using two radii values, 100m and 350 m, as determined through our ridge-valley spacing analysis. At the 100 m scale, the mean relief in Franklin is 128 ± 22 m (mean \pm std dev), which is quite similar to the Harvey value of 116 ± 20 m (Figure 2-10a). At the 350 m scale, however, relief values are higher in the Franklin watershed compared to Harvey, and the topography exhibits a distinct decrease in relief moving SE to NW along the axis of the minor anticline that bisects Franklin Creek (Figure 2-10b). In Franklin, the 350 m radius relief values locally exceed 400 m, while Harvey values never exceed 345 m (Figure 2-10a). High relief zones in Franklin coincide with a high density of resistant rock beds, in the cliffs to the south along the Umpqua River, and along cliffs to the north (Figure 2-10b). Although resistant beds outcrop in Franklin due to an anticline [*Baldwin*, 1961], we suggest that the resistant beds control relief rather than the anticlinal structure, as we do not see elevated relief along other OCR anticlines in the typical Tyee. Additionally, we note regions with resistant rock and high relief values occurring away from the Franklin anticline (Figure 2-10b).

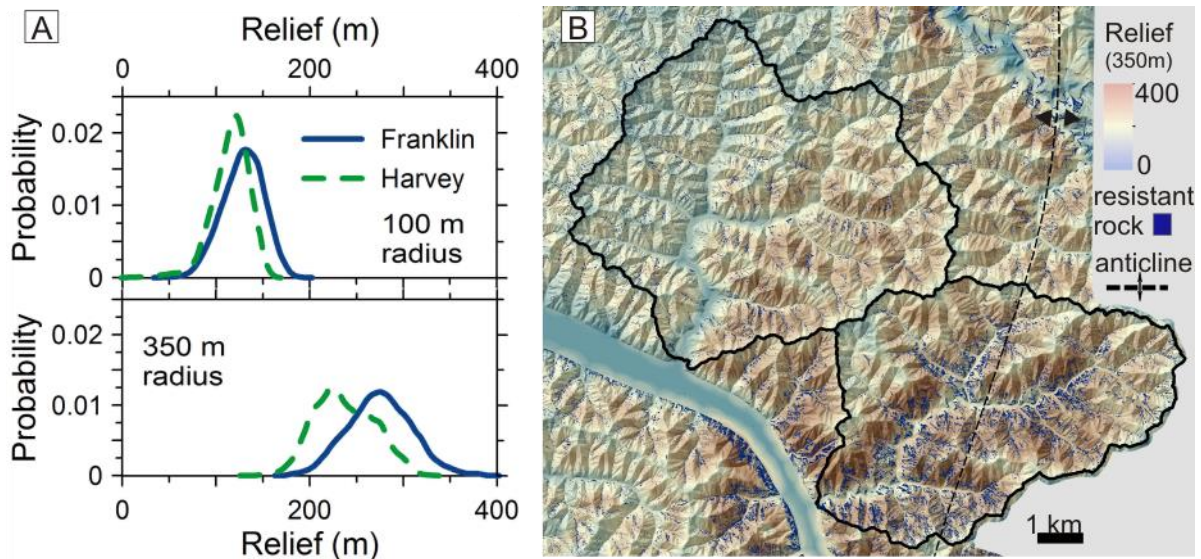


Figure 2-10. Relief comparison A) Probability density functions for mean-local relief in Franklin and Harvey watersheds at 100m (top plot) and 350m (lower plot) scales. B) Relief values calculated over a 350m radius. Areas with low relief are delineated by light blue tones, while high relief areas are shaded reddish-brown. We identify slopes with gradients ≥ 1 with dark blue coloration.

In order to quantify the potential relationship between resistant rock beds and local relief at the sub-catchment and whole-watershed scale, we calculated the percentage of resistant rock beds (gradient ≥ 1) over 100 m and 350 m radii using a neighborhood function and compared those values to the average relief within that same window. We condensed the large datasets generated from Franklin ($n > 18 \times 10^6$) and Harvey ($n > 22 \times 10^6$) into bins of equal percent-width after extracting random subsets of 64,000 data points from each larger dataset. For the 100 m analysis, the Franklin watershed has regions where the resistant beds comprise over 30% of the topography, while the Harvey watershed seldom exceeds 15% resistant beds. Not surprisingly, there is a strong correlation between mean relief and the percent of land with slope gradient ≥ 1.0 in both the Franklin and Harvey watersheds, as relief is similarly affected by local resistant bedrock at short length scales (lower plot Figure 2-11a).

By contrast, the 350 m-scale analysis reveals distinct differences in how resistant bedrock influences relief. While resistant rock beds appear in both Franklin and Harvey, there are very few continuous outcrops extending over length scales exceeding 100 m in Harvey. Only in Franklin watershed are the beds prevalent over continuous length scales

coincident with the larger ridge and valley length scale. This is well-illustrated in Figure 2-11b, which shows the fraction of resistant rock beds within a 350 m radius for both Franklin and Harvey watersheds. In Harvey, resistant beds never compose more than 12% of the topography within a 350 m radius, and rather have a mean density of ~ 5%. This contrasts with Franklin where the resistant rock beds account for 0 to 30% within a 350 m radius (Figure 2-11b). We observe a positive monotonic relationship between percent resistant beds and relief in Franklin that levels off when the local density of resistant beds exceeds 15%. At greater percentages the relationship breaks down, which is consistent with the declining density of resistant bedrock at percentages > 18% (top plot, Figure 2-11a). In Harvey, local relief at the 350 m scale does not increase with the density of resistant beds, likely reflecting the patchy, discontinuous nature of the resistant beds in that watershed.

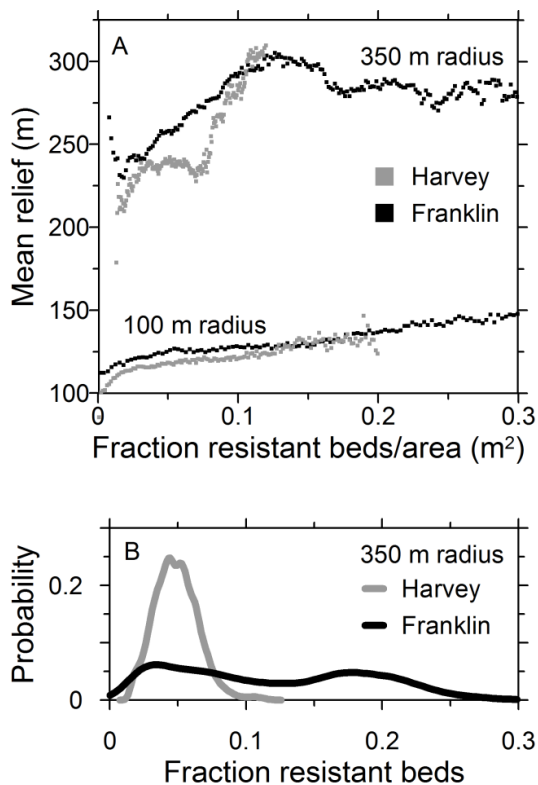


Figure 2-11. Mean relief vs. fraction of resistant beds. A) Comparison of mean relief over 100 m² area and 350 m² area vs. the fraction of resistant beds within each analytical radius. Length scales correspond to sub-catchment and larger ridge valley spacing. B) Normalized distributions (PDFs) of percent resistant beds found within 350 m² area for each grid value. For all plots we generated a random subset of 64 thousand samples for Franklin and Harvey watershed from datasets of 18 and 22 million points for Franklin and Harvey watersheds respectively. In Figure 2-11A we binned the sub-sampled data into 100 evenly spaced bins.

5. DISCUSSION

Geomorphologists frequently list the triumvirate of lithology, climate, and tectonics when describing the fundamental controls on landscape evolution. In this study, we ask the following question: What is the geomorphic significance of lithologic

variation within a seemingly uniform geologic unit? Geomorphologists commonly cite uniform rock type and proceed to ascribe topographic patterns to tectonic, climate, or geomorphic process differences. In the well-studied Oregon Coast Range, lidar allows us to confront the geomorphic implications of lithologic variability. Our analysis indicates that diagenetic variations in rock properties may influence a broad array of geomorphic processes and thus landscape form and evolution.

5.1. Sink to source - diagenesis to rock hardness

Our observations suggest that a diagenetic set of authigenic minerals and clay cements strengthen units that crop out as cliff-forming beds in Franklin Creek. These Eocene basin (sink) morphology-driven grain-scale reinforcements appear to be responsible for increasing tensile strength by 2.5 times relative to beds of the typical Tyee Formation (Figure 2-3). In turn, these present-day source materials influence modern hillslope and channel processes.

In this contribution, we do not pinpoint the exact mineralogical change associated with the diagenetic setting, given that the diagenetic processes in immature volcanic clastic sedimentary deposits allow for multiple clay minerals or cements with the potential to increase rock strength. However, our enhanced understanding of the petrology, diagenetic processes, and artifacts shaping the Tyee, improves our ability to calibrate model parameters and predict the extent of rock property influence on geomorphic function. Based on thin section and SEM analyses and an extensive review of the existing literature [e.g. *Rogers and Richardson*, 1964; *Snavely et al.*, 1964; *Lovell*, 1969a, b; *Ryu and Niem*, 1999], our observations suggest that while calcite and chlorite cements are present throughout the sand-dominated, coarse-grained slope and proximal ramp deposits of the ancestral Tyee Formation (Figure 2-2), fibrous clays and or abundant amounts of chlorite cement are distinct to the resistant beds. Our findings are corroborated by earlier observations of resistant Tyee beds in a region bounded as far south as the Coquille River and to the north by the Siuslaw river watershed [*Dott Jr.*, 1966; *Lovell*, 1969a; *Chan and Dott Jr.*, 1983].

The horizontal and vertical spacing of the resistant beds in Franklin Creek is non-systematic and it is unclear whether climate, depositional patterns, diagenetic processes,

provenance, or autogenic variability controls the bed spacing and thus the spatial and temporal influence of resistant beds on OCR landscape morphology. While speculative, we next ponder potential controls on the horizontal and vertical extent of the resistant beds. Post-initiation of the Cascadia subduction zone at 49 Ma, massive and prolific sediment inputs inundated the ancestral Tyee River along the forearc [Heller *et al.*, 1987; Dumitru *et al.*, 2012]. Unconfined sheet flow down the delta slope dominated sediment transport to the basin plane, leading to little or no differentiation of the ramp slope into features such as deep canyons, overbank deposits, or inter-channel areas [Heller and Dickinson, 1985]. Rather, the deposits formed as sheets of sediment distributed over the narrow continental shelf. The source river sediments were extremely well-mixed [Heller *et al.*, 1992] with sediment accumulation rates greater than 0.7 mm yr^{-1} [Chan and Dott Jr, 1983]. The horizontal continuous yet non-contiguous nature of the resistant rock within our study area may reflect a spatial limit to the individual packets of turbidite deposits flowing down a continental ramp (Figures 2-1, 2-2, Supplemental Figure 2-S1). Indeed, a survey of present-day bathymetric images in submarine ramp settings reveals a crenulated morphology reminiscent of the horizontal organization of the resistant beds in Franklin Creek. In addition to the non-contiguous horizontal spacing, vertical spacing of the resistant beds is also non-uniform, consistent with the variable bedding thickness in the Tyee Formation [Heller and Dickinson, 1985]. Using measured bed thicknesses ranging between 1 and 15 m in height, and an average sedimentation rate of 0.7 mm yr^{-1} [Chan and Dott Jr, 1983], we calculated that resistant bed deposition occurred over ~20 ky intervals, which eliminates mechanisms including landslide deposits from deep subduction zone earthquakes, eustatic changes in sea level, or climate variability during the Eocene. Instead, the resistant rock beds may result from a combination of necessary and sufficient mineral assemblages derived from mafic contributions from the proto-Cascade arc at shallow burial depths [Galloway, 1974; Ryu and Niem, 1999] and subject to kinetic nucleation zones where sandstone chemical diagenesis occurs [Hayes, 1979].

5.2. Rock hardness, fracture density and limits on soil production

In soil pits and on road cuts we observed fracture densities ranging on the order of <1m in the typical Tyee formation. By contrast, average fracture spacing is more than an

order of magnitude higher in the resistant Tyee (Supplemental Figures 2-S1 and 2-S2.) We propose that the presence or absence of diagenetic strengthening materials within the Tyee Formation controls fracture density given that nearby highly fractured typical Tyee beds likely experienced a similar stress history. The sparsely fractured, resistant rock beds are commonly devoid of soil and lack the topographic signature of trees found in the soil-mantled landscape underlain by the typical Tyee (Figure 2-9). *Heimsath et al.*, [2001] posited that the distribution of unweathered bedrock in the OCR limited soil production and transport processes by preventing tree roots and burrowers from penetrating resistant rock. This connection between rock properties and biotic weathering mechanisms implies that fracture density may control soil production mechanisms in resistant beds of the Tyee Formation.

Tree roots penetrate cracks in cliff faces and grow in rock with very little to no soil, although the roots are generally associated with rock fissures [*Matthes-Sears and Larson*, 1995]. Bedrock to soil production mechanisms via tree roots range from the cantilever beam-like leverage exerted by large diameter trees during windstorms [*Lutz*, 1960] to simple displacement via lift forces generated by roots extending along horizontal bedding planes. *Lutz* [1960] measured tree-induced movement of rocks weighing up to 4.5×10^3 kg when compiling data on the maximum movement of rocks by tree roots. Assuming a bedrock density of 2.3 g cm^{-3} [*Reneau and Dietrich*, 1991] for the Tyee Formation, a vertical fracture density of 3 m, and a horizontal bed spacing of 1 m, the calculated mass for a 9 m^3 block of rock is 21×10^3 kg, which is more than $4 \times$ *Lutz's* [1960] maximum measured value of 4.5×10^3 kg. Specifically, a tree root extending along a horizontal bedding plane below the rock block exerts a force equal to:

$$F = m_r * a_g \quad (7)$$

where m_r is the rock mass and a_g is the acceleration due to gravity. To lift a 9 m^3 block of the resistant Tyee, a root would need to exert a force of $\sim 2.0 \times 10^5$ N. Tree roots along a horizontal plane have been observed to exert a radial pressure on the surrounding rock and these radial pressures have been measured up to 0.91 MPa [*Bennie*, 1996]. Thus, in order to lift a 9 m^3 block of Tyee sandstone, root area would need to exceed 2 m^2 (equivalent to a diameter of over 0.5 m), which exceeds the maximum diameter of the

largest roots found in the OCR. In comparison, we executed the same analysis for the typical Tyee, with an average fracture spacing of 0.59 m (Supplemental Figure 2-S2). By only varying the fracture spacing in the calculations we arrive at a calculated volume of $0.35 \times 10^3 \text{ m}^3$ and a mass of $0.8 \times 10^3 \text{ kg}$ (dimensions of $0.59 \text{ m}^2 \times 1 \text{ m}$). Thus, to lift an average typical Tyee block, a root would need to exert a force of 0.08 MPa, an order of magnitude lower than maximum measured tree root radial pressures that have been previously measured [Bennie, 1996]. We calculated that a minimum root diameter of 0.1 m is required to lift an average size block of the typical Tyee; we commonly observe roots of this size in exposed Douglas fir root masses. These simple calculations suggest that rock strength controls on fracture density also affect bedrock detachment by tree roots, thus representing a limit on tree roots as a soil production and erosion agent.

5.3. Resistant rock beds, topographic metrics, and landscape evolution

Given the prevalence of cosmogenic radionuclides for measuring erosion rates, numerous studies assess the extent to which erosion varies with various topographic metrics, perhaps most commonly average gradient. Interestingly, whole-watershed hillslope gradient and slope-area data do not show a significant difference between Franklin and Harvey watersheds despite the difference in relief between the two watersheds at the larger ridge and valley scale. Rather the influence of resistant rock beds on local base level and the mechanics and rates of soil production becomes readily apparent when comparing slopes and slope-drainage area plots at the subcatchment scale (Figures 2-4 and 2-6). Curiously, in the case of Franklin watershed, it appears that the combination of high gradient non-soil mantled slopes and lower gradient soil-mantled slopes perched above the resistant rock beds, roughly balance the mean hillslope gradient in the adjoining soil-mantled Harvey watershed.

Conversely, longitudinal and chi profiles that traverse the length of the two watersheds show significant differences (Figure 2-5). Similarly, while valley width systematically increases as a power law function with drainage area in both watersheds, valleys are nearly 1.5 times wider in Harvey than in Franklin (Figure 2-7). Our results imply that whole-watershed gradient comparisons may be a potentially perilous analytical tool for making process-scale predictions.

In Franklin, the similarity in the slope-drainage area plots between the two watersheds may simply result from the offsetting effect of slope differences in Franklin. Of note is the pronounced scaling break between drainage areas $<1 \text{ km}^2$ and larger drainage areas (Figures 2-5 and 2-6), which suggests that a fundamental process signature, the debris-fluvial transition, is not suppressed by the resistant beds. *Duvall et al.* [2004] noted correlation in concavity indexes with variability in bedrock competence, with high concavities associated with the more resistant rocks. Not surprisingly, we see no similar relationship in Franklin, as unlike the *Duvall et al.* [2004] study, our watersheds do not cross a resistant rock lithology before transitioning to a weaker rock type further downstream, but rather, intermittently encounter resistant rock beds.

Topographic metrics describing hillslope gradients and slope-drainage area relationships in Franklin provide insight into the evolution of channel profiles as resistant rock beds are exposed. Comparing slope-area plots within Franklin watershed, we observe a dramatic difference between sub catchments (Figures 2-6d and 2-6f). In F1, the exhumation of resistant rock beds has been ongoing for some time, such that only the upper half of the catchment remains perched above the beds. This contrasts with F3, in the northern part of the watershed, where the resistant rock beds are just beginning to emerge. We interpret the concave-up channel profile in catchment F1 as indicative of long-standing hard rock exposure in the southern part of Franklin watershed, while the catchment F3 (and nearby) hillslopes are responding to the newly exhumed beds, such that the resistant rock channel has yet to erode into a concave-up form.

Both the hillslope gradient and the hilltop curvature models predict that Franklin catchments perched above the resistant beds erode at approximately half the rate of Harvey catchments. The difference in erosion rate predictions for the gradient (Equations 2 and 3) and hilltop (Equation 4) models likely reflects model assumptions (e.g., 1D vs. 2D solutions) and lidar processing choices, such as smoothing length scales. Thus, we assert that the models agree as to the magnitude of the erosion rate contrast.

By incorporating the hilltop curvature-erosion model results (Equation 4) within the dimensionless E^* and R^* framework (Equations 2 and 3), we can explore deviations from steady state. Given baselevel changes, hilltop curvature responds by sharpening in response to an increase in uplift and relaxing in response to a decrease in uplift rates

[Hurst *et al.*, 2013a]. Our model results (Figure 2-8) suggest that Franklin watershed may be more transient than Harvey. As changes in absolute uplift rates propagate from channel to hillslope, slope gradients respond faster than drainage density and thus hillslope length [Howard, 1997]. Given the somewhat patchy presence of the resistant beds in Franklin, transience and basin reorganization seems likely. Visually the topography of Franklin appears disorganized with respect to catchment orientations, basin shape and drainage density (Figure 2-1), particularly when compared with the regularity of Harvey. Our results suggest that as the resistant beds emerged in the Franklin watershed, hillslope erosion slowed, hilltop curvatures relaxed, and hillslopes lengthened, with an expected trajectory that reverses the hysteresis imposed by a passing wave of increased uplift [Hurst *et al.*, 2013a].

We posit that elevated relief values in Franklin watershed result from the combination of resistant beds within individual small catchments, a large knickzone in mainstem Franklin, and the watershed-scale influence of changes in sediment supply and caliber propagating through the basin. In bedrock channels the rate of incision is proposed to depend on the grain size supplied to channels [Sklar and Dietrich, 1998; Sklar and Dietrich, 2004]. In the individual catchments, the resistant beds set local base level and thus influence erosion rates and relief. Hillslope grain size distributions in paired catchments with contrasting erosion rates consistently exhibit a positive correlation between decreased erosion rates, grain size, and durability in multiple lithologic and climatic settings [Marshall *et al.*, 2009]. We speculate that in Franklin watershed, the resistant rock influences grains size distribution supply to the channel, and thus, incision rates in two ways: via modulation of the typical Tyee grain size distribution and by dint of the resistant Tyee weathering patterns. First, we expect sediment in slow eroding soil-mantled catchments perched above resistant beds to have a smaller overall grain size distribution, smaller median grain size, and abrade faster than the a sandstone with the same rock properties in a faster eroding watershed due to the longer weathering time in the soil [Marshall *et al.*, 2009; Sweeney *et al.*, 2012]. Secondly, we have observed two modes of resistant rock erosion: massive block failure or exfoliation of easily broken cm-scale rock flakes. The massive resistant rock blocks create immobile boulder fields in Franklin Creek and its tributaries, as they are too large for fluvial transport. In fact, we

observe potholes on these massive blocks in Franklin Creek, suggestive of their long-lived nature. Overall, the combination of reduced grain size supply and caliber from perched watersheds and over-sized supply from the resistant rock should result in a smaller range of incision effective grain sizes (tools) in Franklin watershed compared to the ‘typical’ tool supply in Harvey.

In the Oregon Coast Range, the context of the Eocene submarine ramp depositional setting constrains modern-day geomorphic processes. Sand-silt ratios and structure control deep-seated landslides in the region, with large >1km-scale landslides correlating with increased silt to sand ratios and bedrock down-dip locations [Roering *et al.*, 2005]. In contrast to the silt-dominated region, where the hills are effectively weaker and slide-prone, our sites within the sand-dominated proximal slope setting reveal diagenetic variations that can prop the landscape up and increase relief. Furthermore, our results imply several means by which we may incorporate rock properties into geomorphic process models. In landscapes where trees dominate sediment production, fracture density may limit soil production and control the extent of rock fall-dominated bedrock to mobile regolith production. Thus, we might expect that the peak soil production value (often defined as the soil production rate when soil depth is absent) in soil production models increases with fracture density. Furthermore, bedrock strength can directly enter tools-based models of fluvial and debris flow incision [e.g. Sklar and Dietrich, 2004; Stock and Dietrich, 2006].

Our results highlight the need to consider and even embrace petrologic (and in this case diagenetic) sources of bedrock variability. With the increasing availability of airborne lidar and open source tools for extracting topographic metrics such as channel steepness indexes it is possible to attribute morphologic variability to climate or tectonics when instead grain-scale differences may control soil production (Section 4.3 and 5.2) or hillslope and channel erosion processes (Sections 4.2-4.4 and 5.3). As such, lithologic variability is a key consideration when interpreting landscape form and calibrating process models.

6. CONCLUSIONS

We have exploited the contrasts between resistant and non-resistant rock exposures in two adjoining watersheds in the well-studied Oregon Coast Range to examine how rock properties influence the mechanical properties of rock and thus geomorphic function and landscape processes. In contrast to most studies that referenced *Gilbert's* [1877] early observations demonstrating that hard rock creates steeper landscapes, lidar data allows us to quantify the scale over which hard rock modulates to local- and watershed-scale geomorphic form and function. In single lithologies, we commonly make an assumption of uniformity, and ignore intra-lithologic variation. In this study, we show that rock property variation over small spatial extents within a single lithology may have profound implications for landscape evolution.

We have demonstrated that trace differences in diagenetic processes, specifically a combination of fibrous clays and chlorite cements, manifest as 1 to 10 m thick bands of resistant bedrock that are continuous yet non-contiguous in our study area. We utilized 1D spectral analysis to document the lack of a biotic signature imparted by trees roots in the non-soil mantled resistant rock, which contrasts with the biotic signature pervasive in the typical bedrock. Based on simple mass calculations we established that rock control on fracture density may limit bedrock to soil production via detachment. We used theoretical erosion-topography models to predict erosion rates for catchments perched above the resistant beds and found that these values are approximately half those observed for nearby hillslopes unaffected by resistant beds. We demonstrated that thin bands of resistant rock control relief at the watershed scale for >1My periods.

Our findings suggest that even meter-scale expressions of lithologic variability may control geomorphic function enough to challenge the appropriateness of parameterizing process models under the assumption of uniform behavior within a single lithology.

7. BRIDGE

Having determined that diagenetic variability influences geomorphic form and function, in the following chapter, I focus on the role of climate in modulating variations in erosion rates over the extent of the Oregon Coast Range 21 ka. Understanding climatic

influences on rates and mechanisms of landscape erosion is an outstanding problem in Earth science, important for quantifying soil formation rates, sediment and solute fluxes to oceans, and atmospheric CO₂ regulation by silicate weathering. Glaciated landscapes record erosional efficiency through moraine deposits and U-shaped valleys, but more widespread unglaciated hillslopes and rivers lack obvious climate signatures, hampering mechanistic theory for how climate modulates fluxes and form. The results described in Chapter III provide a new framework to quantify how the late Pleistocene affects modern erosion and soil formation rates in unglaciated environments.

CHAPTER III

FROST, NOT PRECIPITATION, DROVE INCREASED EROSION

IN UNGLACIATED TERRAIN 21,000 YEARS AGO

I carried out the work described in this chapter under the guidance of Dr. Josh Roering, Dr. Dan Gavin, and Dr. Darryl Granger. Dr. Patrick Bartlein and Dr. Sarah Praskievicz developed the paleoclimate simulations used in this project. Dr. Alan Rempel and Dr. T.C. Hales provided valuable input on the frost cracking model. All authors commented on early drafts of the manuscript. I did all the writing

1. SEEKING THE ELUSIVE SIGNATURE OF GLACIAL INTERVALS IN UNGLACIATED TERRAIN

In unglaciated landscapes, one can observe vast grass- or forest-covered hillsides that plunge to V-shaped valleys carved by fluvial and debris flow processes. While glaciated landscapes record increased erosional efficiency through ubiquitous moraine deposits and U-shaped valleys, these more widespread unglaciated hillslopes and rivers lack obvious climate signatures, impeding development of mechanistic theory for how climate modulates fluxes and landscape form and limiting our ability to predict landscape dynamics due to climate change (1–4). Landscape response timescales generally correspond with orbital cycle (Milankovitch) timescales, confounding our ability to test the hypothesis that unglaciated settings deviate from steady erosion due to fluctuating climate regimes (5). Precipitation change is commonly invoked when considering the effect of glacial intervals on unglaciated settings, with increases in river discharge or decreases in vegetation proposed to control river incision or terrace formation (6–8). While numerous terrace-forming mechanisms have been proposed, these landforms provide an incomplete and potentially biased record of geomorphic response to climate (8, 9). Surprisingly, despite quantification of appreciable modern frost-driven sediment production and transport in cold, unglaciated terrain (10, 11), there has been little consideration that temperature rather than precipitation, may dictate the frequency, magnitude, or style of erosion in unglaciated landscapes during glacial intervals (3).

Near-continuous organic and inorganic deposits archived in sedimentary basins record climatic controls on geomorphic processes and rates, and enable us to decipher how past climates influence erosion rates, particularly with the advent of isotopic tools such as cosmogenic nuclides (12). In tectonically active settings, such as the unglaciated Oregon Coast Range (OCR) of the Pacific Northwest, USA, paleoarchives are rarely preserved. One notable exception is Little Lake, Oregon, a small landslide-dammed remnant of a much larger paleolake (~8 km² catchment), extensively studied by paleoecologists (13, 14) (Appendix B). Little Lake is located in the temperate portion of the OCR at latitude 44.2°N; over 400 km to the south of the maximum extent of the Cordilleran ice sheet (~ 47.2°N, Fig. 3-1). Fossil plant communities in the 50 kyr archive chronicle open canopy forests during Marine Isotope Stage (MIS) 3 (50-26 ka), a cold, dry, and nutrient-poor parkland setting during the glacial (MIS 2, 27-13 ka), and a shift towards warm, moist conditions and temperate, closed-canopy Douglas-fir forests from 13 ka with the onset of the modern inter-glacial interval (MIS 1) (13, 14). Here we report sedimentary, geochronology, and paleoecology analyses from a new Little Lake sediment core (Methods and Appendix B Text). When combined with a frost weathering model, these observations demonstrate that temperature-driven erosional processes were pervasive and vigorous during the LGM in mid-latitude settings.

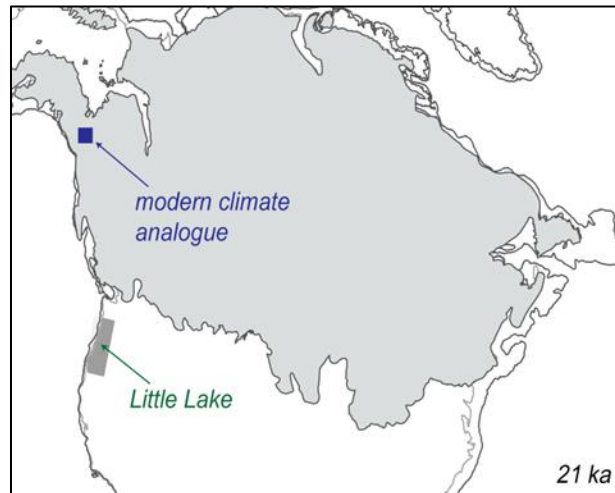


Figure 3-1. Map showing extent of the ice sheets 21 ka, location study area (dark grey polygon) and Little Lake, OR. Modern analogue ecosystem location identified with a blue square. Continental extent 21 ka outlined in black and modern continental extent outlined in grey.

2. LITTLE LAKE SEDIMENT CORE RESULTS

The Little Lake catchment and sedimentary system has all of the prerequisites necessary and favorable for utilizing detrital ^{10}Be to calculate paleo-denudation rates (12) (Methods and Appendix B). Thus, to quantify how climate may have altered erosion rates during the LGM relative to present-day, we measured detrital ^{10}Be concentrations from river-derived fine sand archived in paleolake sediments and modern-day river deposits collected upstream of the paleolake (See Appendix B, Fig. 3-S1). LGM erosion rates remained constant at 0.2 ± 0.01 mm yr⁻¹ (mean \pm se), which is 2.5x faster than present-day catchment erosion rates that average 0.08 ± 0.01 mm yr⁻¹ (See Appendix B, Fig. 3-S2, Table 3-S2). Further, this erosion rate contrast is likely a minimum value because of isotopic inheritance that occurs during changes in erosion rates (12, 15) (Methods and Appendix B). In the sediment core, we also observe a transition from finely laminated lacustrine clay, silt, and sands to coarse lacustrine blue-grey sand deposits at ~ 26 ka, coincident with the LGM transition from open canopy forests to a cold and dry parkland setting (13, 14). These distinct angular sand deposits persist throughout the glacial interval and transition to layered, poorly sorted deposits during the forested Holocene. From analysis of our sediment core, we refine previous Little Lake pollen-based vegetation reconstructions with macrofossil assemblages that indicate co-occurrence of *Picea Sitchensis* (Sitka spruce) and *Abies lasiocarpa* (subalpine fir) from ~ 29.5 ka through 22.6 ka (thousands of calibrated years median before present) (See Appendix B, Fig. 3-S2). These two species are rarely found together today with the exception of cold parkland settings in SE Alaska (latitude 55.6°N) (Fig. 3-1) (16).

3. ACCELERATED SEDIMENT PRODUCTION DUE TO FROST WEATHERING RATHER THAN PRECIPITATION

Given the presence of tree species characteristic of periglacial settings, plant species and sediment color indicative of a nitrogen-poor regolith (13), an abrupt increase in grain size in the sediment core relative to forested intervals, and a 2.5x increase of erosion rates, we hypothesize that frost weathering accelerated sediment production during the LGM in our study area. Our hypothesis runs contrary to evidence suggesting that the OCR is a steady state landscape, where erosion balances uplift and topography is

time-invariant over glacial-interglacial timescales (4, 17, 18). Importantly, LGM climate simulations and fossil records (14) both indicate drier conditions during the LGM, which precludes increased discharge and runoff as a means to increase sediment flux (Appendix B, Fig. 3-S3). Rather, we hypothesize that vast areas south of the Laurentide ice sheet were subject to frost weathering during the LGM.

Because our paleoarchives indicate colder, drier LGM climates compared to the modern (Fig. 3-2), we model frost-driven processes during this climatic interval.

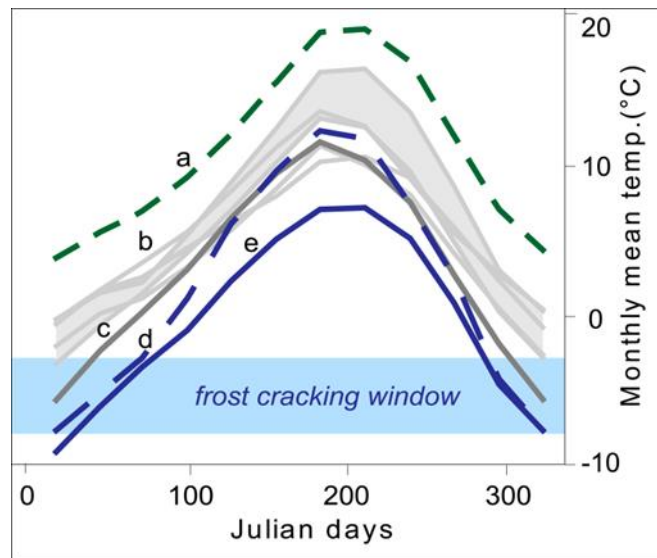


Figure 3-2. Comparison of annual temperature curves based on: mean monthly temperature data for modern Little Lake (a-dashed green line), the range of data from downscaled paleo simulations with temperatures above the frost-cracking window (b-grey band with CCSM4, GISS-E2-R, ISPL-CM5A-LR, MPI-ESM-P, and MRI-CGM3 delineated with light grey lines), COSMOS-ASO (c- solid grey line), Hyder AK climate station data (d-dashed blue line), and MIROC-ESM data (e- blue line). All paleo model data is from CMIP5/PMIP3 simulations (*Methods*).

Theoretical, experimental, and field studies indicate that segregation ice growth contributes to bedrock erosion and regolith transport (11). Bedrock fracturing occurs when ice lenses grow in pore spaces at temperatures between approximately -3°C and -8°C (19–21). Frost damage caused by the growth of segregated ice lenses is vigorous at these temperatures; at warmer temperatures, the pressure exerted against pore walls is too low, while at colder temperatures, ice impedes the liquid water migration required to supply lens growth (19). Frost damage occurs when mobile water wets the interfaces between ice and pore walls (22) and a temperature gradient induces differential interfacial forces that cause crack growth and regulate the magnitude of the liquid pressure gradient

that draws additional water from warmer regions. Hydraulic resistance increases as the temperature drops and the pore space progressively fills with ice (11, 19). Because the pressure gradients that drive liquid flow increase with temperature gradients, and the thickness of the most impermeable zone adjacent to each growing lens scale inversely with the temperature gradient, our model quantifies the intensity of frost weathering as a simple increasing function of the temperature gradient. Our focus on the enhanced hydraulic resistance provided by the most ice-clogged pores is justified by the permeable nature of the sandstone parent rock in our study area. We note that for rocks with much lower intrinsic permeabilities, an alternative formulation (20) may be justified that imposes a significant additional limitation to the frost-cracking rate with increased separation from unfrozen regions, although this alternative formulation is not consistent with either existing data or theory (11, 19, 23). Because OCR hillslopes are steep ($>35^\circ$) and frost-generated regolith transport rates are rapid (10), regolith cover is not likely to limit the pace of sediment production over geomorphic timescales. Thus, we adopt a modified version of a field-verified frost-cracking model (21, 24) to estimate the occurrence of frost-driven weathering and erosion during the LGM.

We define the frost-weathering index as the annual integral of the depth-integrated daily temperature gradient ($^\circ\text{C}\text{-day}$) for substrate within the -3°C and -8°C temperature range. Inter-annual temperature variability, which results from local insolation patterns and the strength of ocean-atmosphere and land-surface interactions, produces annual temperature curves best represented by two harmonics rather than a simple sine wave. Thus, we integrated harmonic functions for the 1D surface heat-flux boundary conditions (25, 26). The model calculates daily temperatures at the surface and at depth based on the mean annual temperature (MAT), a thermal diffusion coefficient (α), and the harmonic coefficients. In our model, the amplitude of seasonal temperature variations and MAT are the dominant factors controlling the vigor of frost weathering at a given location. A contour plot of frost cracking intensity as a function of amplitude and MAT thus provides a framework for predicting frost weathering intensity across a range of conditions (Fig. 3-3, Appendix B, Fig. 3-S4). Zones of high frost cracking intensity are predicted with MAT values just above and below 0°C where summer to winter variation is high (which generates steep temperature gradients when rock passes through the frost

cracking window). As MAT increases above 0°C (or decreases below 0°C), enhanced frost weathering is predicted given concurrent increases in the annual temperature amplitude (Fig. 3-3).

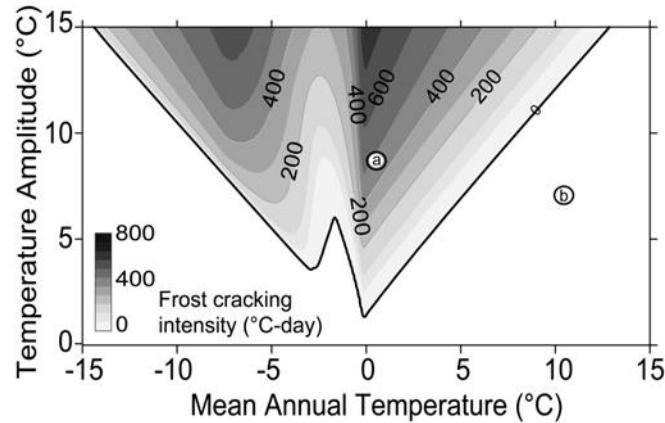


Figure 3-3. Model output of frost cracking intensity for peak amplitude ranging between 0 and 15 and *MAT* ranging between -15°C to 15°C, representing earth’s range of annual temperature variability. *MAT* and amplitude values for Little Lake at 21 ka and the present are delineated by ‘a’ and ‘b’, respectively, on the plot.

In order to quantify the intensity of frost weathering at geomorphically relevant scales in our study area, we employ downscaled CMIP5/PMIP3 (Coupled Model Intercomparison Project Phase 5/Palaeoclimate Modelling Intercomparison Project Phase 3) simulations to generate mean monthly temperature data (27–29). Generally, LGM simulations have a “warm-bias” in *MAT*, primarily generated by insufficient winter cooling (28). We selected the most appropriate CMIP5/PMIP3 models by comparing paleotemperature simulations downscaled to Little Lake with mean monthly temperature data from Hyder, AK, a representative modern environmental analogue (16), based on the LGM macrofossil flora documented in our sediment core from the Little Lake watershed (Fig. 3-2). Only two climate models produce annual temperature cycles similar to the modern analogue. Although the COSMOS model simulations provide a better fit in the warmer months, the MIROC model simulation most closely conforms to the paleoecological constraints imposed by our Little Lake study site (Fig. 3-2).

We calculated frost weathering intensity across western Oregon during the LGM by combining our frost-cracking model with the mean monthly temperature data derived from the downscaled MIROC paleoclimate simulations (Figs. 3-2 and 3-4B). In western

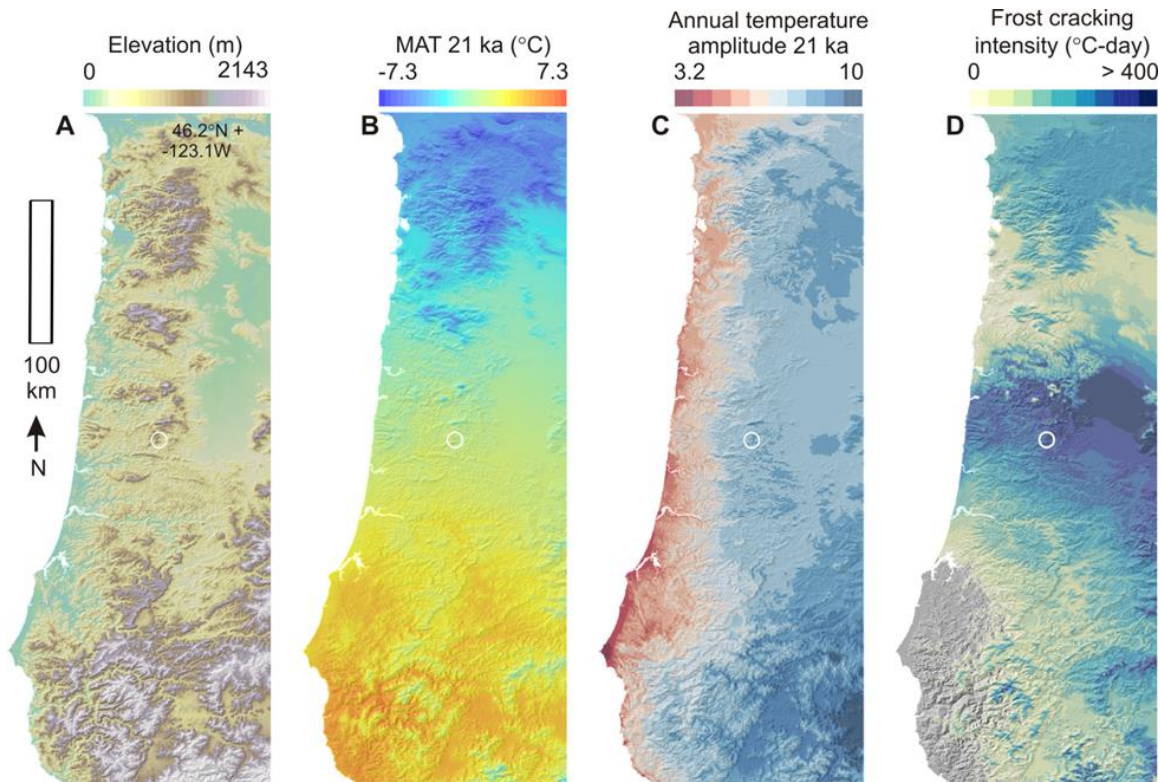


Figure 3-4. Maps showing elevation, MAT, annual amplitude and frost cracking intensity 21 ka. All data overlay on present-day hillshade map delineating the continental extent of the Oregon Coast Range study area. Downscaled paleo-data adjusted for continental extent 21 ka. White circle delineates Little Lake study area. (A) Present-day study area elevation (B) Mean annual temperature ~21 ka based on downscaled MIROC model output. (C) Amplitude values (half the total temperature range) 21 ka based on mean monthly temperature data. (D) Frost cracking intensity ~21 ka in the Oregon Coast Range.

Oregon, bordered by the Pacific Ocean, elevations range from 0 to 2143 m, and paleo MATs decrease with elevation (Fig. 3-4A-B) and latitude (Fig. 3-4, Fig. 3-S5). The amplitude of annual temperature cycles increases towards the east, with increased distance from the buffering influence of the Pacific Ocean; topography also has an effect, with low amplitudes on mountain crests and high amplitudes in valleys (Fig. 3-4C). Hence, the highest frost-cracking intensity during the LGM is not at higher elevations, as our model predicts for the modern climate, but rather in low elevation settings, due to greater winter-to-summer temperature fluctuations. Only the southwestern tip of the OCR (42° - 43°N) shows no frost cracking during the LGM, with the exception of mountain crests, where MATs (~2°C) generate frost cracking despite low temperature amplitude

values (Fig. 3-3, 3- 4). Together, the influence of ocean, land, and ice-sheet proximity during the LGM result in frost weathering across 90% of our study domain (Fig. 3-4D).

4. CONCLUSIONS

Our results encourage a reassessment of conceptual models for how glacial-interglacial climate change manifests in unglaciated terrain (6, 7). Temperature may be the dominant control on increases in sediment production, rather than precipitation, which is commonly invoked. Additionally, increased erosion during the Pleistocene (3, 30) in mid-latitude settings may be largely attributable to frost-derived sediment fluxes emanating from extensive unglaciated terrain. While a functional relationship has not been established to relate frost-cracking intensity to erosion, our data and others (12, 24, 31) suggest that frost weathering is a key control on sediment production. Our results, combining mechanistic theory with temperature reconstructions informed by the geologic record and physical geography, provide a means to resolve the extent to which unglaciated landscapes deviate from modern process mechanisms and rates due to climate fluctuations. Modeling the efficacy of frost processes across mountains and valleys, which is tempered by elevation, and proximity to large water bodies and ice-sheets, amongst other factors, provides a framework to assess how the legacy of past climates influences modern surface processes, such as soil development and ecosystem dynamics. Our results suggest that broad swaths of continental landscapes likely experienced accelerated sediment production via frost processes during glacial intervals, inviting a re-evaluation of what constitutes a steady-state landscape.

5. MATERIALS AND METHODS

Sediment Core. We employed mud rotary drill rigs to collect near-continuous core samples from the paleolake surface through 63 m of sediments to the original valley bedrock. After removing the intact 63.5 mm diameter cores from their metal casings, we split the cores in lengthwise sections and visually described all sections. Using ^{14}C from macrofossils, we constructed a depth-age model. To construct the depth-age model we used a monotonic spline fit to the measured depths and the best-modeled median calibrated ages (See Appendix B Little Lake Paleoclimate Archives, Table 3-S1),

generated with the CLAMS model (ver. 2.2 <http://chrono.qub.ac.uk/blaauw/clam.html>) (32).

¹⁰Be Erosion Rates. The interpretation of paleo-erosion rates requires consideration of cosmogenic nuclide accumulation during hillslope erosion, sediment transport, and sediment deposition. The Little Lake watershed is steep, dissected, and subject to colluvial mass wasting processes. In addition, the area features a uniform sandstone lithology and thus is well suited for inferring erosion rates from the cosmogenic nuclide ¹⁰Be. The topography suggests minimal potential for sediment storage upstream of the lake deposits (Appendix B, Fig. 3-S1). Topographic analysis of our lidar DEM data and sedimentological evidence in the core support a deepwater setting, which would rapidly attenuate post-secondary cosmic rays, so we have not corrected for nuclide production during or after sediment deposition. We estimated erosion rates with spatially averaged production rates determined using LiDAR-derived basin hypsometry (Appendix B, Table 3-S2). We used our depth-age model to derive dates for the paleoerosion rate data. Modern erosion rates were determined from in-stream sediments collected from channels above the influence of the paleolake. All ¹⁰Be ratios calibrated to 07KNSTD (33), measured at PRIME Lab (Purdue University). It is important to note that cosmogenic nuclide analysis determination requires subtraction of a process blank to account for the small amount of ¹⁰Be introduced in the laboratory. At the time our samples were processed there was an unusually high process blank due to contaminated reagents in the chemistry lab. Although the blank was high, it was reproducible for all samples processed at this time, and so we can confidently subtract the blank value from our measurements. This subtraction, together with the low ¹⁰Be concentrations in the samples, has led to unusually high uncertainties for our erosion rates (10-30%). The change in erosion rates that we observe from LGM to modern far exceeds these uncertainties. Table 3-S2 (Appendix B) contains more details on the erosion rate calculations.

Frost Cracking Model. We employ an analytical solution for 1-dimensional heat conduction appropriate for annual temperature variations (26):

$$T(z, t) = MAT + e^{-z\sqrt{\frac{\pi}{\alpha P_y}}} \left(A_1 \cos\left(\frac{2\pi t}{P_y} - z\sqrt{\frac{\pi}{\alpha P_y}}\right) + B_1 \sin\left(\frac{2\pi t}{P_y} - z\sqrt{\frac{\pi}{\alpha P_y}}\right) \right) + e^{-z\sqrt{\frac{2\pi}{\alpha P_y}}} \left(A_2 \cos\left(\frac{4\pi t}{P_y} - z\sqrt{\frac{2\pi}{\alpha P_y}}\right) + B_2 \cos\left(\frac{4\pi t}{P_y} - z\sqrt{\frac{2\pi}{\alpha P_y}}\right) \right) \quad (3-1)$$

Where T is daily temperature, z is depth, t is time, MAT is the mean annual temperature calculated from monthly mean temperatures, α is the thermal diffusion coefficient, P_y is the time period for the curve (we use an annual cycle) and A_1 , B_1 , A_2 , B_2 are coefficients of a Fourier series fit to monthly temperature data extracted from the paleoclimate simulations. In the present context, A_1 and B_1 jointly control the amplitude and the phase of the annual temperature cycle (i.e. the first harmonic of the monthly temperatures), while A_2 and B_2 control the asymmetry of the cycle. We set α to $0.01 \text{ cm}^2 \text{ sec}^{-1}$. Previous 1D heat conduction models disallowed frost cracking when surface temperatures froze water $\leq 0^\circ\text{C}$ (20, 21, 34). However, field and experimental evidence suggests that frost cracking persists due to an active water layer below the surface ice lens (11, 35). Thus, we follow previous methods in calculating frost cracking intensity (20, 21), with a modification that relaxes the restriction against frost cracking when the surface temperature is $\leq 0^\circ\text{C}$. We now set the criteria to $T > 0^\circ\text{C}$ at the surface or at depth to allow for bidirectional freezing and frost cracking in warm permafrost settings.

Paleoclimate Reconstruction. We downloaded climate-model output for the LGM (*lgm*) and control (*piControl*) simulations from the from the Coupled Model Intercomparison Project Phase 5 (CMIP5) web sites. The CMIP5 models selected included: CCSM4, COSMOS-ASO, GISS-E2-R, ISPL-CM5A-LR, MIROC-ESM, MPI-ESM-P, and MRI-CGM3. We used the last 100-years of monthly data for near-surface air temperature (*tas*). We also obtained 30-yr monthly mean maximum and minimum temperature data (*tmin* and *tmax*) from the “800 m” (30-second) PRISM climate data set (*PRISM Climate Group*, Oregon State University, <http://prism.oregonstate.edu>), and from these we generated monthly average temperatures on the PRISM grid. The monthly average temperature data were then used to calculate local topographic lapse rates for each month of the year (36). The lapse rates and CMIP5 data were both (bilinearly) interpolated onto a 90 m digital-elevation model, applying the lapse rates to generate elevationally-adjusted monthly temperatures on the grid (36). Utilizing seven

CMIP5/PMIP3 simulations and the ensemble average, we generated monthly *lgm* minus *piControl* long-term mean differences (or “anomalies”). We then added these long-term mean differences to the present-day 90 m grid to produce a map of simulated LGM monthly temperatures.

We compared model output at location 44.18°N, -123.56° W, a representative location in the Little Lake watershed, midway between the valley floor and ridgetop elevations, at 400 m, to present-day mean monthly temperature data for a similar representative location near Hyder, AK, our analogue landscape, at 500 m (55.914° N, -130.024°W), using ClimateWNA (*ClimateWNA*, University of British Columbia, <http://climatewna.com/>) (37).

Model Implementation. Using the downscaled paleoclimate simulations, we calculated MAT and the shape coefficients by fitting a 2-term Fourier series to the monthly temperature data and the median Julian day within each month for each grid node within our study domain. We then use Eqn. 1 to calculate frost cracking intensity. For computational efficiency, we subsampled the 90-m grid to a 270 m interval.

6. BRIDGE

This chapter presented a snapshot in time 21 ka to demonstrate that frost weathering was pervasive across broad swaths of the modern temperate continent. Ultimately, if we are to understand how climate intervals imprint on modern landscapes and modulate variations in flux and form, we need both spatially broad (e.g. this chapter) and temporally extensive research (Chapter IV). In the next chapter I present erosion rates from the Little Lake Core, extending over MIS 3 through MIS 1. I combine this data with paleoenvironmental reconstructions to demonstrate that erosion rates track climate-modulated changes in bedrock to soil production mechanism through time. Combined, these two studies refute previous studies that suggested climate has a minimal influence on erosion rates. Rather, the results demonstrate the limits of probing modern landscapes exclusively to understand past processes.

CHAPTER IV

LATE QUATERNARY CLIMATIC CONTROLS ON ECOSYSTEMS, PROCESSES, AND EROSION RATES OVER MILLENNIAL TIME SCALES IN THE PACIFIC NORTHWEST

I carried out the work described in this chapter with the guidance of Dr. Josh Roering, Dr. Daniel Gavin and Dr. Darryl Granger. All these coauthors contributed substantially by offering regular input and feedback on results. Dr. Roering offered comments on earlier drafts of the manuscript. I did all the writing.

1. INTRODUCTION

While tectonics and volcanism uplift and construct topography, climate-mediated processes control the style and pace of landscape response. Under conditions of steady uplift, process feedbacks steer landscapes towards a dynamic equilibrium, such that erosion balances uplift over long timescales (Ahnert, 1994; Hack, 1975). However, it is unclear how variations in climate forcings disrupt landscape trajectories towards steady state (Chorley et al., 1984). For example, in many settings, ranging from temperate to tropical, we are yet unable to predict if climate change will induce increased or decreased erosion and if responses such as river incision or aggradation are gradual, a function of the timescale of change, or invoke a threshold change resulting in a new equilibrium (Chorley et al., 1984; Tucker and Slingerland, 1997). Additionally, it is possible that glacial-interglacial intervals impose a cyclic disequilibrium due to repeated perturbations (Zhang et al., 2001), prevalent since the onset of increased climatic variability during the Pleistocene (Molnar, 2004). Alternatively, landscapes may be responding primarily to climate-driven processes that result in the greatest landscape change (e.g. changes in base level or erosion rates), such that a particular climatic interval, rather than the fluctuations, dominates in disrupting steady-state trajectories (Chorley et al., 1984).

In modern landscapes, one can observe intense chemical weathering of saprolite and soils via precipitation in wet, warm climates, physical disruption of bedrock and soil via biota in temperate climates, and the wholesale removal of soil and underlying rock via glaciers in cold climates. However, landscapes are often polygenetic with modern

processes acting on terrain shaped by past tectonics and weathering and hydrologic routing patterns (Barry, 2013; Bull, 1991; Chorley et al., 1984; Slim et al., 2015). Thus, past forcing mechanisms such as climate potentially define the architecture upon which present-day processes operate (Anderson et al., 2013; Vasconcelos et al., 1994). Despite modern-day observations, we lack understanding of how climate-mediated ecological changes (e.g., temperate forests transitioning to xeric grasslands) dictate variations in rock damage, soil production and transport rates. This knowledge gap hampers progress in a broad array of problems in geomorphology and Critical Zone science such as: quantifying fluxes of sediments and solutes, modeling landscape response to past and present climate change, including the regulation of global CO₂ by silicate weathering, understanding the template that modern processes operate on, and predicting the trajectory of future change (Anderson et al., 2013; Committee on Basic Research Opportunities in the Earth Sciences, Board on Earth Sciences and Resources, 2001; Dietrich and Perron, 2006; Dietrich et al., 2003). In this contribution, we couple high fidelity paleo-erosion and paleo-environmental data with paleo-climate reconstructions from a 50 ky sediment archive spanning three Marine Isotope Stages (1-3) to quantify how climate-mediated ecological changes influence erosion rates, if at all.

2. BACKGROUND

2.1. Early approaches to illuminating climate's role

Sedimentary deposits and river terraces provided a rich data source for early geologists seeking clues to past climates and landscape response. Influential early geomorphologists, especially Davis (1899) and Penck (1910), characterized the modern climate as 'normal', particularly as applied to the familiar, settled, temperate soil-mantled landscapes (Barry, 2013; Bryan, 1950). Glacial and arid landscapes were 'climatic accidents'. Davis propagated a framework in which the morphology of temperate, humid climates was considered the norm, and fluvial, weathering and erosional processes of the present dictated the form of modern landscapes, projecting into the past (Barry, 2013; Bryan, 1950; Chorley et al., 1984)

Early geologists such as Gilbert (1890) formulated theories on climate change after working in the arid west and noting landscape records of vast pluvial lakes in

modern dry deserts. Observations of flights of river terraces (e.g., Huntington et al., 1914) perched high above modern river beds suggested fluctuations in sediment supply or river discharge through time, as rivers bevel horizontally when transport limited and downcut vertically when supply limited or when base level is falling. Prevalent climate-driven models predict the same outcome for opposing climate forcings (Tucker and Slingerland, 1997). Huntington et al., (1914) proposed that as climate cooled and dried, the loss of vegetation would lead to stream aggradation, with stream incision attributed to warmer, more humid intervals. Conversely, (Bryan, 1940, 1928) suggested that in colder drier climates, less vegetation would lead to increased runoff and glacial interval incision, with aggradation attributed to interglacial intervals. Bull (1991) extended this empirical approach, by reconstructing coincident denudation and climate records, extending Huntington in attributing aggradation to cold climate vegetation loss.

Diverse landscape features and tools ranging from paleosoils (e.g., Retallack, 2008; Vasconcelos et al., 1994), thermochronometers (e.g., Herman et al., 2013), river terrace deposits (e.g., Bull, 1991), lakes and other depositional settings (e.g., Hendy et al., 2002) are used as a record of landscape response to climate and climate change. However, it is difficult to extract a detailed record of climate controls on sediment production rates using these types of data. Over long timescales (> 100,000 yrs), changes in tectonic forcing and catchment reorganization can complicate efforts to disentangle the role of climate on erosion change through time (Balco and Stone, 2005; Willett et al., 2014). Even at shorter timescales, landscape features such as terraces may only record episodic events and the spatial extent of contributing upstream processes can be difficult to decipher.

2.2. Climate - scales and tools

Climate, and the changes wrought, controls landscape processes at timescales ranging from millions of years to minutes. Widespread deposits of deeply-weathered paleosoils, dated as mid to late Eocene, indicate a major episode of warmer and wetter conditions prevalent over tens of millions of years ago which imprinted on modern landscapes (Vasconcelos et al., 1994). With the arrival of the Plio-Quaternary ice ages, and the transition from a climate where changes were slow and rare to orbital-driven glacial and inter-glacial intervals, climate began to affect landscape processes at temporal

scales of ~ 50 to 100 ky (e.g. Ahnert, 1994, 1976; Whipple, 2001). Complications arise when trying to disentangle the timescales of landscape response to orbital fluctuations vs. response to other perturbations (e.g., hillslope response to seismic events) as the two tend to correspond. At smaller timescales, events such as the millennial-scale Younger Dryas cooling event (~ 12.8 to 11.5 ka) (thousands of calibrated years median before present) and century-scale Dansgaard-Oeschger events, can interrupt longer climatic trends such as the modern interglacial interval. Sedimentary records from tsunamis, earthquakes, and floods record near-instantaneous high magnitude but low frequency perturbations.

In 1976, Luna Leopold declared that the greatest question facing hydrology was “How great a change, in what climatic factors are needed to change by a measureable amount production of water and sediment from a basin” (Leopold, 1976). He went on to state that it is probable that the question, as stated, could never be answered. With the advent of cosmogenic radionuclides (CRN), we are now able to measure erosion rates over millennial time scales (Kirchner et al., 2001). Cosmogenic nuclides, with applicability over timescales of 10^3 to 10^5 years, overlap with the timescales in which rocks weather, soils form, climates cycle between glacial and interglacial, and rivers incise or aggrade (Granger and Schaller, 2014). Thus, cosmogenic nuclides allow for consideration of the rates of rock weathering and erosion over the same timescales that climate interval fluctuations imprint on the land, providing a critical tool unavailable to earlier researchers.

Enhanced by technological advances, recent studies have begun to identify mechanistic explanations for linkages between changes in precipitation or temperature and soil production and denudation. Combining luminescence dating, remote sensing and lithologic analysis, Blechschmidt et al. (2009) disentangled high sediment production during arid periods from monsoon-induced sediment delivery to alluvial megafans. In the French Alps, CRN-derived erosion rates increase with increasing elevation, co-varying with temperature and the relative intensity of frost weathering (Delunel et al., 2010), suggesting a mechanistic link between temperature and bedrock erosion (Hales and Roering, 2007; Walder and Hallet, 1985). In the Atacama Desert, Chile, CRN-derived erosion rates decrease rapidly across the arid-to-hyperarid transition, reflecting a transition from biotic to abiotic conditions (Owen et al., 2011). In the unglaciated Oregon

Coast Range, ^{10}Be -derived erosion rates are $\sim 2.5\times$ greater during the Last Glacial Maximum (LGM) than modern rates, attributed to abiotic frost processes during the LGM compared to biotic processes during the Holocene (Chapter 3). Conversely, Hughes et al., (2009) found that soil transport rates doubled at the Pleistocene-Holocene transition, coincident with the transition from grasslands to closed forests. Despite recent advances, the legacy of past climates in soil-mantled settings is difficult to discern, as the topographic evidence such as solifluction lobes is often bioturbated by vegetation, and, in tectonically active areas, signals are quickly erased and sediment records are hard to find.

At present, with few exceptions (Anderson et al., 2013; Kirkby, 1995; Tucker et al., 2011) landscape evolution models often ascribe processes active in the modern when evaluating landscape evolution through time (e.g. Dietrich et al., 2003; Roering, 2008). This is a reasonable assumption given a lack of data on how unglaciated soil-mantled terrain responds to forcings under different climate regimes, if at all. To better understand how variations in temperature or precipitation may control landscape response, one approach is to quantify changes in sediment production or erosion rates across a suite of study sites, with similar lithology but differences in precipitation or temperature regimes. For example Riebe et al, in a set of seminal studies (Riebe et al., 2001a, 2001b), found little correlation between temperature or precipitation and CRN-derived erosion rates in across the Sierra granites with mean annual temperature (MAT) ranging from 4 -15 °C and mean annual precipitation ranging from 20-180 cm yr⁻¹. However, regional variations in tectonic settings, stress history, rock properties, and the state of landscape adjustment limit the utility of this approach. Because of each sites unique history, processes may vary with climate, but so may site attributes. For example lithologic-derived nutrient availability (Hahm and Riebe, 2014) or fracture density (Marshall and Roering, 2014) in seemingly uniform lithologies may control vegetation density such that increasing precipitation has little influence on tree-driven soil production. Thus, space for time substitutions problematically may preclude comparing the magnitude of different climate-controlled processes operating on the terrain, as climate may not be the only controlling variable (Pederson et al., 2001). Alternatively ‘drilling’ through time at a single location, undergoing steady tectonic forcing, allows for evaluating climate-controlled processes and potential erosion variation through time.

2.3. Coupling paleo-data, and modern geochemistry tools to discern mechanistic links between climate change and landscape evolution

Paleoarchives such as lake sediments provide an alternative to studying diverse processes and erosion rates, for by quantifying erosion rate change through time in a single setting, it is possible to eliminate tectonic and lithologic variation. An ideal paleo-setting would span more than one climatic interval (e.g., Marine Isotope Stage), in a single quartz-rich lithology (for CRN-derived erosion rates), in a quiescent sedimentary environment such as a deep sea basin or small lake, with direct hillslope-to-basin deposition, and contain abundant proxy data such as fossils for inferring millennial-scale climate variations (Jerolmack and Paola, 2010; Schumer et al., 2011; von Blanckenburg, 2005).

As described below, Little Lake, a remnant of a much larger paleolake deposit in the Pacific Northwest Oregon Coast Range (OCR), well-studied by paleo-ecologists, provides an near-ideal setting for quantifying the mechanics of climate-induced erosion rates with high fidelity through time (Fig. 4-1). Little Lake ^{10}Be -derived erosion rates were consistently at least 2.5x higher during the Last Glacial Maximum (LGM) compared to modern rates (Chapter 3). In this study, utilizing previous studies and data from a new sediment archive, we seek to discern mechanistic links between climate, ecosystem changes, and hillslope soil production and erosion processes over glacial and interglacial intervals in a non-glaciated soil-mantled setting. The OCR, including Little Lake, remained unglaciated during MIS 2 when the Cordilleran ice sheet extended at most 320 km to the north of Little Lake (Orr et al., 1992). We hypothesize that climate-induced changes in ecosystems will significantly change bedrock disruption, soil mixing and transport mechanisms such that we can distinguish how climate modulates sediment production, mixing depths, transport, and erosion. By coupling ^{10}Be -derived erosion rates, sediment archive observations, and vegetation-derived climate data extending ~50 ka to present extracted from a near-continuous paleolake core, we quantify at millennial-scale resolution a tight coupling between climate change, ecosystems and erosion rates from the pre-LGM (Marine Isotope Stage, (MIS) 3) (50-26 ka), glacial (MIS 2) (26-13 ka) and modern inter-glacial (MIS 1) (13-modern) intervals.

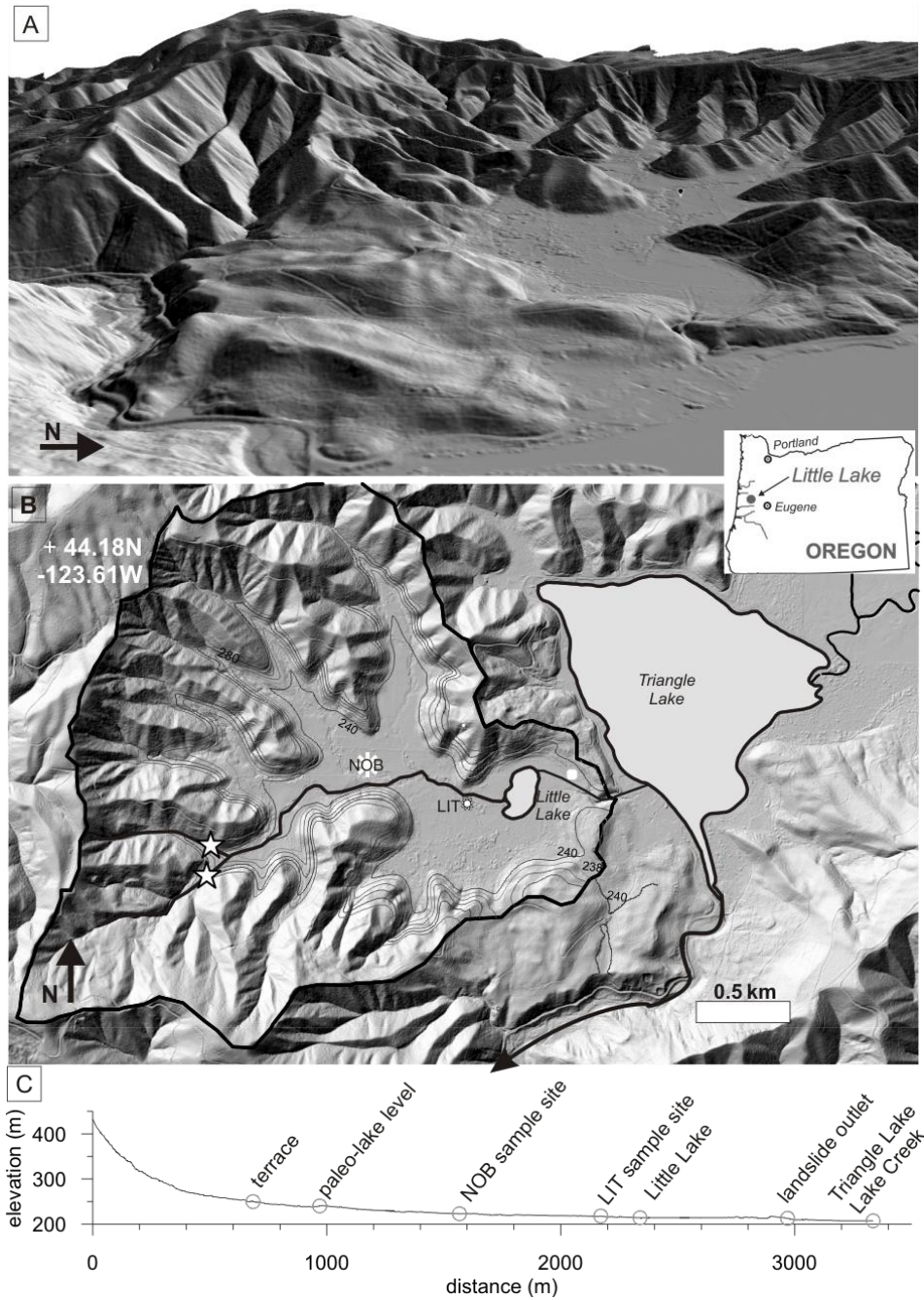


Fig. 4-1. Little Lake catchment and sample sites. A) Perspective view of the Little Lake basin with landslide deposits and Triangle Lake in the foreground. View is rotated with north to the right. B) Map of the Little Lake catchment and sample sites. Modern stream sample locations delineated with stars. Core data locations marked with asterisks (labeled NOB, LIT). Previous paleoecology data collected in the fens near the Little Lake outlet marked with a polygon. Map shows only a portion of the larger landslide-dammed paleolake deposit which extends to the east of modern Triangle Lake. Contour lines on the map are at 10 m intervals and highlight bench-cut terraces and abandoned spillway. C) Longitudinal transect from catchment above NOB sample site to lake outlet.

Below we first provide a geologic and geomorphic overview of the well-studied Oregon Coast Range and describe the Little Lake setting, as well as previous Little Lake studies. We then present our methods and provide a brief background on the use of cosmogenic nuclides and steady state landscape formulations applied to landscapes with variable erosion rates. As variable soil mixing depths and soil production rates (due to climate-driven ecosystem and process changes) can influence measured erosion rates through time when using cosmogenic-nuclides to derive actual erosion rates, we present a conceptual soil production model used to predict mixing depths through time. This conceptual model underlies erosion rate simulations, allowing us to constrain actual erosion rates from the measured depth and time integrated ^{10}Be erosion rates.

3. GEOGRAPHIC SETTING AND PREVIOUS STUDIES

3.1. Oregon Coast Range

The well-studied, unglaciated, soil-mantled Oregon Coast Range (OCR) is a steep and highly dissected mountainous landscape with relatively uniform ridge and valley form (Dietrich and Dunne, 1978; Reneau and Dietrich, 1991). OCR precipitation averages 1-2 m annually, falls predominantly in the winter, and is rainfall-dominated, with rare snow at higher elevations, but lacking persistent snow cover. The summers are generally dry, and mean annual temperatures average $\sim 11 \pm 1^\circ\text{C}$ (mean \pm sd) (PRISM Climate Group, Oregon State University, <http://prism.oregonstate.edu>). This wet, temperate climate supports a closed canopy forest dominated by Douglas-fir (*Pseudotsuga menziesii*) and western Hemlock (*Tsuga heterophylla*). The underlying lithology, primarily the Eocene Tyee formation, is a quartz-rich sequence of uniform, little-deformed, rhythmically bedded turbidite sequences overlying accreted volcanic basement (Heller and Dickinson, 1985; Orr et al., 1992).

The OCR is often considered an ideal representation of steady state topography (Montgomery, 2001; Reneau and Dietrich, 1991; Roering et al., 1999, 2001, 2007) as numerous studies suggest millennial-scale erosion rates estimates (e.g., Balco et al., 2013; Bierman et al., 2001; Heimsath et al., 2001) are approximately in balance with tectonic uplift (Kelsey et al., 1996). Uplift of the Tyee Formation began in the Miocene (McNeill et al., 2000) and is still active today as evidenced by uplifted wave-cut platforms (Kelsey

et al., 1996). Long-term uplift rates in the Oregon Coast range from 0.05 to 0.3 yr⁻¹ mm yr with much of the variation in uplift rates due to structural controls along the coast (Kelsey et al., 1996). Cosmogenic nuclide-derived erosion rates derived from stream sediments average 0.11 ± 0.03 mm yr⁻¹ (Balco et al., 2013; Bierman et al., 2001; Heimsath et al., 2001). Short-term or localized erosional variability is a reflection of stochastic processes (Heimsath et al., 2001, 1999; Sweeney et al., 2012) and rock properties (Heimsath et al., 2001; Marshall and Roering, 2014). Shorter-term studies (decadal to millennial) based on sediment yield or radiometric dating of basal colluvium surfaces have focused on the repeated fill and evacuation of soil in steep, convergent areas, where erosion rates range from 0.05 to 0.3 mm yr⁻¹ (Beschta, 1978; Reneau and Dietrich, 1991).

Biogenic physical weathering processes dominate modern soil production, specifically tree-driven bedrock to soil conversion (Heimsath et al., 2001; Roering et al., 2010). Anderson et al. (2002) calculated that approximately 10% of mass removal in the Tye Formation is chemical, suggesting that denudation is dominated by physical processes. Soils are generally thin on noses and side slopes with average depths of less than 0.5 m (Heimsath et al., 2001; Reneau and Dietrich, 1991; Roering et al., 2010). Soils are thicker (~ 1m) in unchanneled hollows, and provide source material for shallow landslides that can initiate valley-carving debris flows (Dietrich and Dunne, 1978; Stock and Dietrich, 2006).

In contrast to the ‘typical’ steep, highly-dissected terrain of the OCR, low-relief, deep-seated landslides also occur throughout the OCR (Roering et al., 2005), and while locally important, in this study we focus on processes and erosion rates in the more prevalent steep and dissected hillslopes of the OCR.

3.2. Little Lake Basin-physiography

The Little Lake catchment, located in the central portion of the OCR (Fig. 4-1), is comprised of characteristic Tye Formation morphology with steep, highly dissected hillslopes. Little Lake, along with the adjoining Triangle Lake, formed ~ 50 kya (Section 5.2) as the result of a structurally controlled deep-seated landslide. The landslide dam separates present-day Little Lake from Triangle Lake, though the beveled nature of the top of the dam deposit and terrace levels on the adjoining hillslopes suggest that Little

Lake and Triangle Lake may have been part of a single paleo-lake in the past. The Little Lake catchment area, as measured from the watershed divide to the outlet dissecting the landslide deposit, is 8 km². The areal extent of the Little Lake sedimentary deposit is ~ 1km² and the deposit is over 60 m thick (Oregon Water Resource Department, well log data http://apps.wrd.state.or.us/apps/gw/well_log/Default.aspx).

Lidar data, acquired by the National Center for Airborne Laser Mapping, illuminates the landslide deposit that created the paleolake as well as the distinct difference between the deep-seated landslide and the Little Lake watershed morphology (Fig.4-1A). The lack of hills in the central, open portion of the larger Triangle Lake valley, as well as the low-relief hummocky form of the hillslopes bordering Triangle Lake suggests that multiple deep-seated landslides may have pre-dated the most recent lake-forming landslide. Importantly, the lidar data allows us to query the terrain to better understand the Little Lake depositional setting and history.

Based on the elevation of the valley sediments, the paleo-lake level was at a minimum ~ 40 m higher than Little Lake's present elevation of 217 m above sea level (MASL), with continuous paleo lake deposits evident at 260 MASL (Figs. 4-1B-C). Bench-cut terraces visible on the adjoining hillslope suggest lake levels were likely as high 290 MASL (Fig.4-1B). Little Lake outflows bisect the landslide dam (213 MASL) before flowing into Triangle Lake. The bedrock-controlled Triangle Lake outlet (207 MASL) discharges into Lake Creek, a large tributary of the Siuslaw River (Fig. 4-1C). An uncharacteristic broad u-shaped valley with fluvial gravels lies just to the southwest of modern Little Lake outlet. This abandoned spillway is at approximately the same elevation as the top of the landslide dam (240 m MASL), suggesting that the paleolake likely at times drained directly into Lake Creek.

3.3. Little Lake Basin - previous paleo-environmental findings

Lake core data (pollen and plant macrofossils) collected from Little Lake in the distal fen (Fig. 4-1B) by Worona and Whitlock (1995) provide a continuous record of late Quaternary climate change from 42,680 calibrated years before present (cal yr BP.) to 250 years BP. The core contains a 1-cm thick layer of well-preserved ash from the Mt. Mazama eruption dated at approximately 7.6 ka (Sarna-Wojcicki et al., 1983). The original core analysis subdivided the record into five major climate regimes over the past

43,000 years (Worona and Whitlock, 1995). Subsequent core analysis (Grigg and Whitlock, 1998, 2002) and new core data from the Little Lake fens (Grigg et al., 2001) provide higher temporal resolution insight into climatic and vegetation variability for some sections of the record. Lake core analyses show that over the last 43 ky, three distinct forest types existed in the watershed. Pollen data spanning the end of the pre-LGM, (43 to 27 cal yr BP, Marine Isotope Stage (MIS) 3), chronicle an open canopy forest assemblage comprised of pine, hemlock and fir, indicating colder (~ 3 °C) and wetter conditions than today. During the last glacial period (MIS 2, 27-15 cal yr BP.), vegetation consisted of a meadow-dominated spruce (*Picea*) and lodgepole pine (*Pinus contorta*) forest, suggesting a colder (by 7-14 °C), nutrient-poor, and overall drier climate than the modern closed canopy Douglas-fir forest. Without being able to determine spruce pollen to the species level, last glacial climate reconstructions were unable to resolve if the climate at Little Lake was closer to modern Cascades, Olympics, coastal British Columbia or maritime southeastern Alaska (Grigg et al., 2001). While the inferred climate for the last glacial fluctuated between wet and dry, mean annual precipitation was on average about 250-500 mm less than present day (Grigg et al., 2001). The core pollen records shift towards warm, moist conditions and temperate, closed-canopy Douglas-fir forests at 13 ka with the onset of the modern inter-glacial interval (MIS 1) (Worona and Whitlock, 1995). Pollen data from Little Lake only weakly registers a potential Younger Dryas event, as a shift in vegetation suggests cooler but not cold temperatures (Grigg et al., 2001).

3.4. A paleo-erosion archive

The Little Lake basin attributes make it an ideal location to test hypotheses on linkages between climate-driven ecosystem changes and millennial-scale variations in erosion rates. Quiescent sedimentary basins such as small lakes present the highest probability of maximizing the preservation of external forcing mechanisms (such as climate change) and recording periodic fluctuations climatic signals (Jerolmack and Paola, 2010; Schaller and Ehlers, 2006). Sediments derived from creep – dominated processes such as tree throw or frost heave are the primary source of basin deposits and represent basin-integrated erosion rates. As the basin is underlain by a single, remarkably uniform, quartz-rich sandstone (Chan and Dott, 1986; Rogers and Lovell, 1969; Snively

et al., 1964), it is ideally suited for deriving erosion rates from quartz grains. The existing high-resolution paleo-climate reconstructions from the basin provide a rich-dataset for coupling paleo-erosion data with vegetation-derived climate data. Additionally, the paleo-environmental reconstructions allow us to consider how climate change manifests as changes in ecosystem-controlled soil production, mixing depths and transport mechanisms. Post-landslide, Lake Creek flows along the upslope margins of the landslide deposit, leaving the paleorecords undisturbed and preserving Triangle and Little Lake levels throughout time (Fig. 4-1B).

4. METHODS

4.1. Site Selection

We chose our primary CRN and paleoecology sample site upstream of the modern lake to satisfy the following criteria and considerations. Given our primary goal of deriving erosion rates from the quartz-rich deposits, we sought to maximize sampling hillslope-derived sediments and thus set our core location in the valley axis proximal to the sediment source area (Fig.4-1B). The samples also required sufficient quartz mass within a < 4cm diameter sampling tube to obtain erosion rates over short (< 1000 years) time intervals from sediments with a size range 0.25 mm – 2 mm (to avoid extra-basin aeolian or coarse landslide inputs). Only two lots in the basin met the sampling criteria, and of the two properties, landowner access effectively narrowed our preferred sites to one feasible site.

4.2. Drilling and core extraction

As described in more detail below, we collected near-continuous samples from the paleolake surface to 63 m depth, with the final core-drive in saprolite underlying the valley lake fill. Our primary core data comes from a cluster of three drill holes, relying mainly on truck-mounted drills (Cores NOB A-C) and hand drilling with a Livingston corer (NOB-I A-R). We also collected samples to a depth of 7.9 m closer to the modern Little Lake with a soil auger and a Livingston corer (LIT-I A-L) (Fig. 4-1B). As most United States drilling companies still rely on English measurement units (e.g., feet and inches) for sampling equipment such as core rods and sample casings, we report English as well as metric units.

At our primary sample site, NOB, we initially employed a truck-mounted hollow-stem auger continuous sampling system (Core NOB A, 44.16876°N, -123.59436°W). Hollow stem augering allows for large diameter core collection in 5' (1.52 m) intervals (in our case segmented into two 2.5', 0.76 m Lexan tubes). Our first core drive began 5 ft (1.52 m) below the surface with poor recovery in our first two drive attempts (5ft-15 ft, 1.52 m – 4.57 m). Sediment only partially filled the sample tubes and the gaps in the core segment precluded precise depth control, necessary to develop a depth-age model. We drilled to 85 ft (25.91m), with increasingly poor to no recovery. From 40 ft (12.19 m) downward, coarse sands and a high groundwater table created an untenable situation, with water-laden sand flowing into the drill hole.

Due to the sand content and high water table, we transitioned to using a truck-mounted mud-rotary drill for an adjacent core recovery effort (NOB B, 44.16867°N, -123.59434°W). The set-up utilized a 2ft (0.61 m) California split spoon sampler encasing four stacked brass or stainless steel tubes, each 0.5ft (0.15 m) long and 1.5 in (3.81 cm) in diameter. Based on well log data and 1D reconstructions of the paleo-valley topography, we estimated the deposit depth at ~60 m. Therefore, we subsampled the upper 29 m of paleo-sediments, with continuous sampling from 30 m downward, constricted by allocated drilling time, onsite equipment, and expense. After 2 days of drilling, additional supplies arrived on-site allowing for continuous core collection in 2ft (0.61 m) increments.

Subsequent to the NOB B core collection, we again employed a mud-rotary drill at our main sample site (NOB) to subsample intervals from 12ft (3.66 m) to 111ft (33.83 m) (NOB C, 44.16862°N, -123.59435°W) to cross-validate sample depths in the NOB B core. On this occasion, the available samplers held either two or four 0.5ft (0.15 m) steel or brass sample tubes. We also collected hand-cored samples (NOB-I) from the surface to 3.65 m before the mechanical drilling operation.

In an effort to collect contiguous paleo-sediments from the Late Pleistocene through the Holocene we hand cored at a site closer to the upstream end of modern Little Lake (LIT, 44.16735°N, -123.58668°W), using a combination of a soil auger and Livingston corer. Compacted fine sediments halted our efforts at 7.9 m below the surface.

All sample intervals, whether extracted manually or mechanically, were logged and labeled onsite and tightly wrapped in plastic before sealing with tape. For NOB B and C cores, we named the samples by the sampler depth (in feet), with the topmost 0.15 m sample tube segment for each drive modified by the letter 'a', the next tube, 'b' etc. For example if the C drive started 20 ft (6.1 m) below the surface, the top-most sample tube (of four) in the split-spoon sampler would be labeled NOBC 20a.

4.3. Sample extraction

In order to extract the tightly packed sediment deposits from 269 15 cm length sample tubes without slicing or disturbing the sediments, we undertook the following steps. We carefully slit each metal casing lengthwise, using a custom-built jig calibrated to the thickness of the sample tube walls, and a horizontal bandsaw fitted with a vacuum nozzle to prevent metal shaving contamination,. Before re-wrapping the now sprung open tube, we removed all metal filings with a vacuum and fine tweezers. To extract the sediments we used a custom-built extruder. We extruded each 15 cm cylinder into a split PVC split pipe before carefully bisecting each sample lengthwise with thin-gauge wire and labeling each half as either a 'working' or 'archive' core. We preserved core chronology by laying the split sediment cylinders end to end in 1.52 m PVC tubes split in half-lengthwise. We visually described each core segment, noting changes in color, laminations, concretions, grain size information, and plant macrofossils. Once logged, labeled, and wrapped, we encased the cores in protective plastic tubes, color coded as working or archive and transferred to a temperature-controlled cooler.

Because of the mud-rotary drilling method (NOB B and C), approximately 10% of the 269 samples had no recovery or driller's mud in the upper centimeters of the sample sequence. The driller's mud was confined to a layer above the sediments in a sample tube rather than coating the tightly packed sediments, and thus was easily avoided when describing the cores.

4.4. Depth-age model

We adopted an iterative sample dating strategy, initially extracting plant macrofossils from the upper part of the core for radiocarbon dating while processing quartz sediments from deeper in the core using optically stimulated luminescence (OSL)

dating methods. All told, we extracted 25 plant macrofossils from the core for ^{14}C dating and 3 sediment segments for OSL dating in order to construct a depth-age model (Tables 4-1, 4-2).

Table 4-1. ^{14}C data

Sample	CAMS ID#	Depth m	^{14}C age years	Error years	Min 95% years	Max 95% years	Median BP
Data and depths used in depth age models and for constraining CRN sample age							
I-L	156944	-2.17	2425	25	n/a	n/a	2.43
I-P	155165	-3.22	18500	50	19.56	20.02	21.63
C14tip	155166	-4.57	19030	50	22.68	23.15	22.91
C20tip	152768	-6.40	19390	70	23.07	23.58	23.33
C40tip	153571	-12.50	19410	60	23.11	23.59	23.35
C60tip	153573	-18.59	19720	70	23.49	23.99	23.75
B74c	156945	-22.82	20150	70	24.00	24.44	24.21
C83a	156946	-25.15	21030	80	25.15	25.60	25.38
B96tip	156032	-29.69	21425	45	25.61	25.89	25.73
B114tip	158582	-36.28	23880	150	27.69	28.62	27.98
B126d	158585	-40.69	25790	130	29.57	30.43	30.03
B140tip	156032	-46.12	31310	110	34.85	35.51	30.11
B156d	158584	-51.85	32970	420	36.18	38.29	37.26
B158b	158592	-52.31	33900	360	37.19	39.15	38.21
B174b	158581	-57.63	40330	1030	42.74	44.09	44.17
B207a	158586	-63.2	45590	1480	46.35	49.93	48.37
Data and depths not used (assumed re-deposited)							
C50a	155167	-15.24	28610	220	23.28	23.71	32.60
C50tip	153572	-15.54	21130	80	23.31	23.72	25.46
B60d	159909	-18.59	25870	690	23.49	23.99	26.69
C91b	159910	-27.89	21690	100	25.47	25.72	25.94
C91c	158580	-28.04	25790	180	25.48	25.73	30.21
C100tip	155167	-30.78	23980	90	25.57	26.11	26.67
All samples processed at Lawrence Livermore National Laboratories Center for Accelerator Mass Spectrometry (CAMS). All samples consisted of a single piece of wood with the exception of C40tip and C50tip, which contained small pieces of wood, and B114tip, which contained two pieces of adjoining wood extracted from the core.							

We extracted and processed all plant macrofossils using standard techniques including pre-washing the fossils in diluted KOH and HCL. Whenever possible, we used single fossils. If we were unable to find single specimens in the depth of interest, we sought fragments in close proximity with one another to minimize uncertainty. For OSL sampling, shielding the specimens from light was not a concern as the previously buried sediments were still encased in light-blocking sample tubes.

We generated two depth-age models to serve different purposes. To assign ages to each core segment, we used a monotonic spline fit to the measured depths and the best-modeled median calibrated ages (Table 4-11), generated with the CLAM model (ver. 2.2 <http://chrono.qub.ac.uk/blaauw/clam.html>) (Blaauw, 2010). The spline fit model

describes local sediment accumulation rates at each depth interval (mm for the Little Lake fit). We also constructed a depth-age model using linear regressions fit to the same data. The regression model better describes sediment accumulation trends and deviations from trends over time. We did not include anomalously old samples in either depth age model, as they reflect either remobilized lakeside sediments or mixing events (Table 4-1).

Table 4-2. OSL data and calculated ages

Age Information						
Sample	USU ID#	Aliquots n	EQ. Dose (De), Gy	Overdispersion %	Dose rate Gy/ka	OSL age ka
B110b	USU-983	27 (55)	63.08 ± 7.92	31.2 ± 4.6	31.2 ± 4.6	31.2 ± 4.6
B136b	USU-974	28 (43)	81.26 ± 7.58	24.3 ± 3.4	2.35 ± 0.19	34.51 ± 4.54
B168c	USU-975a	27 (34)	92.62 ± 6.68	18.0 ± 2.6	2.26 ± 0.24	40.92 ± 5.64
Age analysis using the single-aliquot regenerative-dose procedure of Murray and Wintle (2003) on 2-mm small-aliquots (SA) of quartz sand. Number of aliquots used for age calculation in bold, number of aliquots measured in parentheses. Overdispersion represents scatter in De beyond calculated uncertainties in data, OD >20% is considered significant. Error on age is 2-sigma standard error.						
Dose Rate Information						
	Depth m	H ₂ O ³ %	U ppm	Th ppm	K %	Rb ppm
B110b	33.7	34.7	2.3±0.2	11.7±1.1	1.90±0.05	82.8±3.3
B136b	41.5	29.4	1.7±0.1	9.4±0.9	2.05±0.05	82.8±3.3
B168c	55.9	45.4	3.1±0.2	13.9±1.3	1.69±0.04	90.6±3.6
H ₂ O ³ % refers to <i>in situ</i> moisture content Contribution of cosmic radiation is 0 due to the deep-water setting Grain size for all samples 63-50 µm All samples were processed at the Utah State University Luminesce Lab						

4.5. CRN sample selection and processing

We used our depth-age models and textural grain size determinations to select samples for cosmogenic nuclide analysis. To the extent possible, we extracted sediments at ~1000 to 1500 year intervals. We also focused our sampling efforts at depths with distinct changes in sediment accumulation rates and at the transitions across climate intervals. In all cases, we used amalgamated sediments from the shortest time interval possible (< 1000 years), given minimum mass requirements to extract sufficient quartz grains ranging in size from 0.25-2 mm for cosmogenic nuclide analysis. In all, we processed 25 samples from the paleolake deposit integrating deposits over 700 years or less. We collected modern catchment-averaged sediment samples from two tributary streams above the influence of the paleo-lake (Fig. 4-1B, Table 4-3).

Table 4-3. Cosmogenic nuclide data and calculated erosion rates

Sample	PRIME ID	Qz mass (g)	Be mass (g)	$^{10}\text{Be}/\text{B}_e$ (10^{-15})	Blank* (10^3 at)	$[^{10}\text{Be}]$ (10^3 at g^{-1})	Erosion rate [†] (mm yr^{-1})	Core depth (m)	Age (ky)
LIT I-D	201201530	22.76	284.46	76 ± 5	239 ± 28	43.5 ± 3.6	0.12 ± 0.01	1.15	$\sim 1.5^\ddagger$
LIT I-L	201201865	14.70	265.22	44 ± 7	147 ± 21	43.1 ± 8.6	0.12 ± 0.02	2.17	23.74
A2	201201867	27.75	270.14	64 ± 3	147 ± 21	36.1 ± 2.2	0.14 ± 0.01	2.54	$\sim 6.0^\ddagger$
A4	201201866	24.07	273.24	53 ± 4	147 ± 21	33.9 ± 2.9	0.15 ± 0.01	3.33	$\sim 7.5^\ddagger$
C14b [§]	201201498	5.79	283.71	15 ± 1	239 ± 28	8 ± 6.6	0.64 ± 0.52	4.27	22.6
C20b	201201500	22.41	284.8	44 ± 5	239 ± 28	26.8 ± 4.4	0.19 ± 0.03	6.25	23.33
C23b+c	201201501	16.32	260.0	39 ± 3	239 ± 28	26.6 ± 3.4	0.19 ± 0.03	7.16	23.35
C30b+tip	201201502	30.72	255.2	57 ± 4	239 ± 28	23.9 ± 2.4	0.21 ± 0.02	9.45	23.56
C51b	201201504	17.67	284.89	50 ± 3	239 ± 28	40.1 ± 3.4	0.13 ± 0.01	15.7	23.53
B60c	201201505	13.99	275.27	39 ± 3	239 ± 28	34.3 ± 4.4	0.15 ± 0.02	18.44	23.74
C70b	201201506	17.57	285.10	41 ± 3	239 ± 28	30.9 ± 3.6	0.17 ± 0.02	21.49	24.01
B74c	201201507	15.59	256.13	43 ± 3	239 ± 28	32.0 ± 3.8	0.16 ± 0.02	22.82	24.22
C83a	201201508	14.14	253.89	43 ± 9	239 ± 28	32.0 ± 3.8	0.15 ± 0.05	25.15	25.39
C90tip [§]		9.39	254.32	49 ± 18	239 ± 28	62.5 ± 32.3	0.08 ± 0.04	27.74	25.58
C93c	201201512	16.63	257.3	37 ± 4	239 ± 28	23.9 ± 4.4	0.21 ± 0.04	28.50	25.64
B96d	201201513	18.65	258.9	42 ± 4	239 ± 28	26.2 ± 4.0	0.20 ± 0.03	28.96	25.67
C103a	201201515	12.52	285.6	27 ± 5	239 ± 28	22.1 ± 8.0	0.23 ± 0.08	31.24	26.70
B112	201201870	13.83	272.81	18 ± 3	147 ± 21	14.6 ± 4.2	0.35 ± 0.10	35.21	23.74
B118b+c	201201516	15.46	271.2	32 ± 5	239 ± 28	22.1 ± 6.1	0.22 ± 0.06	37.50	28.48
B122d	201201517	15.33	255.38	46 ± 6	239 ± 28	35.7 ± 6.9	0.14 ± 0.03	39.26	29.36
B124c	201201518	15.75	258.91	46 ± 4	239 ± 28	35.4 ± 4.7	0.14 ± 0.02	39.84	29.64
B128b [§]	201201519	12.73	256.56	37 ± 17	239 ± 28	30.7 ± 17	0.17 ± 0.13	41.17	30.23
B148d	201201522	6.99	253.35	20 ± 2	239 ± 28	14.3 ± 6.2	0.36 ± 0.15	49.06	36.20
B154b	201201523	11.07	262.01	31 ± 4	239 ± 28	27.5 ± 6.8	0.19 ± 0.05	50.70	36.70
B166	201201524	15.82	284.78	36 ± 3	239 ± 28	28.3 ± 4.0	0.18 ± 0.03	54.98	41.47
B176	201201525	15.59	284.57	48 ± 5	239 ± 28	43.3 ± 6.4	0.18 ± 0.03	58.42	44.76
B197	201201526	9.82	259.48	60 ± 14	239 ± 28	81.7 ± 24.9	0.06 ± 0.02	60.43	46.36
Trib 1	201201864	12.85	274.2	63 ± 7	147 ± 21	53.8 ± 7.3	0.10 ± 0.01	n/a	n/a
Trib 2	201201863	20.05	269.2	68 ± 8	147 ± 21	78.6 ± 10.1	0.07 ± 0.01	n/a	n/a

*The ^{10}Be samples reported here suffered from an unusually high blank because of contamination in the chemistry lab. Although the level of contamination was high, it was highly reproducible. The core samples reported here were bracketed by four different blanks, two of which were analysed twice. The tributary samples were run separately and were bracketed by two different blanks. We corrected the concentrations of ^{10}Be for the contamination by subtracting a fixed number of ^{10}Be atoms regardless of sample mass. The laboratory contamination has since been corrected.

[†]Uncertainties in erosion rate reflect errors in AMS measurements of samples and blanks and do not include uncertainties in production rates.

[‡]Estimated sample depth based on position above Mt. Mazama tephra (~ 7.6 ka).

[§]Reported but unused due to low nuclide concentration combined with high uncertainty.

Bedrock density for all samples is 2.0 g cm^{-3} .

All CRN samples were processed using standard techniques at the Purdue Rare Isotope Measurement (PRIME) Laboratory. After sieving sediments, we separated quartz from the samples and isolated ^{10}Be following procedures modified from Kohl and Nishiizumi, (1992). All samples went through a series of physical preparation steps of the quartz including leaching, frothing, magnetic separation and quartz purification to eliminate other minerals and any meteoric ^{10}Be . After physical separation, the samples underwent chemical preparation of the quartz to isolate the ^{10}Be isotopes. Post-purification the Be hydroxide was dried and converted to oxide. We then crushed the oxides and mixed them with niobium powder loaded into stainless steel holders for analysis by accelerator mass spectrometry (AMS). For more details on the methods, see (<http://science.purdue.edu/primelab/user-information/quality-control.php>). AMS measurements were made at PRIME Lab against standards prepared by K. Nishiizumi (Nishiizumi et al., 2007).

4.5.1. Erosion rate calculations

We determined apparent erosion rates using a spatially averaged ^{10}Be production rate weighted by basin hypsometry. As topographic analysis of our data and sedimentological evidence in the core support a deepwater setting (Fig.4-1), which would rapidly attenuate post-secondary cosmic rays, we have not corrected for nuclide production during or after sediment deposition. Using the CRONUS calculator (<http://hess.ess.washington.edu/>) (Balco et al., 2008), we calculated production rates by nucleon spallation. All core samples have a spallogenic production rate of $5.92 \text{ at g}^{-1} \text{ yr}^{-1}$; Trib 1 and Trib 2 (our stream samples) have spallogenic production rates of 6.42 and 6.69 $\text{at g}^{-1} \text{ yr}^{-1}$, respectively. We estimated production due to muons following previous work using revised muon production cross sections (Granger and Muzikar, 2001). Erosion rates are sufficiently fast that we ignored radioactive decay. We also ignored quartz enrichment due to chemical erosion, which we expect to be similar across all samples. Alternative production estimates that incorporate older muon production in samples with high erosion rates, such as the CRONUS calculator, generate erosion rates that are $\sim 25\%$ greater than the method we used. When calculating the mean we used a weighted averaging approach for the samples and the associated error.

It is important to note that cosmogenic nuclide analysis determination requires subtraction of a process blank to account for the small amount of ^{10}Be introduced in the laboratory. At the time our samples were processed there was an unusually high process blank due to contaminated reagents in the chemistry lab. Although the blank was high, it was reproducible for all samples processed at this time, and so we can confidently subtract the blank value from our measurements. This subtraction, together with the low ^{10}Be concentrations in the samples, has led to unusually high uncertainties for some of our erosion rates (10-30%) (Table 4-3).

5. THEORETICAL FRAMEWORK - MEASURED VS. ACTUAL ^{10}Be -DERIVED EROSION RATES

5.1. Cosmogenic nuclides and steady state

Terrestrial *in situ* cosmogenic nuclides such as ^{10}Be , ^{26}Al , and ^3He are standard tools for dating rock surfaces and calculating soil production and erosion rates. As cosmic rays bombard Earth's surface, these nuclides collide with the nuclei of certain minerals to produce rare isotopes. When bedrock is exhumed and exposed to cosmic ray penetration, minerals such as quartz begin to accumulate nuclides at a rate controlled by the location's latitude and elevation. The slower a site erodes the more nuclides it will accumulate (Granger and Riebe, 2014; Lal, 1991; von Blanckenburg, 2005). The accumulation rate depends on depth beneath the surface, as the secondary cosmic rays attenuate exponentially by mass, with an effective attenuation length (L) equivalent to the depth required to traverse $\sim 160 \text{ g cm}^{-2}$. For rock with a density of 2 g cm^{-3} , such as the bedrock at our study site, this corresponds to a depth of 80 cm.

Erosion rates derived from CRN, such as ^{10}Be , are relatively insensitive to anthropogenic effects on erosion in the recently settled Western US, as well as short-term (<1000yr) climate fluctuations as observed in the Little Lake pollen data (Grigg and Whitlock, 1998; Grigg et al., 2001; von Blanckenburg, 2005; Worona and Whitlock, 1995). In moderate eroding sites like the Oregon Coast Range, ^{10}Be concentrations integrate erosion rates over millennial time scales. Specifically, with an attenuation length of 80 cm and an erosion rate of 0.1 mm yr^{-1} , ^{10}Be integrates erosion rates over a timescale of 8,000 years, exponentially weighted towards the present (Lal, 1991).

Because cosmogenic-derived erosion rates integrate information over thousands of years, the steady state assumption overestimates true erosion rates when erosion rates are slowing over time, and underestimates true erosion rates when erosion rates are increasing (Granger and Riebe, 2014; Lal, 1991; von Blanckenburg, 2005). Not only can measured erosion rates deviate from actual erosion rates due to changing soil production rates, but vertical soil mixing (due to processes ranging from root disturbance to frost heave to earthworm activity) can also differentiate CRN inventories in soil and the underlying bedrock and change rapidly in a soil column when mixing depth changes (Fig.4-2).

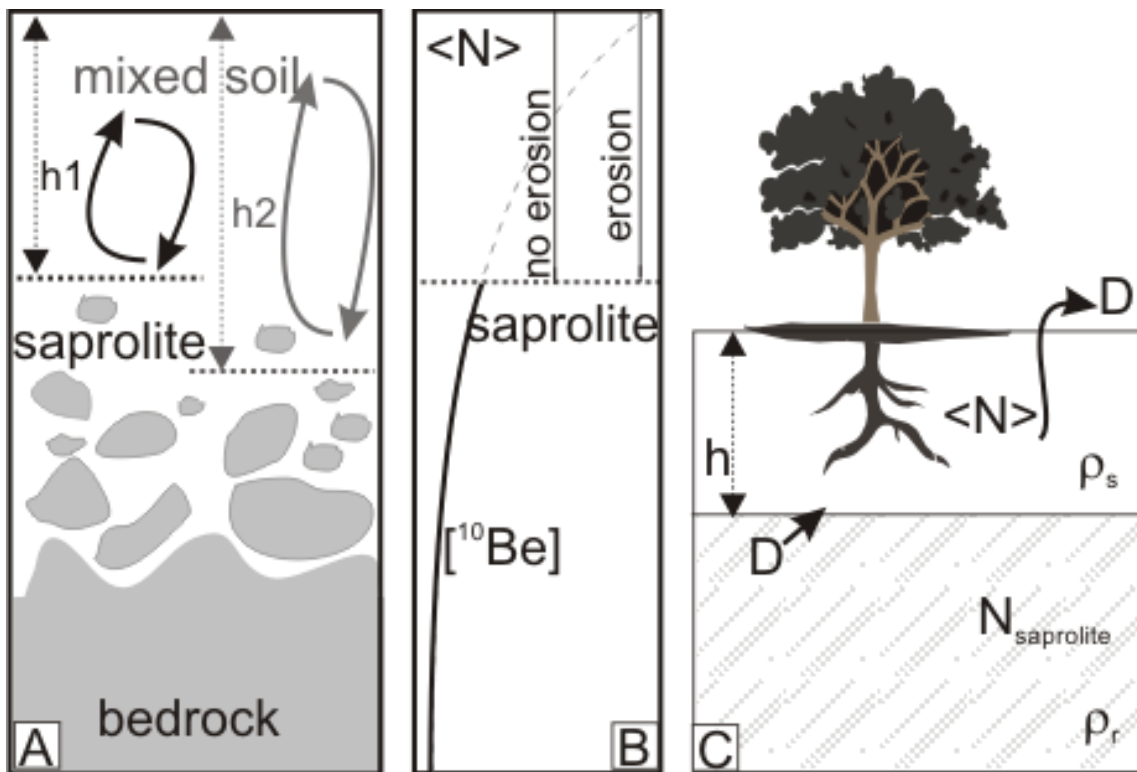


Fig. 4-2. Models of cosmogenic nuclide accumulation and loss in vertically well-mixed soils A) Model illustrating how increasing the mixing depth incorporates saprolite with lower nuclide concentrations into the soil nuclide inventory. B) Model predictions of ^{10}Be concentration in well-mixed soil with and without erosion. Bold lines represent actual concentrations and dashed line represents the concentration in an unmixed soil. C) Conceptual model illustrating cosmogenic nuclide accumulation and loss in a well-mixed soil (Equation 4-4). Figures A and B modified from Granger et al. (2014).

5.2. Soil production

By constraining how erosion rates or mixing depths change CRN concentrations and thus measured erosion rates, we can begin to develop insight into the processes

controlling soil production and erosion rates through time. For example if we can constrain the mixing depth to shallow depths (e.g., < 30 cm) then it is unlikely that tree roots were the soil production mechanism. If mixing depths are shallow and erosion rates are fast, then frost weathering, heave and solifluction would be reasonable soil production and erosion mechanisms. Alternatively, if mixing depths are shallow and erosion rates are slow, than consideration of other mechanisms such as ant or worm activity may be warranted.

Under steady state conditions, the soil production rate (P) ($L T^{-1}$) equals the erosion rate (E) ($L T^{-1}$), such that changes in the bedrock surface elevation over time can be described by:

$$E = P = P_0 e^{-\alpha h} \quad (4-1)$$

where P_0 ($L T^{-1}$) is the maximum soil production rate, α (L^{-1}) is an empirical decline constant and h (L^{-1}) is soil depth normal to the ground surface (Heimsath et al., 1997). The exponential soil production hypothesis states that erosion rates should be at a maximum on bare rock and decline exponentially with increasing soil thickness or bedrock depth (e.g., Dietrich et al., 1995; Heimsath et al., 1997).

We can rearrange equation 4-1 such that erosion and the maximum soil production rate are a function of depth:

$$h = \frac{-\ln(E / P_0)}{\alpha} \quad (4-2)$$

Local stochastic changes in soil depth (e.g., induced by bioturbation) equilibrate rapidly, such that we can assume in this steady state formulation that local soil depth does not vary with time (Dietrich et al., 1995; Heimsath et al., 1999).

Alternative formulations such as ‘humped’ soil production functions posit that soil production is maximized at shallow depths, rather than at the surface, where the soil is thick enough to hold water and foster physical weathering agents such as plants and frost (Cox, 1980; Gilbert, 1877). There may be mechanistic reasons for multiple functional shapes (Cox, 1980; Furbish and Fagherazzi, 2001; Gabet and Mudd, 2010). For our purposes, we rely on the exponential soil production as it the most parsimonious and is well-established (e.g., Granger and Riebe, 2014; Heimsath et al., 1997; Humphreys and Wilkinson, 2007; Wilkinson and Humphreys, 2005).

5.3. Cosmogenic nuclides for transient erosion and soil production

When deriving erosion rates from CRNs, it is standard practice to model erosion rates as steady state, even in transient landscapes (Granger and Riebe, 2014; Heimsath, 2006; Wilkinson and Humphreys, 2005). Under steady erosion, when erosion rates are faster than $\sim 0.1 \text{ mm yr}^{-1}$ we can ignore radioactive decay and calculate CRN concentrations at the surface (assuming no mixing) as:

$$N_0 = \sum P_i L / D \quad (4-3)$$

where P_i is the nuclide production rate by nucleon spallation ($\text{atoms M}^{-1} \text{T}^{-1}$), L is the attenuation length (M L^{-2}) and D is the denudation rate ($\text{M L}^{-2} \text{T}^{-1}$) (Granger and Riebe, 2014).

However, most soils undergo some form of mixing, with the depth and vigor dependent on the mixing mechanism (e.g., tree throw vs. burrowing vs. frost heave) or ecosystem type (e.g., grassland vs. forest). Additionally, we have an expectation that with climate changes, soil production processes should also change along with mixing depth. One can imagine a scenario where a temperate conifer forest with average root-driven mixing depths of $\sim 1 \text{ m}$ transitions to a grassland as temperature cool and precipitation decreases. In this scenario, the new climate supports different biota and shallow ($\sim 0.5 \text{ m}$) gopher activity rather than trees that may control soil production. At a more nuanced level, rooting mass, rooting depth, and below ground net primary productivity (related to process efficiency for mixing and transporting soils (e.g., Phillips, 2009; Yoo et al., 2005)) can vary among different biomes and forest types (Canadell et al., 1996; Hudiburg et al., 2009; Jackson et al., 1996; Runyon et al., 1994), such that the vigor and depth of soil production and mixing may be related to differences in forest composition. Thus, both changing erosion and soil mixing depths reflect the new geomorphic regime imposed by climate change. These mechanisms are likely key to soil production and control erosion rates.

With these types of climate-driven scenarios in mind we can apply an analytical solution developed to calculate denudation rates in vertically mixed soils (Granger and Riebe, 2014) to calculate not just erosion rates, but soil production rates and mixing depths by incorporating the exponential production function (Equations 1,2). When combined with information such as the climate-specific processes disrupting bedrock and

churning the soil, this framework provides insight into the mechanics of soil production, erosion rates and thus landscape evolution. For more details on the cosmogenic transient erosion model with soil mixing, we refer the reader to Granger and Riebe (2014), Section 7.12.3.3.

Consider a vertically mixed soil, where the soil contains the vertically-averaged CRN concentration (Fig. 4-2B). The mixed layer has a steady thickness, and material lost from the soil due to erosion at a mass rate of D_{soil} is replaced by soil production from below at the same mass rate (Fig. 4-2C). This supply is the equivalent to the soil production rate described by Heimsath et al., (1997) (Granger and Riebe, 2014). Following Granger and Riebe (2014) and Heimsath (2006) in assuming no radioactive decay and that the soil production rate equals the total denudation rate (i.e. $D_{soil} = D = P$) we can conceptualize the spatially averaged nuclide concentrations over time in vertically mixed soils using the following equation:

$$\frac{d\langle N \rangle}{dt} = \langle P_i \rangle - \frac{\langle N \rangle P}{\rho_s h} + \frac{N_{sapolite} D}{\rho_s h} \quad (4-4)$$

where $\langle \rangle$ denotes depth-averaged in the homogenous, well-mixed soil, N is the nuclide concentration (atoms $M^{-1}T^{-1}$), P_i is the surface nuclide production rate (atoms $M^{-1}T^{-1}$), ρ_s is the soil density ($M L^{-3}$) and h is soil depth. Essentially, the rate of nuclide concentration change depends on the nuclide production in the soil (term 1), the loss due to erosion (term 2) and input from bedrock or saprolite below (term 3).

By incorporating the formulation for each of the terms, we can rewrite equation 4-4 as:

$$\frac{d\langle N \rangle}{dt} = \frac{P_i L}{\rho_s h} \left(1 - e^{-\rho_s h/L}\right) - \frac{\langle N \rangle D}{\rho_s h} + \frac{P_i L}{\rho_s h} e^{-\rho_s h/L} \quad (4-5)$$

where L is the nuclide penetration length ($M L^{-2}$). For steady state conditions, we arrive again at the familiar and oft-used solution described previously:

$$\langle N \rangle = \frac{P_i L}{D} \quad (4-6)$$

Importantly, note that the steady solution does not depend on the mixing depth. By contrast, the transient solution (equation 4-5) includes soil depth, providing us with an opportunity to link this analysis with the depth-dependent expression for soil production

(equation 1) or inversely explore how changing erosion rates and soil production control soil thickness.

Simplifying Equation 4-5 we arrive at:

$$\frac{d\langle N \rangle}{dt} = \frac{1}{\rho_s h} (P_i L - \langle N \rangle D(t)) \quad (4-7)$$

Equation 4-7 indicates that as soil depth increases due to imposed changes in mixing depth, the rate of change of nuclide concentrations in the soil decreases and thus it takes longer for nuclide concentrations to equilibrate. The lag time between actual and transient nuclide-derived erosion rates is to be expected, due to integration time of the nuclide concentration, as demonstrated in a plethora of previous models (Heimsath, 2006; Lal, 1991; Schaller and Ehlers, 2006; von Blanckenburg, 2005). However, due consideration has not been given to the importance of considering mixing depths in a turbated soil column. To illustrate how CRN-derived (measured) erosion rates deviate from actual transient erosion rates in a well-mixed soil we apply the transient solution to varying erosion rates and mixing depths over 20 ky time steps for 120 ky. We model the actual and measured erosion rates for mixing depths of 20 mm and 60 mm. For the first 60 ky, actual erosion rates vary by a factor of 3, fluctuating between 0.03 mm yr^{-1} and 0.1 mm yr^{-1} . Starting at 60 ka, the actual erosion rates fluctuate by a factor of 1.5, varying between 0.15 mm yr^{-1} and 0.1 mm yr^{-1} (Fig. 4-3). The greater the increase in erosion rates, the faster the vertically mixed soil transmits this change if the mixing depths are low. A 3x increase in true erosion rates takes $\sim 15 \text{ ky}$ to for the soil to integrate the perturbation with a mixing depth of 20 mm and is still approaching equilibrium after 20 ky when the mixing depth is 60 mm. In contrast, a 1.5x increase in erosion rates begins to approach the actual erosion rate after 20 ky, but the relatively small difference between the new erosion rate and the CRN inventory results in a delayed response to the perturbation. The relatively modest mixing depth of 60 mm imposes a significant additional length of time before the nuclide concentration equilibrates under transient conditions.

This theoretical framework is important to consider when evaluating measured erosion rates under transient erosion and perhaps variable mixing depth conditions. In the

following sections, we discuss results from the Little Lake paleo-archive, including measured and possible actual erosion rates.

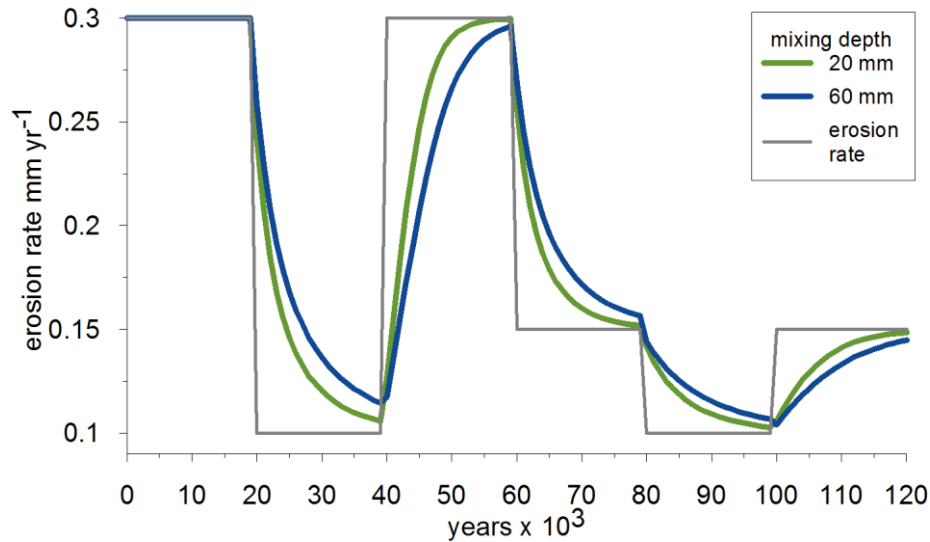


Fig. 4-3. Model applying the transient solution for nuclide-derived erosion rates with fluctuating erosion rates and two different mixing depths. Gray line delineates the actual erosion rates through time. The greater the mixing depth the longer it takes for measured erosion rates to equilibrate to actual erosion rates.

6. RESULTS

We utilized the core to generate descriptive information about the sediment character through time, extract plant macrofossils and sediments to date the core. With the dated material, we generated a depth-age model to evaluate sediment accumulation rates through time and guide CRN sample selection. To put the data compilation in context, we first describe our visual observations of core data, before presenting ¹⁴C and OSL, fossil identification, and cosmogenic nuclide results. Given that we are interested in the expression of climate change through time, our core descriptions follow chronological order. In Fig. 4-4, we provide a summary of the NOB core data, including plant macro fossil ages for depth intervals in the core, fossil occurrences of note, grain size data, ¹⁰Be-derived erosion rate data, and data relationship to other relevant Little Lake studies.

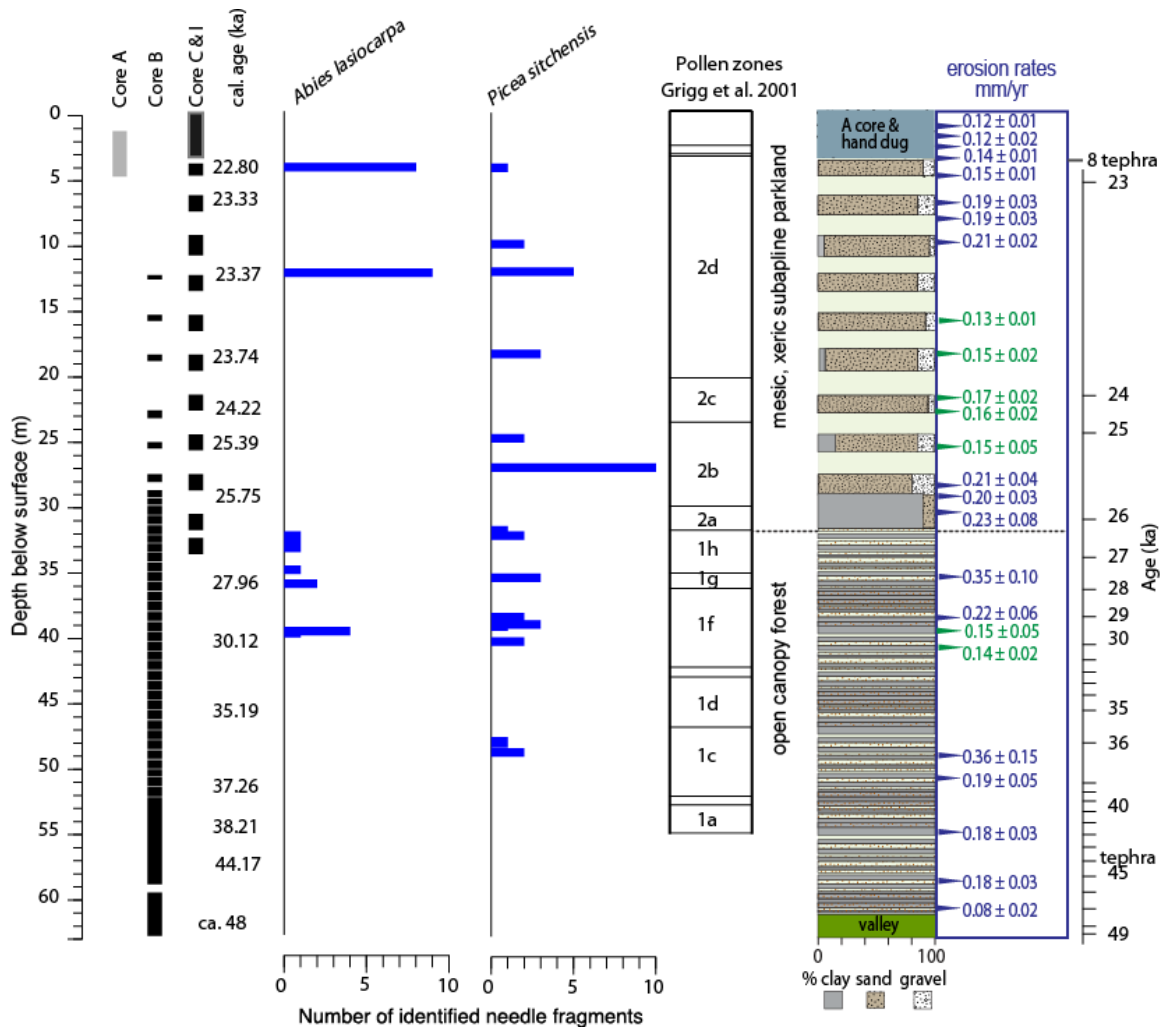


Fig. 4-4. Compilation of Little Lake core observations and data. NOB core sample interval depths described by rectangles on left side of plot. NOB A (gray rectangle, left side of figure) core data lack precise depth control due to gaps in the collection tubes. *Picea sitchensis* (Sitka spruce) and *Abies lasiocarpa* (subalpine fir) co-occurrence observed at 29.5 to 22.6 ka based on depth-age model. Pollen zones of Grigg et al. (2001) and general descriptions of ecosystem types during MIS 3 (LL-1) and MIS 2 (LL-2). Percent clay, sand and silt in the core based on visual observations. Solid tan regions within core stratigraphy column represent intervals without data (replicating gaps in the core described on the left-most side of the figure). The entire core sequence consists of mm-cm scale laminated lacustrine deposits, with a significant reduction in fine-scale laminations, increase in grain size and an increase in sediment accumulation rates at ~ 26 ka, coincident with the start of (MIS 2) interval. ^{10}Be -derived erosion rates values in green have high concentrations ^{10}Be concentrations and are discussed in section 7.2.

6.1. Core observations and assessment

The entire Nob B and C core sequence is lacustrine, with laminated, predominately clay and sand deposits throughout. The most striking observation along the length of the core is the profound shift in sediment size, color, and lamination spacing at ~ 31 m depth (Fig. 4-4). Below 31 m, the core deposits are generally characterized by finely laminated, mixed clay to sand size sediments, varying in color from brown to grey to red. At 31 m, the lake deposits abruptly change to predominantly cm-scale laminations and blue-grey, coarse, uniform, angular sand deposits. The striking angular blue-grey deposits persist in the core up to ~ 4 m depth.

Throughout the core we observed vivianite, a phosphate mineral formed under reducing redox conditions (Rosenqvist, 1970) and commonly found in lacustrine deposits. The deposits fluctuate from grey to brown to red, with laminations and/or thin (mm-cm scale) lenses of different colors and/or grain sizes within thicker sequences. Infrequently (< 5%) we observed mottling over intervals of < 15 cm. Gravels, while interspersed throughout the core, never dominate any of the grain size percentages. Intermittently throughout the core, we observe likely debris flow deposits, marked by woody debris and angular clasts.

The very lowest segment of the B core (61.6 m-62.1 m below the surface) contains large, angular, gleyed, deeply weathered clasts, large pieces of wood jumbled with coarse, poorly sorted sands and clays, which we interpret as a deep-seated landslide deposit. This particular deposit type is unique within our core samples. The landslide deposit overlies a paleo-soil comprised of clay with fine sand, wood and charcoal fragments throughout and a well-preserved core-spanning fragment of western Hemlock at 63.20 m. Below the paleo-soils and forest wood at (the original valley bottom) our final samples (63.35 m - 63.65 m) are intact, competent sandstone, which comes from the bedrock of the paleo-valley floor (Eocene Tye Formation).

We observed tephra deposits at two depths in the cores. Firstly, we found water-lain ash (57 m) below pockets of ash (56.5 m), which we interpret as aerial deposition followed by subsequent transport of hillslope-transported ashfall to the lake. Given that our depth-age curve suggests that the water-lain tephra deposit dates to 43.5 ka, and based on the tephra's distinct 'salt and pepper' appearance, the deposit is likely the Mt.

St. Helens tephra set Cy (Ape-Canyon Stage deposits). This initial eruptive stage spans 275 to 35 ka. It is divided into two distinct periods, 275 to 250 ka and 160 – 35 ka, with the C interval dated to ~50- 35 ka (Clyne et al., 2008; Crandell, 1987; Kuehn and Negrini, 2010). Secondly, we observe tephra in both the NOB A and NOB-I cores, our two near-surface sample sets. We have excellent depth control on the hand-dug NOB-I samples, where we found a 1cm thick ash within lake sediments at 2.93 m below the surface. While we have only crude depth control on our NOB A cores, as the paired 2.5ft (0.76 m) drives (for a total of 5 ft or 1.52 m) were only partially filled with sediment, we did observe a sharp transition to ash in the A4 tube , at ~ 4.1 m with the upper A3 tube bereft of lake deposits. Based on our NOB A core observations, we expect that the deposit was originally emplaced in the A3 tube, which would place the ash at a similar depth below the surface as our hand-dug NOB-I core. Given the extensive Mt. Mazama tephra deposits in the region, and more importantly the recovery of a ~ 1cm layer of Mt. Mazama tephra deposits from the previous Little Lake core (Worona and Whitlock, 1995), we interpret these near-surface tephra deposits as Mt Mazama (~ 7.7 ka) origin. This is important as it provides us with age control for the near-surface portions of the core drives.

6.2. Chronology and depth-age model

We generated ages for intervals in the core from plant macrofossils (radiocarbon) and sediments (OSL) (Tables 4-1, 4-2). The sediments preserve a high-fidelity record of past environments from 4 m below the surface to the original valley bottom. However the radiocarbon dates lead us to infer that the paleolake location had changed from a depositional setting to intermittently erosional by ~20 ka. NOB I-P, at 3.22 m is only 0.29 m below NOB I-O, which contains the 7.7 ka Mt. Mazama ash deposit, and yet dates to 21.6 ka (Fig. 4-4, Table 4-1). We can use our near-surface ^{14}C dates to constrain the age of cosmogenic samples, as near-surface samples immediately adjacent to the ^{14}C dates are deemed reliable, even though a depth-age model is not possible. In Figure 4-5, we plot sample depth (below the surface) against years before present from 21.6 ka to 48.4 ka. Open triangles represent age dates that we did not include in the depth age model, as they are anomalously old compared to neighboring samples and likely reflect re-worked sediment. Because the age-depth data has an obvious inflection between 36 m (28 ka) and

41 m (30 ka), we plot two separate linear regressions to estimate average sediment accumulation rates. Based on linear fits, pre-27 ka sediment accumulation rates averaged $1 \pm 0.003 \text{ mm yr}^{-1}$, and post-27 ka accumulation rates averaged $6 \pm 0.085 \text{ mm yr}^{-1}$. Particularly notable is the $> 16.5 \text{ m}$ of sediment dated between 24 ka and 23 ka. While the three OSL samples have large errors, the dates are well-fit with the ^{14}C dates, and thus we include them in the model (Fig. 4-5).

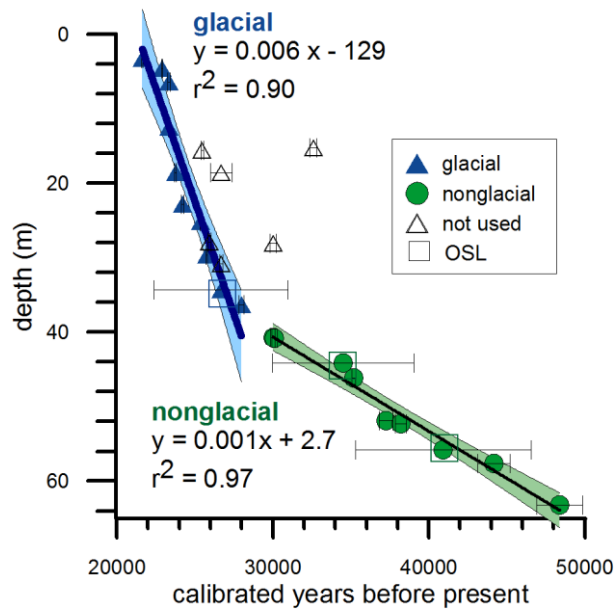


Fig. 4-5. Depth-age model based on ^{14}C and OSL dates. Linear fits describe the trends in sediment accumulation rates over time. Open triangles mark fossils with dates chronologically older than underlying fossils.

6.3. Fossil identification

We refine previous Little Lake paleo-environmental reconstructions (Grigg et al., 2001; Worona and Whitlock, 1995) with the observation of the co-occurrence of Sitka spruce and subalpine fir from $\sim 29.5 \text{ ka}$ through 22.6 ka based on needle counts (Fig. 4-4). These two species are rarely found together today with the exception of cold parkland settings in SE Alaska (latitude 55.6°N) (Alexander et al., 1990). As Worona and Whitlock (1995) and Grigg et al. (2001) noted, while their extensive pollen-based paleo-environmental reconstruction suggests a sub-alpine parkland setting toward the end of MIS 3 and into the glacial MIS 2, they were unable to resolve *Picea* pollen to the species

level. This lack of resolution was problematic for climatic reconstructions as the fossil pollen assemblages suggested a vegetation ecosystem with no modern analogue. The presence of Engelmann spruce (*Picea engelmannii*) in the core would suggest an analogue setting such as the Cascades or maritime Olympic Peninsula (48°N) whilst the presence of Sitka Spruce would imply much a setting akin to SE AK (56°N). With our identification of the co-occurrence of Sitka spruce and subalpine fir from the end of MIS 3 through MIS 2, we can now better constrain the late Pleistocene climate with the modern analogue, a geographically restricted region near Hyder, AK (Alexander et al., 1990). Additionally, of note, we find the pollen evidence of lacustrine species *Nuphar* and *Potamogeton* throughout the core (D.G. Gavin, personal communication) which confirms sedimentological evidence of a deepwater setting, eliminating the need to consider nuclide inheritance as water would have rapidly attenuated the cosmic ray flux.

6.4. ¹⁰Be-derived erosion rates

We analyzed nuclide concentrations from 26 paleolake samples and two modern samples collected from stream sediments above the paleolake influence (Fig. 4-1B). In calculating nuclide-derived erosion rates, we use the steady state formulation (equation 4-3). Thus, unless nuclide concentrations have had sufficient time to equilibrate we assume the measured erosion rates are underestimates as erosion rates increase and overestimates as they decrease (Fig. 4-3). Using our CLAM depth-age model fit to assign ages to the CRN samples, we plot ¹⁰Be-derived erosion rates against years before present (Fig. 4-6). We include samples with very high errors (Table 4-3), although we ignore these samples in our evaluation of the results.

¹⁰Be-derived (apparent) erosion rates from the oldest part of our core at 46.4 ka are 0.06 mm yr⁻¹ and generally increase throughout MIS 3, concurrent with decreasing temperatures (Grigg et al., 2001; Worona and Whitlock, 1995) and a shift in ecosystems from temperate and montane forests to a subalpine parkland. The erosion rate increase during MIS 3 occurs before the increase in sediment accumulation rates at MIS 2 (Fig. 4-5). At 28.5 ka, coincident with a break in slope in our depth-age model (Fig. 4-5), apparent erosion rates are 0.23 mm yr⁻¹, 3.8x greater than our oldest measured erosion rate. Throughout MIS 2 erosion rates fluctuate around 0.21 ± 0.01 (mean and se) mm yr⁻¹ (n=7), a value that is 3.2x greater than our 46.4 ka sample. Two clusters of samples at ~

29 ka and ~ 23-25 ka have anomalously high ^{10}Be concentrations (and thus low apparent erosion rates). We ignore these samples as they occur in the same period as age-reversed fossils (Section 6.2) and within the cosmogenic nuclide framework of an actively eroding landscape ‘impossibly’ integrate a rapid increase in nuclide concentrations over a short time span (Fig.4-3). We discuss this in more detail in Section 7.2. We include an apparent erosion rate at 23.7 ka of 0.35 ± 0.1 mm in our mean glacial interval value of 0.21 ± 0.01 yr^{-1} , as we calculated the mean using an inverse variance (Bevington and Robinson, 2003). We also note that the increase in erosion rates during MIS 3 precedes an increase in sediment accumulation rates during MIS 2 (Fig. 4-5).

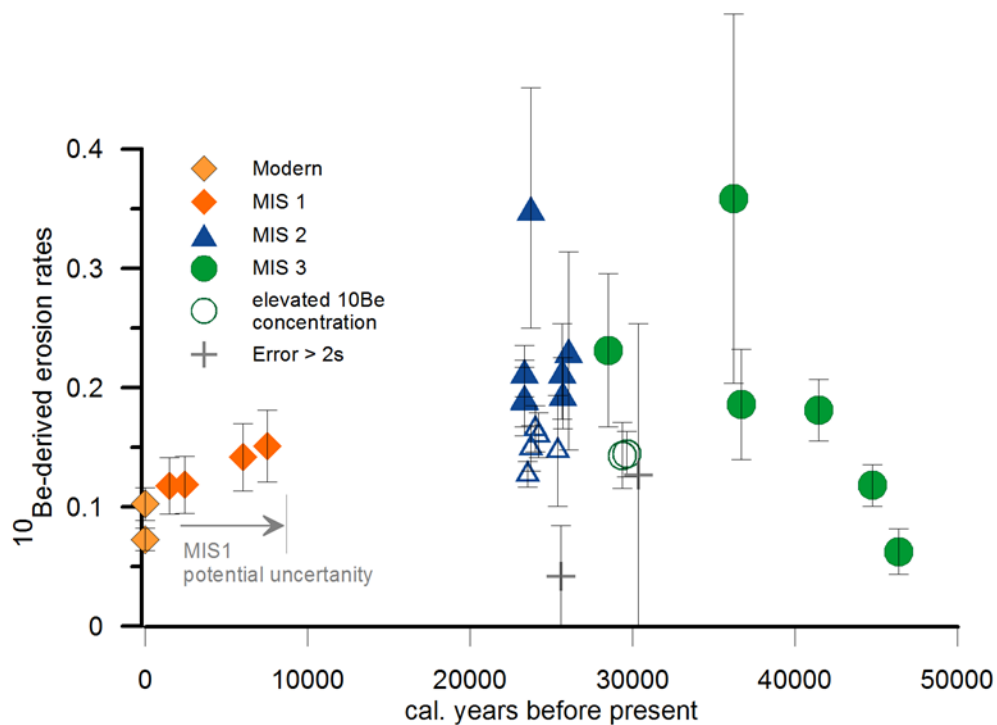


Fig. 4-6. Little Lake ^{10}Be -derived erosion rates vs. time. All MIS 1 samples are from lake sediments deposited above Mt. Mazama tephra. As ages are unconstrained above the Mt. Mazama tephra (~7.6 ka) due to core incompleteness and inferred erosional episodes, we assign approximate ages to the MIS 1 samples based on core chronology. Modern samples collected from tributary sediments above the lake influence.

Due to core incompleteness, we have no data for the late glacial to early Holocene transition (the period between ~22.6 and 8 ka). Samples from NOB A2 and A4 core have only coarse age constrain. The NOB A4 sample comes from just above the Mt. Mazama tephra deposit, so we assign an age of 7.5 ka to the sample (Fig. 4-4). For sample A2, we

estimate an age, acknowledging that it could be much younger. While we have a radiocarbon date of $2,427 \pm 25$ years for LIT I-L (2.17 m), in LIT I-D (1.15 m), ~ 1 m above LIT I-L, fossils were indistinguishable from modern surface plants with deep roots penetrating the paleo deposits, so we chose not to date the material. However, given that the LIT core data comes from an active deposition area near the modern Little Lake (Fig. 4-1), we are confident that the sample pre-dates modern deposits and thus we assign an age of 1500 years to the sample for plotting purposes.

During the late Holocene, the measured erosion rates for samples with ‘assigned’ ages decrease in chronological order, with our sample from just above the 7.6 ka Mt. Mazama ash recording an erosion rate of 0.15 ± 0.01 mm yr⁻¹. Values continue to decline, with modern erosion rates averaging 0.08 ± 0.01 mm yr⁻¹.

7. DISCUSSION

7.1. Climate-mediated changes in soil production mechanisms

. Erosion rates at Little Lake track climate change through time, with a 3.2x increase in measured erosion rates concurrent with declining temperatures, as climate transitioned from the pre-LGM MIS 3 into the full glacial MIS 2. Measured LGM erosion rates are 2.5x higher than modern erosion rates (Figs. 4-4, 4-6, Table 4-3). Despite gaps in our core data at the Pleistocene-Holocene transition and through the early Holocene, erosion rates declined with the warming transition from a subalpine setting (Grigg et al., 2001; Worona and Whitlock, 1995, Chapter III) to the modern temperate climate. Importantly, paleoclimate reconstructions from the Little Lake Basin as well as sedimentological observations allow us to infer the mechanistic underpinnings controlling measured erosion rate changes.

Below we first lay out evidence for the transition from a forest-driven sediment production and transport regime to an increasingly cold and frost-dominated sediment production and transport regime before transitioning back to a forested setting in the Holocene. By combining lidar observations with fossil and ¹⁰Be data, a more nuanced lake history emerges, providing context for our sedimentation and erosion rate plots, which we discuss before returning anew to the theoretical framework underlying measured vs. actual erosion rates in a setting such as Little Lake. This theoretical

framework allows us to consider lag times between climate-mediated changes in soil production mechanisms and mixing depths and implications for landscape evolution. Additionally, our sediment accumulation (Fig. 4-5) and erosion (Fig. 4-6) rate data allows for consideration of the timing of soil production vs. transport and deposition signals.

7.1.1. Forests, frost and soil production rates

Given the presence of tree species indicative of periglacial settings (Grigg et al., 2001; Worona and Whitlock, 1995), a profound shift in sediment character, an increase in grain size, angularity and lamination spacing (Fig. 4-4), a 6x increase in sediment accumulation rates (Fig. 4-5) and a 3x increase in erosion rates as climate cooled during MIS 3 (50-26 ka), with MIS 2 glacial interval erosion rates 2.5x greater than modern (26-22.6 ka recorded in the core) (Fig.4-6), we hypothesize that frost processes increasingly dominated soil production, transport and erosion during the late stages of MIS 3 and throughout the glacial interval. Not only did climate dictate the transition between biotic and abiotic controls on sediment production and erosion mechanisms, but our erosion rate data also suggests that frost processes are significantly more efficient erosion mechanisms than tree-driven processes.

Bedrock disruption and damage via tree roots range from cantilever-like leverage exerted by large-diameter trees during windstorms to simple displacement via lift forces generated by roots extending along horizontal bedding planes (Marshall and Roering, 2014). Roering et al. (2010) analyzed the role of trees in bedrock to soil production in the thin-soiled forested OCR and found strikingly similar patterns between ¹⁰Be-derived soil production rates (Heimsath et al., 2001) tree size, volume of bedrock in overturned tree roots, and the measured depth distribution of conifer tree roots. In addition to priming bedrock for detachment and generating soil, trees transport soil downslope when uprooted (Gabet and Mudd, 2010; Gabet et al., 2003; Heimsath et al., 1999; Lutz, 1960).

Frost processes are also extremely efficient at bedrock damage, disruption, and transport. Frost damage, from micro- to macro-cracks (Murton 2006) occurs via segregation ice growth (frost cracking or weathering), while disruption and transport occurs via frost heave, frost creep and solifluction. Bedrock fracturing occurs when ice lenses grow in rock pore spaces at temperatures between approximately 3°C to -8°C (Anderson, 1998; Hales and Roering, 2007; Walder and Hallet, 1985). Rock damage

created by the growth of segregated ice lenses is vigorous at these temperatures; at warmer temperatures, ice lens pressure is too low, while at colder temperatures, high viscosity limits water migration rates towards the ice lenses. Unlike freeze-thaw processes, which depend on frequency of temperature fluctuations, frost weathering depends the steepness of the temperature gradient (Hales and Roering, 2007) below the surface when in the frost cracking window.

While frost weathering damages rock, frost heave, active particularly at temperatures of $\sim 0^{\circ}\text{C}$ (Matsuoka, 2001), is extremely efficient at vertically mixing soils (Small et al., 1999). Frost heave, creep, and solifluction are intimately associated with one another. As frost creep disrupts soil particles horizontally (particularly driven by needle ice), they are then displaced downslope (French, 2013; Matsuoka, 2001). Solifluction is the downslope mass movement of frost creep soils. The mechanics and efficiency of frost heave, needle ice creep, frost creep, plug-like flow etc. are dependent on a range of factors including one vs. two-sided freezing, freeze-thaw cycle frequency, moisture availability, and frost susceptibility of the soil (French, 2013; Harris et al., 2008; Matsuoka, 2001; Smith, 1992), beyond the scope of this study. However, we can generalize the information relevant to Little Lake, in that hillslope gradient is a first order control on potential frost or biogenic creep travel distance. Potential frost (and biogenic) creep distance (l) is described by:

$$\Delta l = h \tan \theta \quad (4-8)$$

where h is the heave normal to the ground surface and θ is the hillslope gradient (French, 2013). Because hillslope gradients are steep ($>35^{\circ}$), sediment transport efficiency is quite high in the Little Lake catchment. Frost-driven sediment production and transport in cold climates is substantial (Matsuoka, 2001; Matsuoka and Murton, 2008), with ^{10}Be -derived erosion rates attributed to frost weathering increasing with decreasing temperature (Delunel et al., 2010). Solifluction rates in montane climates are up to 10x faster than soil creep in temperate climates, though the solifluction rates may be biased due to studies focusing on highly active sites (Saunders and Young, 1983). Mean solifluction rates in steep montane topography average $\sim 6 \text{ cm yr}^{-1}$ compared to soil creep rates of $\sim 1 \text{ cm yr}^{-1}$ in temperate settings. In modern settings with steep slopes, seasonal frost and MAT similar to Little Lake's LGM MAT of $\sim 0^{\circ}\text{C}$, solifluction rates approach $\sim 20 \text{ cm yr}^{-1}$

(Matsuoka, 2001). Therefore we expect that frost-driven transport rates at Little Lake exceeded biogenic-driven rates, which may account for the increase in sediment accumulation rates during MIS 2.

7.1.2. Frost weathering model and erosion rates through time

With the evidence of the co-occurrence of Sitka spruce and subalpine fir starting at 29.5 ka at Little Lake (Fig.4-4), which points to a modern analog climate similar to that in southeast Alaska, we can model temperature controls on frost weathering intensity at Little Lake 21 ka, based on paleoclimate simulations for the LGM (See Chapter 3). Additionally we can use vegetation-derived mean annual temperatures (Grigg et al., 2001) during the earlier glacial interval (MIS 3) and a frost weathering model to consider how frost-controlled weathering rates may have changed through time in the Little Lake watershed.

We employ an analytical solution for 1-dimensional heat conduction appropriate for annual temperature variations (Bloomfield, 2000; Carslaw and Jaeger, 1959):

$$T(z,t) = MAT + e^{-z\sqrt{\frac{\pi}{\alpha P_y}}} \left(A_1 \cos\left(\frac{2\pi t}{P_y} - z\sqrt{\frac{\pi}{\alpha P_y}}\right) + B_1 \sin\left(\frac{2\pi t}{P_y} - z\sqrt{\frac{\pi}{\alpha P_y}}\right) \right) + e^{-z\sqrt{\frac{2\pi}{\alpha P_y}}} \left(A_2 \cos\left(\frac{4\pi t}{P_y} - z\sqrt{\frac{2\pi}{\alpha P_y}}\right) + B_2 \cos\left(\frac{4\pi t}{P_y} - z\sqrt{\frac{2\pi}{\alpha P_y}}\right) \right) \quad (4-9)$$

where T is daily temperature, z is depth, t is time, MAT is the mean annual temperature calculated from monthly mean temperatures, α is the thermal diffusion coefficient, P_y is the time period for the curve (we use an annual cycle) and A_1 , B_1 , A_2 , B_2 are coefficients of a Fourier series fit to monthly temperature data extracted from paleoclimate simulations (See Chapter 3).

Our model quantifies the intensity of frost weathering as a simple increasing function of the temperature gradient. We define the frost-weathering index as the annual integral of the depth-integrated daily temperature gradient ($^{\circ}\text{C}\cdot\text{day}$) for substrate within the -3°C and -8°C temperature range. The model calculates daily temperatures at the surface and at depth based on the mean annual temperature (MAT), a thermal diffusion coefficient (α), and the harmonic coefficients. In our model, the half amplitude of seasonal temperature variations and MAT are the dominant factors controlling the vigor of frost weathering at a given location.

Because the co-occurrence of Sitka spruce and subalpine fire at similar elevations is confined to a narrow geographic range in the Hyder AK area (Alexander et al., 1990), we use modern temperature data from a nearby analogue site located at 400 MASL (55.914° N, -130.024°) to constrain the available LGM paleoclimate simulations to the most suitable for Little Lake LGM temperatures (Chapter 3). After downloading and downscaling CMIP5/PMIP3 (Coupled Model Intercomparison Project Phase 5/Palaeoclimate Modelling Intercomparison Project Phase 3) simulations to generate mean monthly temperature data (Braconnot et al., 2012; Harrison et al., 2013; Izumi et al., 2013) we chose the MIROC model as most appropriate for Little Lake (Chapter 3) as it most closely matches conditions at the analogue site. While MAT at modern Little Lake is ~ 11°C, with amplitude of ~ 7°C MAT at Little Lake 21 ka was ~0°C with an amplitude of ~ 8°C (Fig. 4-7). Differences in summer insolation and the degree of ocean and land surface interactions resulted in greater interannual temperature variation during the Pleistocene (French, 2013) which accounts for the increasing amplitude during the LGM.

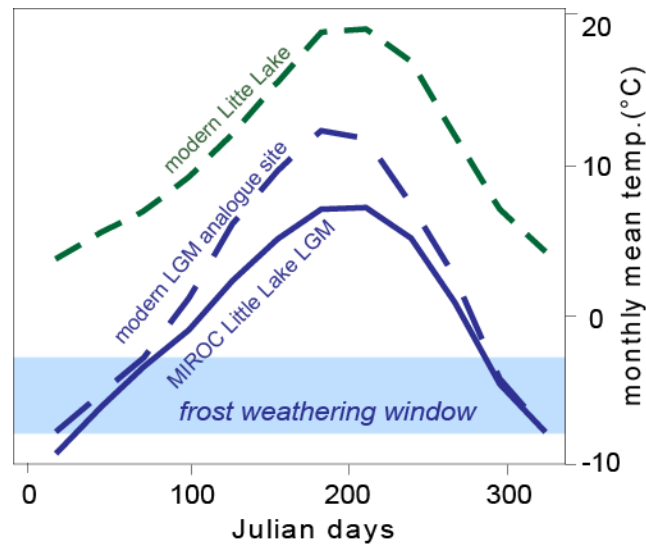


Fig. 4-7. Comparison of annual temperature curves based on: mean monthly temperature data for modern Little Lake, a representative location near Hyder AK (our analogue site), and downscaled paleoclimate simulation data from MIROC-ESM.

According to our model, the amplitude of seasonal temperature variation and *MAT* are the dominant factors controlling the vigor of frost weathering at a given site.

Thus, we can use a contour plot of frost weathering intensity as a function of amplitude and MAT to predict how frost weathering intensity and thus erosion rates might have increased through time at Little Lake. Not surprisingly, our model predicts no modern frost weathering at Little Lake. Using temperature output from our downscaled paleoclimate data, Little Lake was in the frost weathering zone 21 ka (Fig. 4-8).

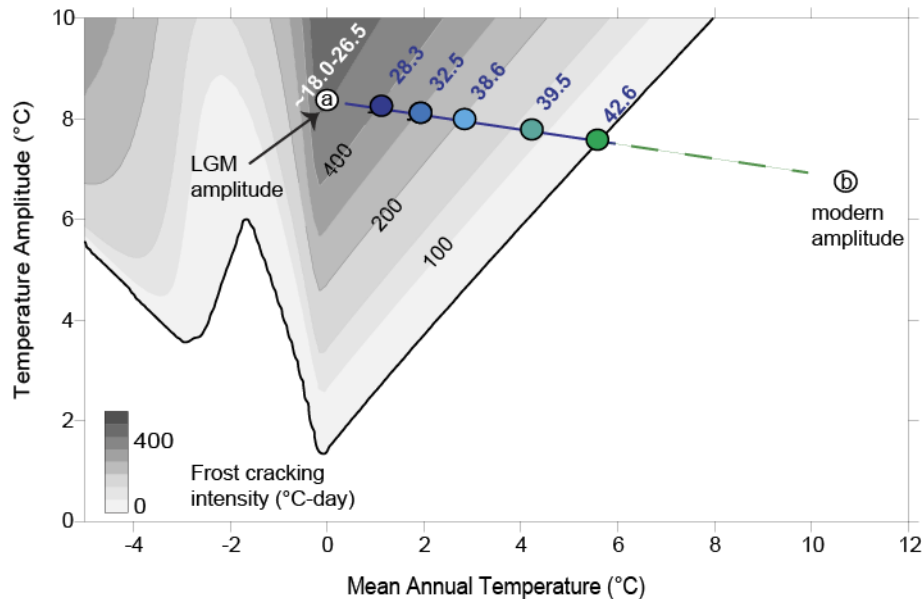


Fig. 4-8. Frost cracking intensity and paleoclimate reconstructions. MAT and amplitude values for Little Lake at 21 ka and the present are delineated by ‘a’ and ‘b’, respectively, on the plot. Line represents change in amplitude from glacial to interglacial intervals. Colored dots are frost cracking intensity at Little Lake for MIS 3 pollen zone intervals (blue numbers in ka) and MIS 2 (white numbers in ka) based on inferred Little Lake temperatures from (Grigg et al., 2001), our core fossil data data (Fig. 4-4) and paleoclimate simulations at 21 ka.

While paleoclimate simulations such as CMIP5/PMIP3 do not go back further in time than 21 ka, the Little Lake paleoclimate reconstruction allows us to infer MAT throughout MIS 3 and 2 and use this information to calculate frost cracking intensity through time. To date there are no inferred temperatures from paleo-vegetation data for Little Lake during MIS 1. Therefore, we restrict our analysis to MIS 2 and 3 using inferred temperatures from Grigg et al. (2001) and our core data.

While the ecosystems fluctuate between temperate and montane forests and an open subalpine setting, the overall trend exhibits cooling through time, with temperate

conditions in <15 % of zone LL-1 and subalpine conditions occurring in > 50% of the recorded climate interval. By 27.8 ka, Little Lake was a subalpine parkland meadow setting, dominated by meadows with scattered trees. These climatic conditions persisted throughout the glacial interval beginning at 26.5 ka when summer insolation decreased. As temperature amplitude increases during glacial interval conditions, we extend a line from the modern Little Lake amplitude to the paleoclimate amplitude at 21 ka. We use this simplistic approach to infer a linear trajectory through time.. Along this amplitude line, we plot frost cracking intensity based on inferred temperatures for the dominant LL-1 subzones (Fig.4-8).

At 42.7 ka (LL-1a), pollen suggests an open hemlock pine forest, with MAT with temperatures cooler than present. Grigg et al. (2001) do not suggest a MAT for this interval. However, on a plot of inferred climate for MIS 3 and 2, they assigned the warmest temperatures of any Little Lake pollen subzone. Additionally, the LL-1a forest type is similar to west side Vancouver Island, with abundant cedar and hemlock, minimal Douglas-fir and some western pine, where January temperatures average ~ 4°C, MAT are ~ 7°C and it rarely snows (*ClimateWNA*, University of British Columbia, <http://climatewna.com/>). We therefore assume that temperatures would have allowed for minor excursions into the frost cracking window and tree-driven processes would have dominated soil production. As temperatures cooled and amplitudes modestly increased, frost weathering intensity would have increased, concurrent with the measured increase in erosion rates (Fig. 4-6). Frost weathering intensity increases from near 0 to ~ 500 °C-day (frost cracking intensity units) as climate cools and the ecosystem changes (Fig.4-8). As subalpine parklands began to dominate over forested settings, frost processes would begin to increasingly control soil production, transport, and erosion. Even during periods when the montane forests returned, January and February temperatures were likely low enough to generate frost weathering over short periods, increasing rock damage and priming the substrate for future disruption.

7.2. Lake history – slow erosion rates and sediment accumulation conundrums

Our erosion rate data goes from $0.214 \pm 0.04 \text{ mm yr}^{-1}$ at 25,650 yrs BP to $0.147 \pm 0.07 \text{ mm yr}^{-1}$ at 25,390 yrs BP. In other words, the measured erosion rate changed 30%

in 260 years. This shift in erosion rates continues for 1750 years, measured in 5 different sample intervals spanning 9.5 m of lake sediments, until just as abruptly erosion rates return to $0.214 \pm 0.02 \text{ mm yr}^{-1}$ at 23,360 years BP. Given that CRN-derived erosion rates integrate concentrations over the length of attenuation (about 80 cm in the Little Lake watershed or $\sim 2\text{-}4$ ky depending on erosion rates), there is no feasible mechanism that could increase measured nuclide concentrations in soils within the watershed by 1.5x over < 400 years (Fig. 4-3).

We suggest that the conundrum of impossible actual erosion rate changes can be attributed to dam breakout events. Based on our lidar data, bench-cut terraces suggest that paleolake levels could have been much as 290 MASL compared to the present day outlet connecting to Triangle Lake at 213 MASL (Fig. 4-1). At a minimum, the lake elevation dropped from 260 MASL to the broad spillway at 240 MASL before cutting an outlet into the landslide deposit to the east-northeast of the former spillway. We envision a series of lake-lowering breakout events, with one significant event around ~ 26 ka. Given lake lowering, sediment stored in steep alluvial fans at the lake's edge would have been remobilized. These lakeside sediments would have continued to accumulate cosmogenic nuclides post-sediment production and their presence in the lake sediments may constrain the timing of at least one of the major dam breakout events. Additionally, all our age-reversed fossils are from the same depth interval as the sediments with high nuclide concentrations further supporting the re-deposition of stored sediments (Fig. 4-5, Table 4-1).

While measured erosion rates track changes in climate-mediated production processes through time (Figs. 4-3, 4-5, 4-8), with erosion rates steadily increasing as climate cools, we do not see a synchronous increase in sediment accumulation rates. Instead, our data shows a 6x increase in sediment accumulation rate starting at ~ 27 ka. The storage and mobilization of hillslope material as the lake lowered through time is one way to increase sediment accumulation rates. However, the steep and dissected topography limits the amount of storage available in the watershed (Fig. 4-1). Given steep hillslope gradients, a MAT of $\sim 0^\circ\text{C}$ during the glacial, and, importantly, a transition from an intermittently forested setting to a subalpine parkland where tree density would have dramatically reduced, we hypothesize that transport rates

dramatically increased during the LGM due to frost creep and solifluction and this is the dominant signal controlling our large increase in sediment accumulation rates during the LGM. Alternatively or additionally, the sudden increase in sediment accumulation rates and increase in grain size and angularity could also be due to a facies change with delta progradation.

7.3. Lag time and actual vs. apparent erosion rates

Our theoretical framework for evaluating measured erosion rates under climate-controlled transient production and mixing conditions allows for consideration of our measured erosion rates in context of climate-mediated changes between biotic and abiotic soil production mechanisms over the past 50 ky in the Little Lake catchment. Apparent erosion rates will lag behind actual erosion rates, as ^{10}Be concentrations integrate erosion rates over millennial time scales. Importantly as soil depth increases, the rate of change of nuclide concentrations in the soil decreases and thus it takes longer for nuclide concentrations to equilibrate.

By combining MATs inferred from paleovegetation data, an LGM climate reconstruction, and a mechanistic frost weathering model, with our ^{10}Be -derived erosion rate data (Figs. 4-3, 4-6 to 4-8) we can qualitatively begin to assess how actual erosion rates may have changed through time in the Little Lake Basin. To fully consider our theoretical framework, we need to assess how mixing depths as well as erosion rates may have changed through time in the unglaciated OCR.

While Little Lake was forested both before and after the last glacial maximum, the forest types differed between an open canopy hemlock-pine forest during much of the MIS 3 pre-LGM interval compared to a closed canopy Douglas-fir forest during the Holocene (Worona and Whitlock, 1995). We speculate that differences in below ground biomass should correlate with mixing depth and vigor. Furthermore, above ground biomass and plant vigor should control soil production rates. In comparing modern OCR hemlock-pine forest metrics (a modern analogue to Little Lake's open canopy forest) with OCR Douglas-fir forest metrics, tree biomass, belowground net primary productivity (NPP) and total NPP in all cases is slightly higher in the Douglas-fir forests than in the hemlock-pine forests (Runyon et al., 1994). Belowground NPP in the open canopy forest measured $3.1 \text{ Mg ha}^{-1} \text{ yr}^{-1}$ compared to $3.8 \text{ Mg ha}^{-1} \text{ yr}^{-1}$ in the closed canopy forest.

Equipped with this information, and with the expectation that both erosion and mixing depths reflect climate-driven changes in ecosystems (Section 5.2), we postulate that erosion rates and mixing depth during the non-glacial interval may have been ~ 80% of erosion rates and mixing depths imposed by the modern Holocene forests. Given that modern Douglas-fir forest soils depths are relatively thin in the OCR (~0.5 m), for the purposes of this qualitative exploration (Heimsath et al., 2001; Reneau and Dietrich, 1991; Roering et al., 2010), we assign a mixing depth of 40 cm to the forested MIS 3 interval and 60 cm to MIS 1.

During the glacial maximum, we speculate that frost heave would have controlled mixing depths. To model lag times between actual and apparent erosion rates, we assign a mixing depth of 20 cm, based on diurnal frost penetration depths from sites in temperate locations, seasonal frost and MAT ~ 0°C (Matsuoka, 2001).

We numerically solve equation 4-4 in an erosion rate model to consider how climate controlled soil production and mixing mechanisms might influence ^{10}Be concentrations through time at our Little Lake site (Fig. 4-9). In this simple scenario, we transition from an open canopy soil production and mixing regime at 50 ka with an erosion rate of 0.06 mm yr^{-1} to a mixed forest-frost weathering regime at 49 ka with erosion rates increasing to 0.15 mm yr^{-1} and mixing depths of 40 cm. By 32 ka, when we impose a new frost-driven erosion rate of 0.25 mm yr^{-1} with mixing depths of 20 cm, apparent erosion rates are 0.16, or only 66% of the actual erosion rates. Under transient conditions, the apparent nuclide-derived erosion rates continue to increase, approaching the actual erosion rate after ~ 6000 years. At 16 ka, as the glacial interval is waning and forests are re-appearing (Grigg et al., 2001), we impose an erosion rate of 0.08 mm yr^{-1} and mixing depths of 60 cm. The 40 cm increase in the mixing depth injects bedrock with low nuclide concentrations into mixed soil zone, which results in an apparent erosion rate spike of 0.38 mm yr^{-1} . However, without further mining of the low nuclide concentration bedrock, apparent erosion rates decrease to 0.23 mm yr^{-1} after only 2000 years, and continue to decline, although equilibrating at slower pace than when mixing depths decrease (Fig. 4-3) as indicated by equation 4-7.

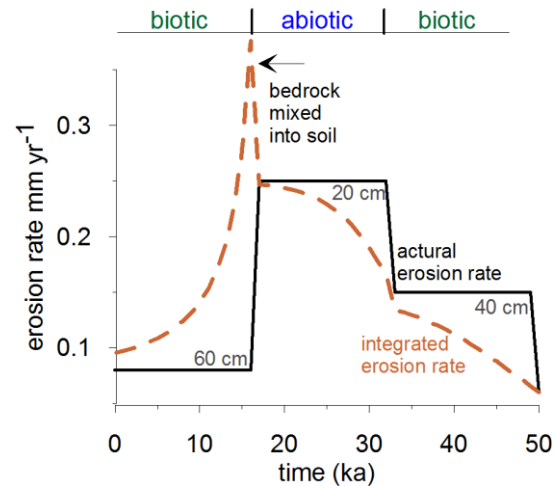


Fig. 4-9. Transient erosion rate and mixing model output. Model parameters (actual erosion rates and vertical mixing depth) based on hypothesized soil production, mixing, and erosion processes through time. Black line delineates modeled actual erosion rates, with model mixing depths noted at each of the three time intervals.

The model, using reasonable mechanistic assumptions based on the paleo-environmental reconstruction, core observations and *a priori* knowledge of the minimum erosion rates from our ^{10}Be derived erosion rates, does reasonably well at broadly replicating measured erosion rates at Little Lake through time. For measured or apparent erosion rates to reach 0.23 mm yr^{-1} by 28.5 ka as we see in our paleoerosion data, glacial frost-driven erosion rates likely increased at least 4x relative to earlier Pleistocene erosion rates from warmer, forested times. Additionally, our model output (and equation 4-7) suggests that without paleoerosion data from the late Pleistocene through the early to mid-Holocene, along with the absence of younger Holocene sediments (Fig. 4-4, Table 4-1), we are unable to determine if modern measured erosion rates have fully equilibrated to actual erosion rates.

7.4. Orbital wobbles, exceptional climates, and steady state

When Kirk Bryan wrote, “The ‘normal’ climate of Davis, i.e., the temperate, humid climate of northeastern United States, northwestern Europe and a few other places, including part of New Zealand, is truly exceptional” (Bryan, 1950), he did not use exceptional as a compliment. Rather he was chastising geomorphologists for their tortuous reasoning in assuming that glacial and arid landscapes were the exceptions rather

than the rule when considering the impact of past climates on modern terrain. In one brief, prescient paragraph, he laid out a conceptual model consistent with our quantitative study. Given the length of glacial intervals relative to interglacial interval, Bryan urged geomorphologists to re-consider the impact of past climates. In seemingly steady state unglaciated soil-mantled terrain - Bryan's 'rare' settings - not only is the signal of past climates difficult to discern, but perhaps we have come to expect at most a modest impact compared to the observations of Gilbert (1890) and others on the vast Pleistocene pluvial lakes or Huntington's terraces (Huntington et al., 1914) in the arid west (Bryan 1928).

Yet our results at Little Lake, over 400 km to south of the maximum extent of the Cordilleran ice sheet, highlight that climate wrought at a minimum a 2.5x increase in erosion rates during the LGM relative to modern measured erosion rates. While previous studies have argued that climate only weakly controls nonglacial erosion rates (e.g., Riebe et al 2001) our data contradicts this tenet. The contradiction likely arises from two problematic approaches to discerning the impact of climate on landscapes 1) comparing among sites with their varied landscape histories and forcing mechanisms (e.g. Riebe et al., 2001a) and 2) seeking a signal in precipitation rather than temperature (Champagnac et al., 2014).

Our data, here and in Chapter 3, suggests that the well-studied Oregon Coast Range, and indeed other unglaciated mid-latitude terrain likely experienced accelerated sediment production during glacial intervals. Other studies are also emerging in recent years that point to accelerated sediment production and erosion during the last glacial in unglaciated settings. (Champagnac et al., 2014; Heimsath, 2006; Mason and Knox, 1997; Schaller et al., 2004; Tucker et al., 2011). This invites a re-evaluation of what constitutes a steady state landscape. Following Bryant's lead, we suggest consideration of time spent in the lengthy glacial intervals (40-100 ky) compared to the much briefer interglacial interval (typically 10-15 ky), may be the dominant control on landscape evolution – due to both the climate-driven mechanical strength of frost-driven processes and the interval length (Fig. 4-10). Interglacial conditions, similar to the modern, are found in only ~ 10 % of the ~ 750,000 extensive, detailed quaternary records extracted from ice cores, ocean sediments, and palynology records (Barry, 2013). Even assuming modest 2x increase in erosion rates, over a 70 ky glacial interval compared to a 15 ky interglacial interval,

implies only 10% of a landscape's trajectory can be attributed to interglacial intervals. Perhaps increased sediment accumulation rates measured worldwide since the onset of the Pleistocene (Zhang et al., 2001) is not due to a cyclic response to climatic perturbations, but are simply the norm, as glacial intervals and their powerful erosive mechanisms may dominate the geomorphic legacy even in mid-latitude non-glaciated terrain.

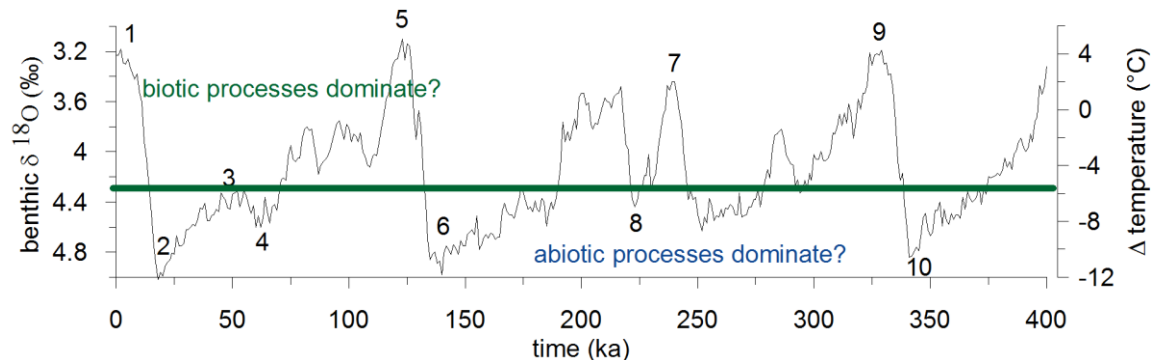


Fig. 4-10. Climate fluctuations over the last 400 ka. LR04 benthic $\delta^{18}\text{O}$ stack constructed by the graphic correlation of 57 globally distributed benthic $\delta^{18}\text{O}$ record versus LR04 depth-age model (Lisiecki and Raymo, 2005). Data downloaded from <http://www.lorraine-lisiecki.com/stack.html> including the ages of the MIS boundaries. Temperature aligned with benthic $\delta^{18}\text{O}$ stack based on EPICA Dome C Ice Core 800 ky deuterium data and temperature estimates (Jouzel et al., 2007). Data downloaded from <http://www.ncdc.noaa.gov/data-access/paleoclimatology-data/datasets/ice-core> (Last updated 11/26/2007). While the benthic stack data extends to 5.3 Myr, we limit the data set to 400 ka to allow for observation of the details of the glacial vs. interglacial interval length. Suggested transition between biotic and abiotic soil production and erosion delineated with horizontal green line.

8. CONCLUSIONS

By coupling diverse tools and analyses, including downscaled paleoclimate GCM simulations, a frost weathering model, sedimentology, paleoecology and isotopic-derived paleoerosion data from a new sediment archive extracted from a 50 ka paleo-lake deposit, we document climate-mediated ecosystem influence on erosion rates over 3 climatic intervals. ^{10}Be -derived erosion rates more triples as the unglaciated Oregon Coast Range transitioned from the open forest-dominated MIS 3 pre-LGM climate interval into the periglacial subalpine MIS 2 LGM interval. Measured erosion rates fell again by more than half as the subalpine ecosystem gave way to the modern MIS 1 closed canopy

Douglas-fir forest. Our findings contradict previous work that suggest climate has only weak control on erosion rates and challenge the notion that modern processes in unglaciated mid-latitude terrain can be projected into the past beyond the current, relatively brief interglacial interval.

We have demonstrated that in our Oregon Coast Range setting, abiotic frost weathering is at a minimum 2.5x more efficient as an erosion agent than tree-driven processes. Additionally with the transition from a forested to subalpine parkland setting, sediment accumulation rates increased by up to a factor of 6, although the rate change is likely inflated due to re-mobilization of alluvial fan sediments. By employing a transient framework, that incorporates changing mixing depths and erosion rates in considering nuclide inventories in a soil column, we establish the importance of soil depth in controlling the lag time for measured erosion rates to equilibrate to actual erosion rates. Coupling paleo-vegetation-derived climate information with core observations we model frost weathering intensity from ~ 43 ka to 21 ka and establish a correspondence with increasing frost weathering intensity and increasing ^{10}Be -derived erosion rates. Utilizing this information and reasonable mixing depths for open and closed canopy forests (MIS 3 and MIS I) and a subalpine setting (MIS 2), in a transient mixing depth and erosion rate model, we are able to broadly replicate measured erosion rates at our site. Our model results suggest that actual LGM erosion rates, driven by frost processes, are likely minimally 3x greater than tree-driven erosion rates in more temperate climates.

Our findings encourage a re-evaluation of what constitutes steady state in soil-mantled unglaciated settings. Importantly, lengthy glacial intervals with their highly efficient abiotic erosion mechanisms relative to short interglacial intervals and biotic-driven erosion mechanisms may be the ultimate pacesetters controlling landscape evolution in unglaciated terrain.

APPENDIX A
SUPPLEMENTARY MATERIAL FOR CHAPTER II

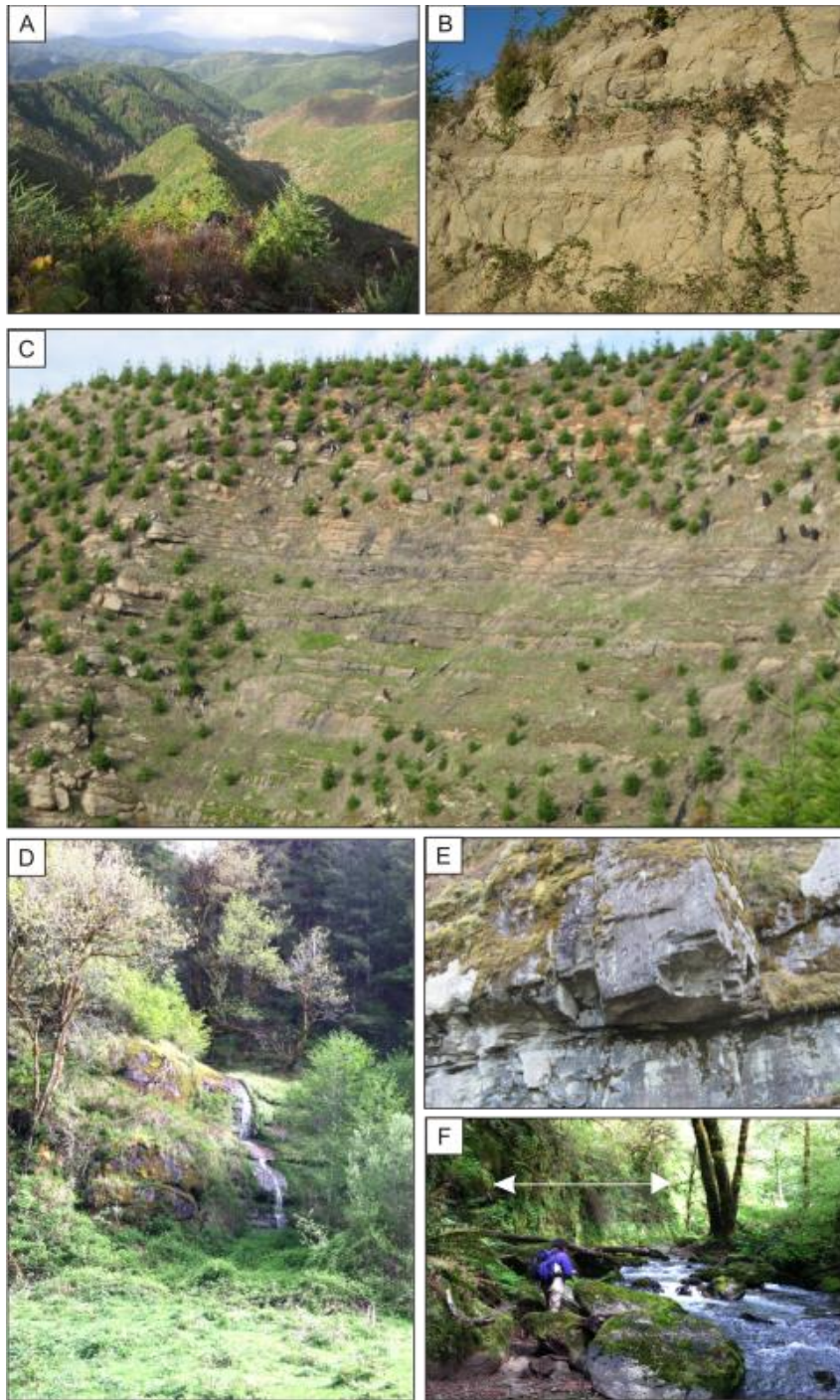


Figure S1. Pictures of ‘typical’ and ‘resistant’ Tye Formation. A) Steep, soil-mantled hillslopes with uniform ridge and valley spacing in the Oregon Coast Range. Underlying bedrock is the typical Tye. B) Fracture spacing in the typical Tye. C) Swath of resistant Tye. Note the lack of trees, soil or vertically orientated fractures on the resistant swath. Sapling diameters on the surrounding typical Tye are ~ 1m. D) Resistant rock knickpoint in Franklin watershed. E) Block failure in the resistant Tye. F) Resistant boulders in Franklin Creek (foreground). Arrow delineates resistant rock cliff.

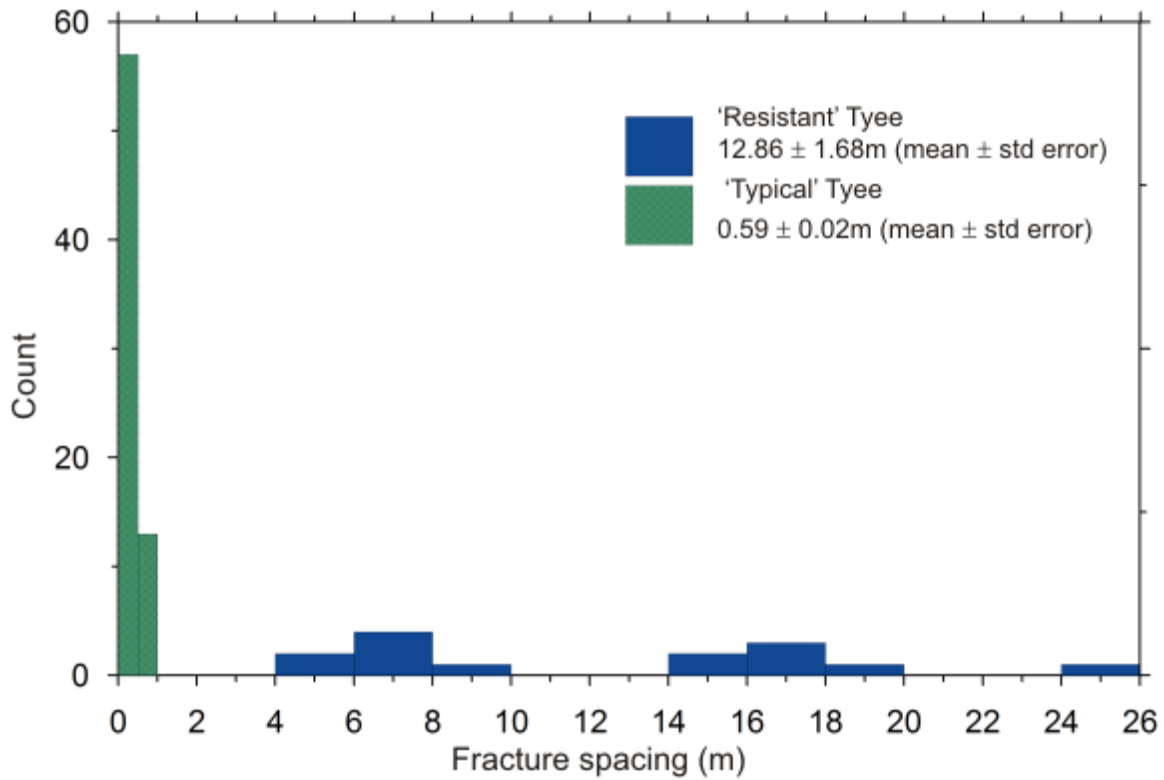


Figure S2. Histogram comparing fracture spacing in the 'typical' Tyee (green stippled bars) with fracture spacing in the 'resistant' Tyee (solid blue bars). We measured vertical fracture spacing over 42m length of the typical Tyee and 180m length of the resistant Tyee.

APPENDIX B

SUPPLEMENTARY MATERIAL FOR CHAPTER III

LITTLE LAKE

Paleolake setting and sample site selection. Paleolake deposits can yield information on past ecosystems, changes in mineral and organic characteristics, sediment accumulation and erosion rates. In order to optimize paleo-environmental reconstructions, previous researchers collected core data in the fine-grained deposits along the distal fen of the modern Little Lake (1, 2). For our study, we sited our core location upstream of the modern lake to satisfy the following criteria and considerations. Given our primary goal of deriving erosion rates from the quartz-rich deposits, we sought to maximize the occurrence of hillslope-derived deposits and thus set our core location in the valley axis proximal to the sediment source area. The samples required sufficient quartz mass to obtain erosion rates over short (< 1000 years) time intervals from sediments with a size range 0.25 mm – 2 mm within the 63.5 mm diameter core. While our sample site (Fig. 3-S1) proved optimal for these ^{10}Be criteria, at the same time it was less optimal for continuous Late Pleistocene-Holocene deposition, as the paleolake location had transitioned from a depositional setting to intermittently erosional by ~20 kya. For the upper 29 m of the core drive, we subsampled the paleo-sediments, with continuous sampling from 30 m downward. Paleoarchive depositional environment preservation in the core is excellent from 4 m below the surface to the original valley bottom.

Paleoclimate archives - data and previous reconstructions. Paleoclimate reconstructions from the Little Lake fen deposits support our core data and paleoclimate simulation results (Fig. 3-S2). The transition from finely laminated sediments to coarse angular blue-grey grains in our core corresponds with last glacial pollen zones LL-1 (42.5 ka -27 ka) and LL-2 (27-13 ka) (thousands of calibrated years median before present) (1, 2). The open canopy forest of LL-1 and the sub-alpine parkland of LL-2 correspond to the latter part of MIS 2 and MIS 3, respectively. Climate estimates based on modern analogues to pollen found in the Little Lake core suggest that temperatures would have been 7° - 11°C cooler than present (14). With the co-occurrence of *Picea sitchensis* (Sitka

spruce) and *Abies lasiocarpa* (subalpine fir), we estimate MAT at Little Lake to be 10°C colder than present day, based on paleoclimate simulations (MAT =1°C) and modern MAT of 11°C. While climate fluctuated between cold to colder during LL-2, the overall average remained steady. Pollen data suggests that average precipitation at Little Lake was 250-500 mm less than present day (2) similar to LGM precipitation values derived from paleoclimate simulations (Fig. 3-S3).

EROSION RATE DATA

Steadily eroding landscape formulations applied to landscapes with variable erosion rates and methods. Cosmogenic nuclides such as ^{10}Be , ^{26}Al , and ^3He , are standard tools for dating rock surfaces and calculating soil production and erosion rates. As secondary cosmic rays bombard the Earth's surface, they produce rare cosmogenic nuclides within mineral grains. As bedrock erodes, minerals such as quartz within the rock are brought to the surface, accumulating cosmogenic nuclides along the way. The accumulation rate depends on depth beneath the surface, as the secondary cosmic rays attenuate approximately exponentially by mass, with an effective attenuation length equivalent to the depth required to traverse $\sim 160 \text{ g cm}^{-2}$. For rock with a density of 2 g cm^{-3} , such as the bedrock at our study site, this corresponds to a depth of 80 cm. It also depends on the local production rate, which is a function of latitude and elevation. The integrated accumulation of cosmogenic nuclides within a mineral grain depends on the amount of time that the grain spends near the surface. The slower a site erodes, the more nuclides it accumulates. We direct the interested reader to the extensive literature on the topic for more detailed explanations (3–5) Because cosmogenic nuclides accumulate in the uppermost $\sim 1\text{m}$, they are relatively insensitive to small changes in soil depth or rapid changes in erosion rates such as we observe in the Little Lake pollen data (1). In rapidly eroding catchments such as ours in the Oregon Coast Range, with erosion rates ranging from $0.1\text{-}0.2 \text{ mm yr}^{-1}$, ^{10}Be integrates erosion rates over a timescale of 3,000-6,000 years, exponentially weighted towards the present. Although our work shows that erosion rates have changed through time, we nonetheless model erosion rates as steady-state equivalent, following standard practice in the literature. The steady-state assumption overestimates true erosion rates when erosion rates are slowing over time and

underestimates true erosion rates when erosion rates are increasing (4, 6). At our site, the observed paleo erosion rates are likely a minimum value because we expect that erosion rates had increased from pre-LGM values. By contrast, given the abrupt warming at the transition from the LGM to the Holocene and the rapid transition from a cold subalpine setting to Douglas fir forests (1), modern day cosmogenic nuclide concentrations in river sediments have had sufficient time to equilibrate to modern processes and thus likely approximate actual erosion rate values.

Methods and comparison with previous OCR erosion rate data. We determined erosion rates using a spatially averaged production rate weighted by basin hypsometry (Table 3-S2). Using the CRONUS calculator (<http://hess.ess.washington.edu/>) (7), we calculated production rates by nucleon spallation. All core samples have a spallogenic production rate of $5.92 \text{ at g}^{-1} \text{ yr}^{-1}$; Trib 1 and Trib 2 have spallogenic production rates of 6.42 and $6.69 \text{ at g}^{-1} \text{ yr}^{-1}$, respectively. We estimated production due to muons following previous work (8) using revised muon production cross sections (9). Erosion rates are sufficiently fast that we ignored radioactive decay. We also ignored quartz enrichment due to chemical erosion, which we expect to be similar across all samples. Alternative production estimates that incorporate older muon production in samples with high erosion rates, such as the CRONUS calculator, generate erosion rates that are $\sim 25\%$ greater than the method we used. Using the CRONUS calculator, mean LGM erosion rates are $0.29 \pm 0.1 \text{ mm yr}^{-1}$ compared to CRONUS-calculated modern erosion rates of $0.11 \pm 0.1 \text{ mm yr}^{-1}$ in the Little Lake basin. Our modern ^{10}Be -derived erosion rates at Little Lake are consistent with average catchment-derived erosion rates throughout the Oregon Coast Range (10). Regardless of the method used, ^{10}Be -derived erosion rates in the Little Lake Basin are $\sim 2.5\text{x}$ faster during the LGM when compared to modern.

REFERENCES

1. Worona MA, Whitlock C (1995) Late Quaternary vegetation and climate history near Little Lake, central Coast Range, Oregon. *Geol Soc Am Bull* 107(7):867–876.
2. Grigg LD, Whitlock C, Dean WE (2001) Evidence for Millennial-Scale Climate Change During Marine Isotope Stages 2 and 3 at Little Lake, Western Oregon, U.S.A. *Quat Res* 56(1):10–22.

3. Lal D (1991) Cosmic ray labeling of erosion surfaces: in situ nuclide production rates and erosion models. *Earth Planet Sci Lett* 104(2-4):424–439.
4. Von Blanckenburg F (2005) The control mechanisms of erosion and weathering at basin scale from cosmogenic nuclides in river sediment. *Earth Planet Sci Lett* 237(3-4):462–479.
5. Granger DE, Riebe CS (2014) Cosmogenic Nuclides in Weathering and Erosion. *Treatise on Geochemistry*, ed Drever JI (Elsevier, London), pp 401–436. 2nd Ed.
6. Schaller M, Ehlers TA (2006) Limits to quantifying climate driven changes in denudation rates with cosmogenic radionuclides. *Earth Planet Sci Lett* 248(1-2):153–167.
7. Balco G, Stone JO, Lifton NA, Dunai TJ (2008) A complete and easily accessible means of calculating surface exposure ages or erosion rates from ^{10}Be and ^{26}Al measurements. *Quat Geochronol* 3(3):174–195.
8. Granger DE, Muzikar PF (2001) Dating sediment burial with in situ-produced cosmogenic nuclides: theory, techniques, and limitations. *Earth Planet Sci Lett* 188(1-2):269–281.
9. Balco G, Soreghan GS, Sweet DE, Marra KR, Bierman PR (2013) Cosmogenic-nuclide burial ages for Pleistocene sedimentary fill in Unaweep Canyon, Colorado, USA. *Quat Geochronol* 18:149–157.
10. Balco G, Finnegan N, Gendaszek a., Stone JOH, Thompson N (2013) Erosional response to northward-propagating crustal thickening in the coastal ranges of the U.S. Pacific Northwest. *Am J Sci* 313(8):790–806.

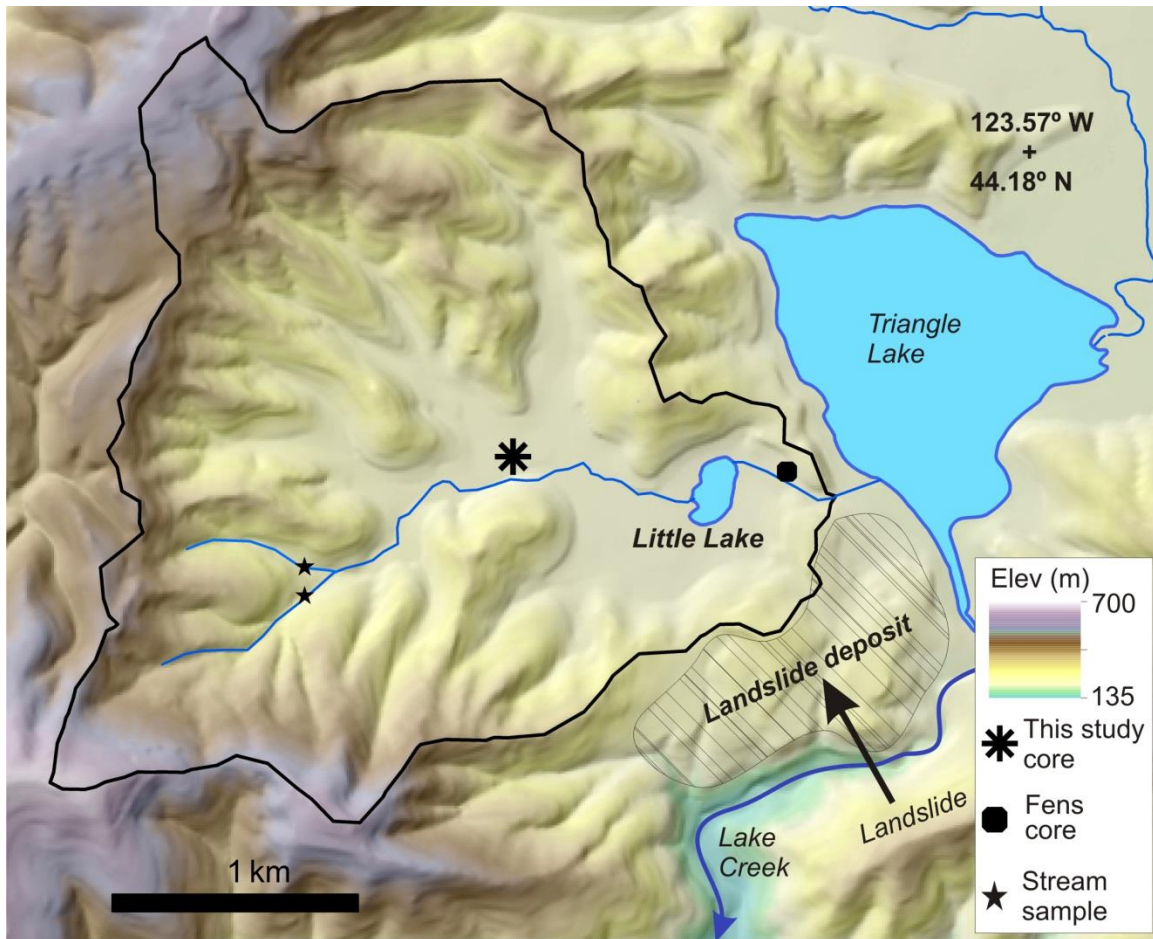


Fig. 3-S1. Map of the Little Lake catchment and sample sites. Core data location for this study marked with an asterisk. Previous paleoecology data collected in the fens near the Little Lake outlet marked with a polygon. Modern stream sample locations delineated with stars. Map shows only a portion of the larger landslide-dammed paleolake deposit which extends to the east of Triangle Lake.

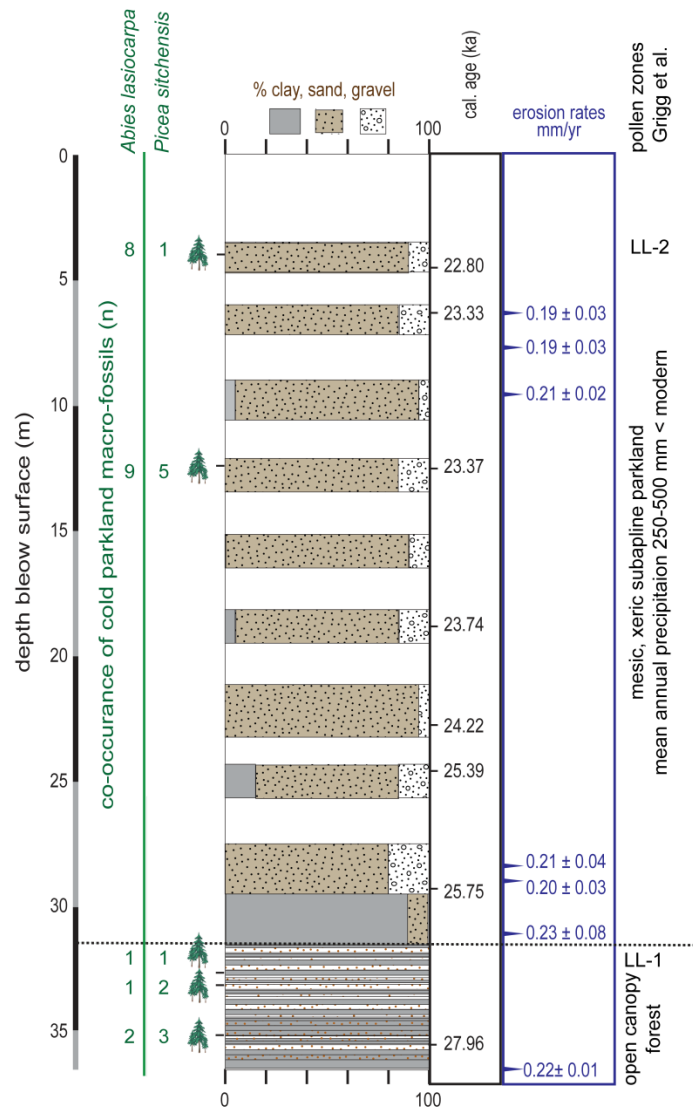


Fig 3-S2. Compilation of Little Lake core observations and data. *Picea sitchensis* (Sitka spruce) and *Abies lasiocarpa* (subalpine fir) co-occurrence observed at 29.5 to 22.6 ka (thousands of calibrated years median before present (BP)) based on depth-age model. Numbers to the left of the tree icons are macrofossil counts for each species at each interval. For simplicity, we only do not include macrofossil counts at 29.5 ka (3 *Picea sitchensis* and 4 *Abies lasiocarpa*). Percent clay, sand and silt in the core based on visual observations. The entire core sequence consists of mm-cm scale laminated lacustrine deposits, with a significant reduction in fine-scale laminations, increase in grain size and an increase in sediment accumulation rates at ~ 26 ka, the start of last glacial (MIS 2) interval. Median calibrated ages based on the CLAMS model best fit. While the core extends over 50 ky, for the purpose of this study, we only present data relevant to the time interval of interest.

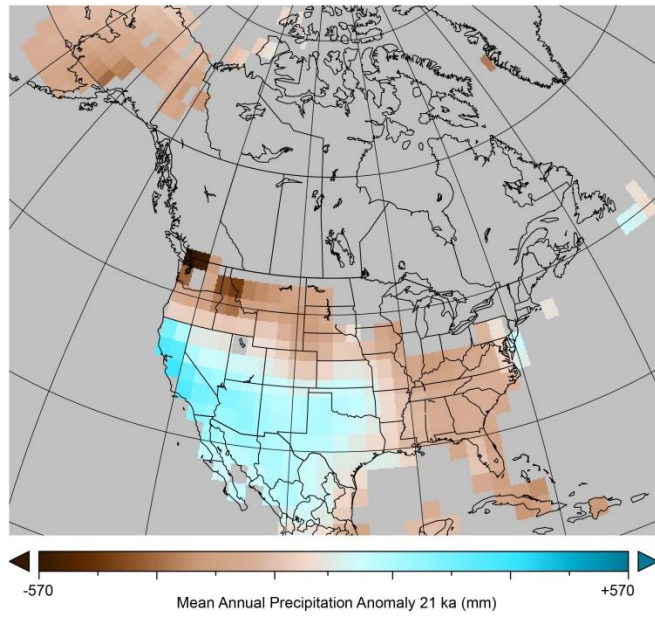


Fig. 3-S3. Precipitation anomaly map. Modern mean annual precipitation (MAP) minus the MAP 21 ka derived from the mean of the CMIP5 ensemble paleoclimate simulations. Brown colors represent drier LGM conditions while blue colors represent wetter LGM conditions relative to modern.

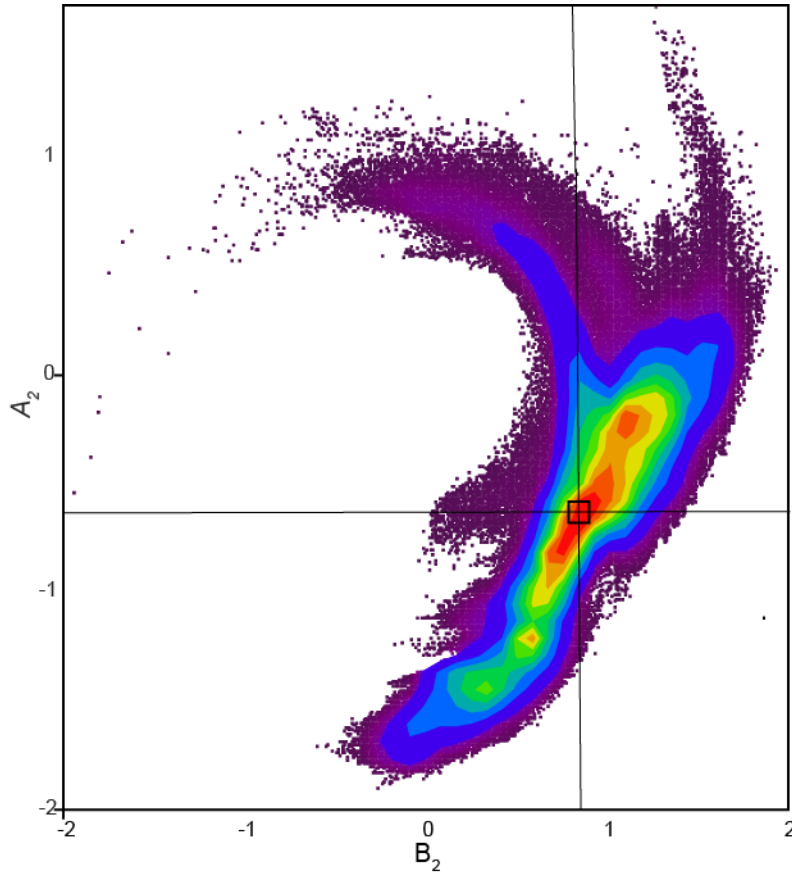


Fig. 3-S4. Additional information on frost cracking intensity phase map (Fig. 3-3 in main text). To generate a representative frost cracking intensity phase map we used values for coefficients B_1 , A_2 and B_2 drawn from the range of best-fit coefficients by fitting the annual temperature curves generated from mean monthly temperature data derived from the downscaled paleoclimatic simulations ($n = 614,145$) across our grid domain. By varying A_1 and MAT, we generated a suite of amplitude values and annual temperature curves. To produce realistic annual temperature curves, we set B_1 to -1.5 (data set mean = -2.1 ± 1.5 standard deviation, median = -2.0). Coefficient values for the 2nd harmonic selected from the centre of the 0.9 quantile nonparametric bivariate density plot when plotting A_2 vs. B_2 . The lowest density values are colored purple with the highest concentration of values (90%) colored red. Large square in center of plot outlines the values used for Figure 2 where we set $A_{2_{10}}$ -0.6280 and B_2 to 0.87 .

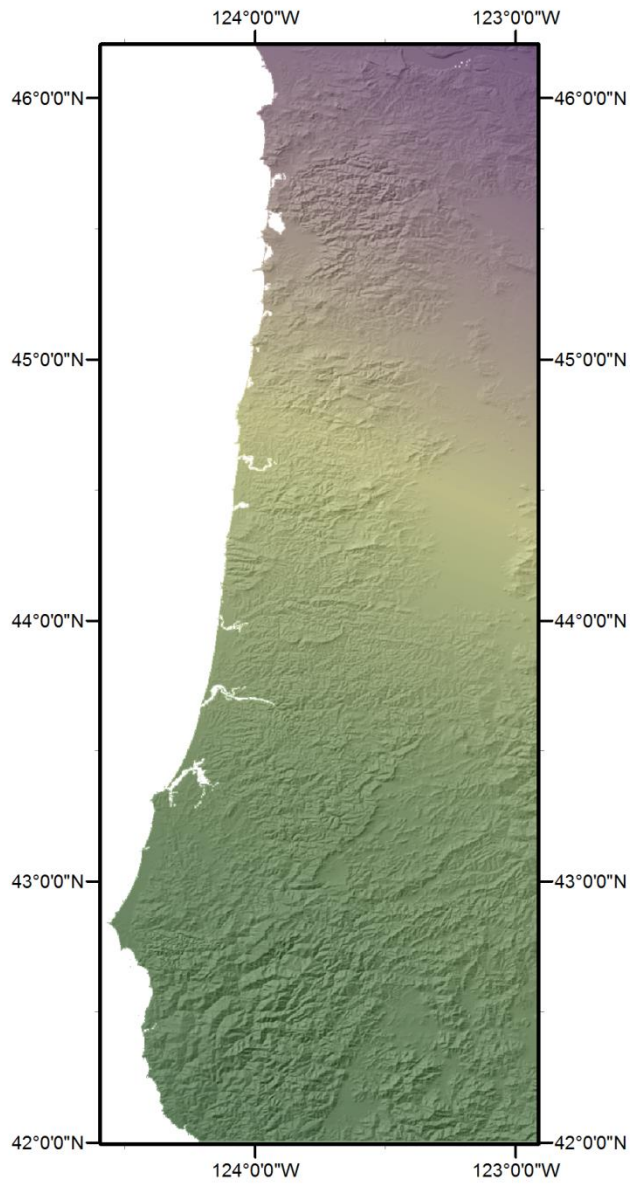


Fig. 3-S5. Temperature anomaly map. Modern mean annual temperatures (MAT) minus the MAT 21 ka derived from the downscaled MIROC temperature simulations. Cooler (green) colors represent smaller temperature anomalies between the LGM and modern non-glacial interval, while the greatest MAT anomalies are in the warmest (purple) colors. Note that the MAT difference increases from south to north.

TABLE 3-S1

14C data and depths used in depth-age model

Sample	CAMS ID#	Depth m	¹⁴ C age years	Error years	Min 95% years	Max 95% years
C14tip	155166	-4.57	19030	50	22.68	23.15
C20tip	152768	-6.40	19390	70	23.07	23.58
C40tip	153571	-12.50	19410	60	23.11	23.59
C60tip	153573	-18.59	19720	70	23.49	23.99
B74c	156945	-22.82	20150	70	24.00	24.44
C83a	156946	-25.15	21030	80	25.15	25.60
B96tip	156032	-29.69	21425	45	25.61	25.89
B114tip	158582	-36.28	23880	150	27.69	28.62

All samples processed at Lawrence Livermore National Laboratories Center for Accelerator Mass Spectrometry (CAMS). All samples consisted of a single piece of wood with the exception of B1tip, which contained two pieces of adjoining wood extracted from the core.

TABLE 3-S2.

Cosmogenic nuclide data and calculated erosion rates

Sample	PRIME ID	Qz mass (g)	Be mass (g)	¹⁰ Be/ ⁹ Be (10 ⁻¹⁵)	Blank* (10 ³ at)	[¹⁰ Be] (10 ³ at g ⁻¹)	Erosion rate [†] (mm yr ⁻¹)	Core depth (m)	Age (ky)
C20b	201201500	22.41	284.8	44 ± 5	239 ± 28	26.8 ± 4.4	0.19 ± 0.03	-6.25	23.33
C23b+c	201201501	16.32	260.0	39 ± 3	239 ± 28	26.6 ± 3.4	0.19 ± 0.03	-7.16	23.35
C30b+tip	201201502	30.72	255.2	57 ± 4	239 ± 28	23.9 ± 2.4	0.21 ± 0.02	-9.45	23.56
C93c	201201512	16.63	257.3	37 ± 4	239 ± 28	23.9 ± 4.4	0.21 ± 0.04	-28.50	25.64
B96d	201201513	18.65	258.9	42 ± 4	239 ± 28	26.2 ± 4.0	0.20 ± 0.03	-28.96	25.67
C103a	201201515	12.52	285.6	27 ± 5	239 ± 28	22.1 ± 8.0	0.23 ± 0.08	-31.24	26.70
B118b+c	201201516	15.46	271.2	32 ± 5	239 ± 28	22.1 ± 6.1	0.22 ± 0.06	-37.50	28.48
Trib 1	201201864	12.85	274.2	63 ± 7	147 ± 21	53.8 ± 7.3	0.10 ± 0.01	n/a	n/a
Trib 2	201201863	20.05	269.2	68 ± 8	147 ± 21	78.6 ± 10.1	0.07 ± 0.01	n/a	n/a

*The ¹⁰Be samples reported here suffered from an unusually high blank because of contamination in the chemistry lab. Although the level of contamination was high, it was highly reproducible. The core samples reported here were bracketed by four different blanks, two of which were analysed twice. The tributary samples were run separately and were bracketed by two different blanks. We corrected the concentrations of ¹⁰Be for the contamination by subtracting a fixed number of ¹⁰Be atoms regardless of sample mass. The laboratory contamination has since been corrected.

[†]Uncertainties in erosion rate reflect errors in AMS measurements of samples and blanks and do not include uncertainties in production rates.

Bedrock density for all samples is 2.0 g cm⁻³.

REFERENCES CITED

Chapter II

- Aalto, R., T. Dunne, and J. L. Guyot (2006), Geomorphic Controls on Andean Denudation Rates, *J. Geol.*, 114(1), 85–99, doi:10.1086/498101.
- Ahnert, F. (1987), Approaches to dynamic equilibrium in theoretical simulations of slope development, *Earth Surf. Process. Landforms*, 12(1), 3–15, doi:10.1002/esp.3290120103.
- Aldrich, F. T. (1972), A chorological analysis of the grass balds in the Oregon Coast Range, PhD Dissertation, Oregon State University, 31 May.
- Allen, G. H., J. B. Barnes, T. M. Pavelsky, and E. Kirby (2013), Lithologic and tectonic controls on bedrock channel form at the northwest Himalayan front, *J. Geophys. Res. Earth Surf.*, 118(July), doi:10.1002/jgrf.20113.
- Al-Tahini, A., C. Sondergeld, and Rai C. (2006), The effect of cementation on the mechanical properties of sandstones, *SPE Reserv. Eval. Eng.*, 94(6), 306–316.
- Baldwin, E. (1961), Geologic map of the lower Umpqua River area, Oregon: *US Geol. Survey Map OM*, 204, no. 1963, scale 1:62:500., Washington D.C.
- Bennie, A. T. P. (1996), Growth and mechanical impedance, in *Plant roots: The hidden half*, edited by Y. Waisel, A. Eshel, and U. Kafkafi, pp. 393-414, Marcel Dekker, Inc., New York.
- Bierman, P., E. Clapp, K. Nichols, A. Gillespie, and M. Caffee (2001), Using cosmogenic nuclide measurements in sediments to understand background rates of erosion and sediment transport, *Landsc. Eros. Evol. Model. New York, Kluwer*, 89–116.
- Butenuth, C. (1997), Comparison of tensile strength values of rocks determined by point load and direct tension tests, *Rock Mech. Rock Eng.*, 30(1), 65–72, doi:10.1007/BF01020114.
- Callen, R. (1984), Clays of the palygorskite-sepiolite group: depositional environment, age and distribution, *Dev. Sedimentol.*, 37, 1–37, doi.org/10.1016/S0070-4571(08)70027-X.
- Chan, M. A. (1985), Correlations of diagenesis with sedimentary facies in Eocene sandstones, western Oregon, *SEPM J. Sediment. Res.*, Vol. 55(3), 0322–0333, doi:10.1306/212F86B6-2B24-11D7-8648000102C1865D.

- Chan, M. A., and R. H. Jr. Dott (1983), Shelf and deep-sea sedimentation in Eocene forearc basin, western Oregon-Fan or non-fan, *Am. Assoc. Pet. Geol. Bull.*, 67(11), 2100–2116.
- Clarke, B. A., and D. W. Burbank (2010), Bedrock fracturing, threshold hillslopes, and limits to the magnitude of bedrock landslides, *Earth Planet. Sci. Lett.*, 297(3-4), 577–586, doi:10.1016/j.epsl.2010.07.011.
- DiBiase, R. A., K. X. Whipple, A. M. Heimsath, and W. B. Ouimet (2010), Landscape form and millennial erosion rates in the San Gabriel Mountains, CA, *Earth Planet. Sci. Lett.*, 289, 134–144, doi:10.1016/j.epsl.2009.10.036.
- DiBiase, R. A., A. M. Heimsath, and K. X. Whipple (2012), Hillslope response to tectonic forcing in threshold landscapes, *Earth Surf. Process. Landforms*, 37(8), 855–865, doi:10.1002/esp.3205.
- Dietrich, W.E., D. G. Bellugi, L. S. Sklar, J. D. Stock, A. M. Heimsath, and J. J. Roering (2003), Geomorphic transport laws for predicting landscape form and dynamics, in *Prediction in Geomorphology*, Geophys. Monogr. Ser, vol. 135, edited by P. R. Wilcock, and R. M. Iverson, pp. 103–132, AGU, Washington, D. C.
- Dietrich, W. E., and T. Dunne (1978), Sediment budget for a small catchment in mountainous terrain, *Z. Geomorph. N.F.*, 29, 191–206, doi:10.1007/s10069-002-0008-0.
- Dott, R. H. Jr. (1966), Eocene deltaic sedimentation at Coos Bay, Oregon: Jour, *J. Geol.*, 74, 373–420.
- Dumitru, T. A., W. G. Ernst, J. E. Wright, J. L. Wooden, R. E. Wells, L. P. Farmer, A. J. R. Kent, and S. A. Graham (2012), Eocene extension in Idaho generated massive sediment floods into the Franciscan trench and into the Tyee, Great Valley, and Green River basins, *Geology*, 41(2), 187–190, doi:10.1130/G33746.1.
- Duvall, A., E. Kriby, and D. Burbank (2004), Tectonic and lithologic controls on bedrock channel profiles and processes in coastal California, *J. Geophys. Res.*, 109, doi:10.1029/2003JF000086.
- Ferrier, K. L., J. T. Perron, S. Mukhopadhyay, M. Rosener, J. D. Stock, K. L. Huppert, and M. Slosberg (2013), Covariation of climate and long-term erosion rates across a steep rainfall gradient on the Hawaiian island of Kaua’i, *Geol. Soc. Am. Bull.*, 125(7-8), 1146–1163, doi:10.1130/B30726.1.
- Franklin, J. F., and C. T. T. Dyrness (1988), *Natural vegetation of Oregon and Washington*, US Government Printing Office, Washington, D. C.

- Gabet, E. J., and S. M. Mudd (2010), Bedrock erosion by root fracture and tree throw: A coupled biogeomorphic model to explore the humped soil production function and the persistence of hillslope soils, *J. Geophys. Res.*, *115*, doi:10.1029/2009JF001526.
- Galan, E. (1996), Properties and applications of palygorskite-sepiolite clays, *Clay Miner.*, *31*(4), 443–453, doi:10.1180/claymin.1996.031.4.01.
- Galloway, W. E. (1974), Deposition and diagenetic alteration of sandstone in northeast Pacific arc-related basins: Implications for graywacke genesis, *Geol. Soc. Am. Bull.*, *85*(3), 379, doi:10.1130/0016-7606(1974)85<379:DADAOS>2.0.CO;2.
- Galloway, W. E. (1979), Diagenetic control of reservoir quality in arc-derived sandstones: implications for petroleum exploration, *Asp. Diagenes. Soc. Econ. Paleontol. Mineral. Spec. Publ. 26*, 251–261.
- Gilbert, G. K. (1877), Report on the geology of the Henry Mountains: US Geographical and Geological Survey of the Rocky Mountain Region, Gov. Print Off., Washington. D. C.
- Hack, J. (1957), Studies of longitudinal stream profiles in Virginia and Maryland: *U.S. Geol. Survey Prof. Paper 294-B*, 94 p.
- Hack, J. (1973), Drainage adjustment in the Appalachians, in *Fluvial Geomorphology*, edited by M. Morisawa, pp. 51–69, Binghamton, State University of New York.
- Hanley, J. T. (1977), Fourier analysis of the Catawba Mountain knolls, Roanoke county, Virginia, *J. Int. Assoc. Math. Geol.*, *9*(2), 159–163, doi:10.1007/BF02312510.
- Harrison, J. M., and C.-P. P. Lo (1996), PC-based two-dimensional discrete Fourier transform programs for terrain analysis, *Comput. Geosci.*, *22*(4), 419–424.
- Hawthorne, N. (1854), Sketches from memory: The notch of the White Mountains, in *Mosses from an Old Manse*, retrieved from: <http://www.eldritchpress.org/nh/sfm.html>.
- Hayes, J. (1979), Sandstone diagenesis — the hole truth, *Asp. Diagenes. SEPM Spec. Publ. 26*, 127–139.
- Heimsath, A. M., W. E. Dietrich, K. Nishiizumi, and R. C. Finkel (1997), The soil production function and landscape equilibrium, *Nature*, *388*, 21–24, doi:10.1144/SP312.8.
- Heimsath, A. M., W. E. Dietrich, K. Nishiizumi, and R. C. Finkel (2001), Stochastic processes of soil production and transport: erosion rates, topographic variation and cosmogenic nuclides in the Oregon Coast Range, *Earth Surf. Process. Landforms*, *26*(5), 531–552, doi:10.1002/esp.209.

- Heimsath, A. M., R. A. DiBiase, and K. X. Whipple (2012), Soil production limits and the transition to bedrock-dominated landscapes, *Nat. Geosci.*, 5(3), 210–214, doi:10.1038/ngeo1380.
- Heller, P. L., and W. R. Dickinson (1985), Submarine ramp facies model for delta-fed, sand-rich turbidite systems, *Am. Assoc. Pet. Geol. Bull.*, 69(6), 960.
- Heller, P. L., and P. T. Ryberg (1983), Sedimentary record of subduction to forearc transition in the rotated Eocene basin of western Oregon, *Geology*, 11(7), 380, doi:10.1130/0091-7613(1983)11<380:SROSTF>2.0.CO;2.
- Heller, P. L., Z. E. Peterman, J. R. O’Neil, and M. Shafiqullah (1985), Isotopic provenance of sandstones from the Eocene Tyee Formation, Oregon Coast Range, *Geol. Soc. Am. Bull.*, 96, 770-780, doi:10.1130/0016-7606(1985)96<770:IPOSFT>2.0.CO;2.
- Heller, P. L., R. W. Tabor, and C. a. Suczek (1987), Paleogeographic evolution of the United States Pacific Northwest during Paleogene time, *Can. J. Earth Sci.*, 24(8), 1652–1667, doi:10.1139/e87-159.
- Heller, P. L., P. R. Renne, and J. R. O’Neil (1992), River mixing rate, residence time, and subsidence rates from isotopic indicators: Eocene sandstones of the US Pacific Northwest, *Geology*, 20(12), 1095–1098, doi:10.1130/0091-7613(1992)020<1095.
- Howard, A. D. (1998), Long profile development of bedrock channels: Interaction of weathering, mass wasting, bed erosion, and sediment transport, in *Rivers Over Rock: Fluvial Processes in Bedrock Channels*, vol. 107, pp. 297–319.
- Howard, A. D. (1997), Badland Morphology and Evolution: Interpretation Using a Simulation Model, *Earth Surf. Process. Landforms*, 22(3), 211–227, doi:10.1002/(SICI)1096-9837(199703)22:3<211::AID-ESP749>3.0.CO;2-E.
- Hurst, M. D., S. M. Mudd, R. Walcott, M. Attal, and K. Yoo (2012), Using hilltop curvature to derive the spatial distribution of erosion rates, *J. Geophys. Res.*, 117(F2), F02017, doi:10.1029/2011JF002057.
- Hurst, M. D., S. M. Mudd, M. Attal, and G. Hilley (2013a), Hillslopes record the growth and decay of landscapes., *Science*, 341(6148), 868–71, doi:10.1126/science.1241791.
- Hurst, M. D., S. M. Mudd, K. Yoo, M. Attal, and R. Walcott (2013b), Influence of lithology on hillslope morphology and response to tectonic forcing in the northern Sierra Nevada of California, *J. Geophys. Res. Earth Surf.*, 118(2), 832–851, doi:10.1002/jgrf.20049.
- Hutcheon, I. (1983), Diagenesis 3. Aspects of the Diagenesis of Coarse-Grained Siliciclastic Rocks, *Geosci. Canada*, 10(1), 4–14.

- Kasahara, T., and S. M. Wondzell (2003), Geomorphic controls on hyporheic exchange flow in mountain streams, *Water Resour. Res.*, 39(1), 1005, doi: 10.1029/2002WR001386.
- Kelsey, H. M., D. C. Engebretson, C. E. Mitchell, and R. L. Ticknor (1994), Topographic form of the Coast Ranges of the Cascadia margin in relation to coastal uplift rates and plate subduction, *J. Geophys. Res.*, 99(B6), 255,12212–12245.
- Kirby, E., and K. Whipple (2001), Quantifying differential rock-uplift rates via stream profile analysis, *Geology*, 29(5), 415–418.
- Kirby, E., and K. X. Whipple (2012), Expression of active tectonics in erosional landscapes, *J. Struct. Geol.*, 44, 54–75, doi:10.1016/j.jsg.2012.07.009.
- Kobor, J., and J. Roering (2004), Systematic variation of bedrock channel gradients in the central Oregon Coast Range: implications for rock uplift and shallow landsliding, *Geomorphology*, 62(3), 239–256.
- Korup, O., and F. Schlunegger (2009), Rock-type control on erosion-induced uplift, eastern Swiss Alps, *Earth Planet. Sci. Lett.*, 278(3-4), 278–285, doi:10.1016/j.epsl.2008.12.012.
- Lague, D., and P. Davy (2003), Constraints on the long-term colluvial erosion law by analyzing slope-area relationships at various tectonic uplift rates in the Siwaliks Hills (Nepal), *J. Geophys. Res. Solid Earth*, 108(B2), 2129, doi:10.1029/2002JB001893.
- Lovell, J. (1969), Tye formation; a study of proximality in turbidites, *J. Sediment. Res.*, 39(3), 935–953.
- Lovell, J., and J. Rogers (1969), Tye Formation: Undeformed turbidites and their lateral equivalents: Mineralogy and paleogeography, *Geol. Soc. Am. Bull.*, 80(1), 9–22.
- Lutz, H. (1960), Movement of rocks by uprooting of forest trees, *Am. J. Sci.*, 258(10), 752–756.
- Marshall, J. A., M. Attal, L. S. Sklar, C. S. Riebe, M. D. Hurst, S. M. Mudd, and K. Yoo (2009), The Effect of Erosion Rate on Hillslope Rock Fragment Production: Implications for Supply of Bedload Material to Channels, *Eos Trans. AGU*, 2009 (52), Fall Meet. Suppl., Abstract EP51B-0594.
- Matthes-Sears, U., and D. Larson (1995), Rooting characteristics of trees in rock: a study of *Thuja occidentalis* on cliff faces, *Int. J. Plant Sci.*, 156(5), 679–686.
- May, C., J. Roering, L. Eaton, and K. Burnett (2013), Controls on valley width in mountainous landscapes: The role of landsliding and implications for salmonid habitat, *Geology*, doi:10.1130/g33979.1.

- Montgomery, D. R. (2001), Slope distributions, threshold hillslopes, and steady-state topography, *Am. J. Sci.*, 301(4-5), 432–454, doi:10.2475/ajs.301.4-5.432.
- Montgomery, D. R., and M. T. Brandon (2002), Topographic controls on erosion rates in tectonically active mountain ranges, *Earth Planet. Sci. Lett.*, 201(3-4), 481–489, doi:10.1016/S0012-821X(02)00725-2.
- Montgomery, D. R., and E. Foufoula-Georgiou (1993), Channel network source representation using digital elevation models, *Water Resour. Res.*, 29(12), 3925–3934, doi:10.1029/93WR02463.
- Moore, J. R., J. W. Sanders, W. E. Dietrich, and S. D. Glaser (2009), Influence of rock mass strength on the erosion rate of alpine cliffs, *Earth Surf. Process. Landforms*, 34(10), 1339–1352, doi:10.1002/esp.1821.
- Mudd, S. M., M. Attal, D. T. Milodowski, S. W. D. Grieve, and D. A. Valters (2014), A statistical framework to quantify spatial variation in channel gradients using the integral method of channel profile analysis, *J. Geophys. Res. Earth Surf.*, 119(2), 138–152, doi:10.1002/2013JF002981.
- Naiman, R., and R. Bilby (Eds.) (1998), *River ecology and management: lessons from the Pacific coastal ecoregion*, Springer Verlag, New York.
- Orr, E. L., W. N. Orr, and E. M. Baldwin (1992), *Geology of Oregon*, 254 pp. Kendall/Hunt, Dubuque, Iowa.
- Ouimet, W. B., K. X. Whipple, and D. E. Granger (2009), Beyond threshold hillslopes: Channel adjustment to base-level fall in tectonically active mountain ranges, *Geology*, 37(7), 579–582, doi:10.1130/G30013A.1.
- Perron, J. T., J. W. Kirchner, and W. E. Dietrich (2008), Spectral signatures of characteristic spatial scales and nonfractal structure in landscapes, *J. Geophys. Res.*, 113(F4), F04003, doi:10.1029/2007JF000866.
- Perron, J. T., J. W. Kirchner, and W. E. Dietrich (2009), Formation of evenly spaced ridges and valleys, *Nature*, 460(7254), 502–505, doi:10.1038/nature08174.
- Perron, J., and L. Royden (2013), An integral approach to bedrock river profile analysis, *Earth Surf. Process. Landforms*, 38: 570–576. doi: 10.1002/esp.3302.
- Priestley, M. B. (1981), *Spectral analysis and time series. Volume 1: Univariate series*, Academic Press, New York.
- Rayner, J. (1972), The application of harmonic and spectral analysis to the study of terrain, in *Spatial analysis in Geomorphology*, edited by R. J. Chorley, pp. 283–302, Methuen, London.

- Reneau, S. L., and W. E. Dietrich (1991), Erosion rates in the southern Oregon coast range: Evidence for an equilibrium between hillslope erosion and sediment yield, *Earth Surf. Process. Landforms*, *16*, 307–322, doi:10.1002/esp.3290160405.
- Richards, M., M. Bowman, and H. Reading (1998), Submarine-fan systems I: characterization and stratigraphic prediction, *Mar. Pet. Geol.*, *15*, 689–717, doi:10.1016/S0264-8172(98)00036-1.
- Roering, J. J. (2008), How well can hillslope evolution models “explain” topography? Simulating soil transport and production with high-resolution topographic data, *Geol. Soc. Am. Bull.*, *120*, 1248–1262, doi:10.1130/B26283.1.
- Roering, J. J., J. W. Kirchner, and W. E. Dietrich (1999), Evidence for nonlinear, diffusive sediment transport on hillslopes and implications for landscape morphology, *Water Resour. Res.*, **35**, 853, doi:10.1029/1998WR900090.
- Roering, J. J., J. W. Kirchner, L. S. Sklar, and W. E. Dietrich (2001), Hillslope evolution by nonlinear creep and landsliding: An experimental study, *Geology*, *29*(2), 143–146, doi:10.1130/0091-7613(2001)029<0143:hebnca>2.0.co;2
- Roering, J. J., J. W. Kirchner, and W. E. Dietrich (2005), Characterizing structural and lithologic controls on deep-seated landsliding: Implications for topographic relief and landscape evolution in the Oregon Coast Range, USA, *Geol. Soc. Am. Bull.*, **117**, 654-668 doi:10.1130/B25567.1.
- Roering, J. J., J. T. Perron, and J. W. Kirchner (2007), Functional relationships between denudation and hillslope form and relief, *Earth Planet. Sci. Lett.*, *264*, 245–258, doi:10.1016/j.epsl.2007.09.035.
- Roering, J. J., J. Marshall, A. M. Booth, M. Mort, and Q. Jin (2010), Evidence for biotic controls on topography and soil production, *Earth Planet. Sci. Lett.*, *298*(1-2), 183–190, doi:10.1016/j.epsl.2010.07.040.
- Rogers, J. (1969), Tyee Formation: Undeformed Turbidites and Their Lateral Equivalents: Mineralogy and Paleogeography: Discussion, *Geol. Soc. Am. Bull.*, *80*(10), 2129, doi:10.1130/0016-7606(1969)80[2129:TFUTAT]2.0.CO;2.
- Rogers, J., and K. Richardson (1964), Thorium and uranium contents of some sandstones, *Geochim. Cosmochim. Acta*, *28*(12), 2005–2011.
- Ryu, I., and A. R. Niem (1999), Sandstone Diagenesis, Reservoir Potential, and Sequence Stratigraphy of the Eocene Tyee Basin, Oregon, *SEPM J. Sediment. Res.*, *69*(1), 384–393, doi:10.1306/D42689F5-2B26-11D7-8648000102C1865D.
- Schmidt, K. M., and D. R. Montgomery (1995), Limits to Relief, *Science* (80-.), *270*, 617–620, doi:10.1126/science.270.5236.617.

- Seidl, M., and W. Dietrich (1992), The problem of channel erosion into bedrock, *Catena*, 23(Supplement), 101–104.
- Selby, M. (1993), *Hillslope materials and processes*, 2nd ed., Oxford Univ. Press, Oxford.
- Simpson, R. W. R., and A. Cox (1977), Paleomagnetic evidence for tectonic rotation of the Oregon Coast Range, *Geology*, doi:10.1130/0091-7613(1977)5<585.
- Sklar, L. S., and W. E. Dietrich (1998), River longitudinal profiles and bedrock incision models: Stream power and the influence of sediment supply, in *Rivers Over Rock: Fluvial Processes in Bedrock Channels*, vol. 107, pp. 237–260.
- Sklar, L. S., and W. E. Dietrich (2001), Sediment and rock strength controls on river incision into bedrock, *Geology*, 29(12), 1087–1090, doi: 10.1130/0091-7613(2001)029<1087:SARSCO>2.0.CO;2.
- Sklar, L. S., and W. E. Dietrich (2004), A mechanistic model for river incision into bedrock by saltating bed load, *Water Resour. Res.*, 40(6), W06301, doi: 10.1029/2003WR002496.
- Sklar, L. S., and W. E. Dietrich (2006), The role of sediment in controlling steady-state bedrock channel slope: Implications of the saltation–abrasion incision model, *Geomorphology*, 82, 58–83, doi:10.1016/j.geomorph.2005.08.019.
- Snively, P. D., H. C. Wagner, and N. S. MacLeod (1964), Rhythmic-bedded eugeosynclinal deposits of the Tyee formation, Oregon Coast Range, *Kansas Geol. Surv. Bull.*, 169, 461–480.
- Snyder, N. P., K. X. Whipple, G. E. Tucker, and D. J. Merritts (2000), Landscape response to tectonic forcing: Digital elevation model analysis of stream profiles in the Mendocino triple junction region, northern California, *Geol. Soc. Am. Bull.*, 112, 1250–1263, doi:10.1130/0016-7606(2000)112<1250:LRTTFD>2.0.CO;2.
- Stock, J., and W. E. Dietrich (2003), Valley incision by debris flows: Evidence of a topographic signature, *Water Resour. Res.*, 39(4), doi:10.1029/2001WR001057.
- Stock, J. D., D. R. Montgomery, B. D. Collins, W. E. Dietrich, and L. Sklar (2005), Field measurements of incision rates following bedrock exposure: Implications for process controls on the long profiles of valleys cut by rivers and debris flows, *Geol. Soc. Am. Bull.*, 117(1-2), 174, doi:10.1130/B25560.1.
- Stock, J. D., and W. E. Dietrich (2006), Erosion of steepland valleys by debris flows, *Geol. Soc. Am. Bull.*, 118(9-10), 1125–1148, doi:10.1130/B25902.1.

- Sweeney, K. E., J. J. Roering, P. Almond, and T. Reckling (2012), How steady are steady-state landscapes? Using visible-near-infrared soil spectroscopy to quantify erosional variability, *Geology*, *40*(9), 807–810, doi:10.1130/G33167.1.
- VanLaningham, S. (2006), The effects of rock uplift and rock resistance on river morphology in a subduction zone forearc, Oregon, USA, *Earth Surf. Process. Landforms*, *31*(10), 1257–1279, doi:10.1002/esp.
- Vutukuri, V. S., R., D. Lama, and S. S. Saluja (1974), Handbook on mechanical properties of rocks, Testing techniques and results. Vol. 1, Series on Rock and Soil Mechanics, Bay Village, Ohio, *Trans. Tech Publishers*, p. 105-115.
- Weaver, C. E. (2000), Origin and geologic implications of the palygorskite of the SE United States, in *Palygorskite-sepiolite: occurrences, genesis and uses*, edited by A. Singer and E. Galan, Elsevier B.V.
- Wells, R. E., and P. L. Heller (1988), The relative contribution of accretion, shear, and extension to Cenozoic tectonic rotation in the Pacific Northwest, *Geol. Soc. Am. Bull.*, *100*, 325–338, doi:10.1130/0016-7606(1988)100<0325:TRCOAS>2.3.CO;2.
- Wheatcroft, R. A., and C. K. Sommerfield (2005), River sediment flux and shelf sediment accumulation rates on the Pacific Northwest margin, *Cont. Shelf Res.*, *25*(3), 311–332, doi:10.1016/j.csr.2004.10.001.
- Whipple, K., C. Wobus, B. Crosby, E. Kirby, and D. Sheehan (2007), New tools for quantitative geomorphology: extraction and interpretation of stream profiles from digital topographic data, *GSA Short Course*, 506.
- Whipple, K. X. (2004), Bedrock rivers and the geomorphology of active orogens, *Annu. Rev. Earth Planet. Sci.*, *32*, 151–185, doi:10.1146/annurev.earth.32.101802.120356.
- Whipple, K. X., E. Kirby, and S. H. Brocklehurst (1999), Geomorphic limits to climate-induced increases in topographic relief, *Nature*, *401*, 39–43, doi:10.1038/43375.
- Willett, S., S. McCoy, J. Perron, L. Goren, and C. Chen (2014), Dynamic Reorganization of River Basins, *Science*, **343** (6175), doi: 10.1126/science.1248765.
- Wobus, C., K. Whipple, E. Kirby, N. Snyder, J. Johnson, K. Spyropolou, B. Crosby, and D. Sheehan (2006), Tectonics from topography: Procedures, promise, and pitfalls, in *Tectonics, Climate, and Landscape Evolution*, edited by S.D. Willett et al., Penrose Cof.Ser., *Spec. Pap. Geol. Soc. Am.*, **398**, 55-74, doi: 10.1130/2006.2398(04).
- Wood, J. (1996), The geomorphological characterisation of digital elevation models, Ph.D. diss., University of Leicester.

Yatsu, E. (1971), Landform material science, rock control in geomorphology, in *Proceedings, 1st Guelph Symposium on Geomorphology*, vol. 1, pp. 49–73, University of Guelph Geographical Publication.

Chapter III

1. Raymo ME, Ruddiman WF (1992) Tectonic forcing of late Cenozoic climate. *Nature* 359(6391):117–122.
2. West JA, Galy A, Bickle M (2005) Tectonic and climatic controls on silicate weathering. *Earth Planet Sci Lett* 235(1-2):211–228.
3. Champagnac J-D, Valla PG, Herman F (2014) Late-Cenozoic relief evolution under evolving climate: A review. *Tectonophysics* 614:44–65.
4. Dietrich WE, et al. (2003) Geomorphic transport laws for predicting landscape form and dynamics. *Predictions in Geomorphology*, eds Wilcock PR, Iverson RM (American Geophysical Union, Washington, D. C.), pp 103–132. Geophysica.
5. Zhang P, Molnar P, Downs WR (2001) Increased sedimentation rates and grain sizes 2-4 Myr ago due to the influence of climate change on erosion rates. *Nature* 410(6831):891–7.
6. Bull W (1991) *Geomorphic Responses to Climatic Change* (Oxford Univ. Press, New York).
7. Huntington E, Schuchert C, Douglass AE, Kullmer CJ (1914) *The Climatic Factor as Illustrated in Arid America* (Carnegie Institution of Washington).
8. Hancock GS, Anderson RS (2002) Numerical modeling of fluvial strath-terrace formation in response to oscillating climate. *Geol Soc Am Bull* 114(9):1131–1142.
9. Finnegan NJ, Schumer R, Finnegan S (2014) A signature of transience in bedrock river incision rates over timescales of 10(4)-10(7) years. *Nature* 505(7483):391–4.
10. Matsuoka N (2001) Solifluction rates, processes and landforms: a global review. *Earth-Science Rev* 55(1-2):107–134.
11. Matsuoka N, Murton J (2008) Frost weathering: recent advances and future directions. *Permafrost Periglacial Process* 19(2):195–210.
12. Von Blanckenburg F (2005) The control mechanisms of erosion and weathering at basin scale from cosmogenic nuclides in river sediment. *Earth Planet Sci Lett* 237(3-4):462–479.

13. Worona MA, Whitlock C (1995) Late Quaternary vegetation and climate history near Little Lake, central Coast Range, Oregon. *Geol Soc Am Bull* 107(7):867–876.
14. Grigg LD, Whitlock C, Dean WE (2001) Evidence for Millennial-Scale Climate Change During Marine Isotope Stages 2 and 3 at Little Lake, Western Oregon, U.S.A. *Quat Res* 56(1):10–22.
15. Schaller M, Ehlers TA (2006) Limits to quantifying climate driven changes in denudation rates with cosmogenic radionuclides. *Earth Planet Sci Lett* 248(1-2):153–167.
16. Alexander RR, Shearer RC, Shepperd WD (1990) Silvics of North America. Volume 1. Conifers. eds Burns RM, Honkala BH (Technical C (United States Department of Agriculture, Forest Service, Washington, D. C.), p 675.
17. Roering JJ, Kirchner JW, Dietrich WE (2001) Hillslope evolution by nonlinear, slope-dependent transport: Steady state morphology and equilibrium adjustment timescales. *J Geophys Res* 106(B8):16499.
18. Roering JJ, Perron JT, Kirchner JW (2007) Functional relationships between denudation and hillslope form and relief. *Earth Planet Sci Lett* 264:245–258.
19. Walder J, Hallet B (1985) A theoretical model of the fracture of rock during freezing. *Geol Soc Am Bull* 96(3):336–346.
20. Anderson RS, Anderson SP, Tucker GE (2013) Rock damage and regolith transport by frost: an example of climate modulation of the geomorphology of the critical zone. *Earth Surf Process Landforms* 38(3):299–316.
21. Hales TC, Roering JJ (2007) Climatic controls on frost cracking and implications for the evolution of bedrock landscapes. *J Geophys Res* 112(F2):F02033.
22. Dash J, Rempel A, Wettlaufer J (2006) The physics of premelted ice and its geophysical consequences. *Rev Mod Phys* 78(3):695–741.
23. Vlahou I, Worster MG (2015) Freeze fracturing of elastic porous media: a mathematical model. *Proc R Soc A Math Phys Eng Sci* 471(2175):20140741–20140741.
24. Delunel R, van der Beek PA, Carcaillet J, Bourlès DL, Valla PG (2010) Frost-cracking control on catchment denudation rates: Insights from in situ produced ¹⁰Be concentrations in stream sediments (Ecrins–Pelvoux massif, French Western Alps). *Earth Planet Sci Lett* 293(1-2):72–83.
25. Bloomfield P (2000) *Fourier Analysis of Time Series: An Introduction* (John Wiley & Sons, New York). Second.

26. Carslaw HS, Jaeger JC (1959) Conduction of heat in solids. *Oxford Clarendon Press*.
27. Braconnot P, et al. (2012) Evaluation of climate models using palaeoclimatic data. *Nat Clim Chang* 2(6):417–424.
28. Harrison SP, et al. (2013) Climate model benchmarking with glacial and mid-Holocene climates. *Clim Dyn* 43(3-4):671–688.
29. Izumi K, Bartlein PJ, Harrison SP (2013) Consistent large-scale temperature responses in warm and cold climates. *Geophys Res Lett* 40(9):1817–1823.
30. Herman F, et al. (2013) Worldwide acceleration of mountain erosion under a cooling climate. *Nature* 504(7480):423–6.
31. Hales TC, Roering JJ (2005) Climate-controlled variations in scree production, Southern Alps, New Zealand. *Geology* 33(9):701.
32. Blaauw M (2010) Methods and code for “classical” age-modelling of radiocarbon sequences. *Quat Geochronol* 5(5):512–518.
33. Nishiizumi K, et al. (2007) Absolute calibration of ^{10}Be AMS standards. *Nucl Instruments Methods Phys Res Sect B Beam Interact with Mater Atoms* 258(2):403–413.
34. Hales TC, Roering JJ (2009) A frost “buzzsaw” mechanism for erosion of the eastern Southern Alps, New Zealand. *Geomorphology* 107(3-4):241–253.
35. Harris C, et al. (2008) Solifluction processes on permafrost and non-permafrost slopes: results of a large-scale laboratory simulation. *Permafr Periglac Process* 19(4):359–378.
36. Praskievicz S, Bartlein P (2014) Hydrologic modeling using elevationally adjusted NARR and NARCCAP regional climate-model simulations: Tucannon River, Washington. *J Hydrol* 517:803–814.
37. Wang T, Hamann A, Spittlehouse DL, Murdock TQ (2012) ClimateWNA—High-Resolution Spatial Climate Data for Western North America. *J Appl Meteorol Climatol* 51(1):16–29.

Chapter IV

Ahnert, F., 1976, Brief description of a comprehensive three-dimensional process-response model of landform development: *Z. Geomorphol. Suppl.*, v. 25, p. 29–49.

- Ahnert, F., 1994, Equilibrium, scale and inheritance in geomorphology: *Geomorphology*, v. 11, p. 125–140, doi: 10.1016/0169-555X(94)90077-9.
- Alexander, R.R., Shearer, R.C., and Shepperd, W.D., 1990, *Silvics of North America. Volume 1. Conifers*, in Burns, R.M. and Honkala, B.H. (Technical C. eds., Washington, D. C., United States Department of Agriculture, Forest Service, p. 675.
- Anderson, R.S., 1998, Near-Surface Thermal Profiles in Alpine Bedrock: Implications for the Frost Weathering of Rock: *Arctic and Alpine Research*, v. 30, p. 362–372, doi: 10.2307/1552008.
- Anderson, R.S., Anderson, S.P., and Tucker, G.E., 2013, Rock damage and regolith transport by frost: an example of climate modulation of the geomorphology of the critical zone: *Earth Surface Processes and Landforms*, v. 38, p. 299–316, doi: 10.1002/esp.3330.
- Anderson, S.P., Dietrich, W.E., and Brimhall, G.H., 2002, Weathering profiles , mass-balance analysis , and rates of solute loss : Linkages between weathering and erosion in a small, steep catchment: *Geological Society of America Bulletin*, v. 114, p. 1143–1158, doi: 10.1130/0016-7606(2002)114<1143.
- Balco, G., Finnegan, N., Gendaszek, a., Stone, J.O.H., and Thompson, N., 2013, Erosional response to northward-propagating crustal thickening in the coastal ranges of the U.S. Pacific Northwest: *American Journal of Science*, v. 313, p. 790–806, doi: 10.2475/11.2013.01.
- Balco, G., and Stone, J.O.H., 2005, Measuring middle Pleistocene erosion rates with cosmic-ray-produced nuclides in buried alluvial sediment, Fisher Valley, southeastern Utah: *Earth Surface Processes and Landforms*, v. 30, p. 1051–1067, doi: 10.1002/esp.1262.
- Balco, G., Stone, J.O., Lifton, N.A., and Dunai, T.J., 2008, A complete and easily accessible means of calculating surface exposure ages or erosion rates from ^{10}Be and ^{26}Al measurements: *Quaternary Geochronology*, v. 3, p. 174–195, doi: 10.1016/j.quageo.2007.12.001.
- Barry, R.G., 2013, *Palaeoclimatology, climate system processes and the geomorphic record: Process and Form in Geomorphology*,.
- Beschta, R.L., 1978, Long-term patterns of sediment production following road construction and logging in the Oregon Coast Range: *Water Resources Research*, v. 14, p. 1011–1016, doi: 10.1029/WR014i006p01011.
- Bevington, P.R., and Robinson, D.K., 2003, *Data reduction and error analysis*: New York, 366 p.

- Bierman, P., Clapp, E., Nichols, K., Gillespie, A., and Caffee, M., 2001, Using cosmogenic nuclide measurements in sediments to understand background rates of erosion and sediment transport: *Landscape Erosion and Evolution Modelling*: New York, Kluwer, p. 89–116.
- Blaauw, M., 2010, Methods and code for “classical” age-modelling of radiocarbon sequences: *Quaternary Geochronology*, v. 5, p. 512–518, doi: 10.1016/j.quageo.2010.01.002.
- Von Blanckenburg, F., 2005, The control mechanisms of erosion and weathering at basin scale from cosmogenic nuclides in river sediment: *Earth and Planetary Science Letters*, v. 237, p. 462–479, doi: 10.1016/j.epsl.2005.06.030.
- Blechs Schmidt, I., Matter, A., Preusser, F., and Rieke-Zapp, D., 2009, Monsoon triggered formation of Quaternary alluvial megafans in the interior of Oman: *Geomorphology*, v. 110, p. 128–139, doi: 10.1016/j.geomorph.2009.04.002.
- Bloomfield, P., 2000, *Fourier Analysis of Time Series: An Introduction*: New York, John Wiley & Sons, 288 p.
- Braconnot, P., Harrison, S.P., Kageyama, M., Bartlein, P.J., Masson-Delmotte, V., Abe-Ouchi, A., Otto-Bliesner, B., and Zhao, Y., 2012, Evaluation of climate models using palaeoclimatic data: *Nature Climate Change*, v. 2, p. 417–424, doi: 10.1038/nclimate1456.
- Bryan, K., 1940, *Erosion in the valleys of the Southwest*: publisher not identified.
- Bryan, K., 1928, Historic Evidence on Changes in the Channel of Rio Puerco, a Tributary of the Rio Grande in New Mexico: *The Journal of Geology*, v. 36, p. 265–282, doi: 10.2307/30060528.
- Bryan, K., 1950, The place of geomorphology in the geographic sciences: *Annals of the Association of American Geographers*, v. 40, p. 196–208.
- Bull, W., 1991, *Geomorphic Responses to Climatic Change*: New York, Oxford Univ. Press.
- Canadell, J., Jackson, R.B., Ehleringer, J.B., Mooney, H.A., Sala, O.E., and Schulze, E.-D., 1996, Maximum rooting depth of vegetation types at the global scale: *Oecologia*, v. 108, p. 583–595, doi: 10.1007/BF00329030.
- Carslaw, H.S., and Jaeger, J.C., 1959, *Conduction of heat in solids*: Oxford: Clarendon Press,.
- Champagnac, J.-D., Valla, P.G., and Herman, F., 2014, Late-Cenozoic relief evolution under evolving climate: A review: *Tectonophysics*, v. 614, p. 44–65, doi: 10.1016/j.tecto.2013.11.037.

- Chan, M.A., and Dott, R.H.J., 1986, Depositional facies and progradational sequences in Eocene wave-dominated deltaic complexes, southwestern Oregon: *Am. Assoc. Pet. Geol., Bull.*; (United States), v. 70:4.
- Chorley, R.J., Schumm, S.A., and Sugden, D.E., 1984, *Geomorphology*: New York: New York, Methuen & Co, p. 605.
- Clynne, M.A., Calvert, A.T., Wolfe, E.W., Evarts, R.C., Fleck, R.J., and Lanphere, M.A., 2008, The Pleistocene eruptive history of Mount St. Helens, Washington, from 300,000 to 12,800 years before present: Chapter 28 in *A volcano rekindled: the renewed eruption of Mount St. Helens, 2004-2006*: Professional Paper, p. 593–627.
- Committee on Basic Research Opportunities in the Earth Sciences, Board on Earth Sciences and Resources, N.R.C., 2001, *Basic Research Opportunities in Earth Science*: Washington, D. C., The National Academies Press.
- Cox, N., 1980, On the relationship between bedrock lowering and regolith thickness: *Earth Surface Processes*, v. 5, p. 271–274.
- Crandell, D.R., 1987, Deposits of pre-1980 pyroclastic flows and lahars from Mount St. Helens Volcano, Washington: Professional Paper,.
- Davis, W.M., 1899, The geographical cycle: *The Geographical Journal*, v. 14, p. 481–504.
- Delunel, R., van der Beek, P.A., Carcaillet, J., Bourlès, D.L., and Valla, P.G., 2010, Frost-cracking control on catchment denudation rates: Insights from in situ produced ¹⁰Be concentrations in stream sediments (Ecrins–Pelvoux massif, French Western Alps): *Earth and Planetary Science Letters*, v. 293, p. 72–83, doi: 10.1016/j.epsl.2010.02.020.
- Dietrich, W.E., Bellugi, D.G., Sklar, L.S., Stock, J.D., Heimsath, A.M., and Roering, J.J., 2003, Geomorphic transport laws for predicting landscape form and dynamics, *in* Wilcock, P.R. and Iverson, R.M. eds., *Predictions in Geomorphology*, Washington, D. C., American Geophysical Union, p. 103–132.
- Dietrich, W.E., and Dunne, T., 1978, Sediment budget for a small catchment in mountainous terrain: *Z. Geomorph. N.F.*, v. 29, p. 191–206, doi: 10.1007/s10069-002-0008-0.
- Dietrich, W.E., and Perron, J.T., 2006, The search for a topographic signature of life.: *Nature*, v. 439, p. 411–8, doi: 10.1038/nature04452.
- Dietrich, W.E., Reiss, R., Hsu, M., and Montgomery, D.R., 1995, A process-based model for colluvial soil depth and shallow landsliding using digital elevation data: *Hydrological Processes*, v. 9, p. 383–400.

- French, H.M., 2013, *The periglacial environment*: John Wiley & Sons, 458 p.
- Furbish, D., and Fagherazzi, S., 2001, Stability of creeping soil and implications for hillslope evolution: *Water Resources Research*, v. 37, p. 2607–2618.
- Gabet, E.J., and Mudd, S.M., 2010, Bedrock erosion by root fracture and tree throw: A coupled biogeomorphic model to explore the humped soil production function and the persistence of hillslope soils: *Journal of Geophysical Research: Earth Surface*, v. 115, doi: 10.1029/2009JF001526.
- Gabet, E., Reichman, O., and Seabloom, E., 2003, The effects of bioturbation on soil processes and sediment transport: *Annual Review of Earth and Planetary Sciences*, v. 31, p. 249–273.
- Gilbert, G.K., 1890, *Lake Bonneville*: U.S. Government Printing Office, 438 p.
- Gilbert, G.K., 1877, *Report on the geology of the Henry Mountains: US Geographical and Geological Survey of the Rocky Mountain Region*.
- Granger, D.E., and Muzikar, P.F., 2001, Dating sediment burial with in situ-produced cosmogenic nuclides: theory, techniques, and limitations: *Earth and Planetary Science Letters*, v. 188, p. 269–281, doi: 10.1016/S0012-821X(01)00309-0.
- Granger, D.E., and Riebe, C.S., 2014, *Cosmogenic Nuclides in Weathering and Erosion*, in Drever, J.I. ed., *Treatise on Geochemistry*, London, Elsevier, p. 401–436.
- Granger, D.E., and Schaller, M., 2014, *Cosmogenic Nuclides and Erosion at the Watershed Scale: Elements*, v. 10, p. 369–373, doi: 10.2113/gselements.10.5.369.
- Grigg, L.D., and Whitlock, C., 1998, Late-Glacial Vegetation and Climate Change in Western Oregon: *Quaternary Research*, v. 49, p. 287–298, doi: 10.1006/qres.1998.1966.
- Grigg, L.D., and Whitlock, C., 2002, Patterns and causes of millennial-scale climate change in the Pacific Northwest during Marine Isotope Stages 2 and 3: *Quaternary Science Reviews*, v. 21, p. 2067–2083, doi: 10.1016/S0277-3791(02)00017-3.
- Grigg, L.D., Whitlock, C., and Dean, W.E., 2001, Evidence for Millennial-Scale Climate Change During Marine Isotope Stages 2 and 3 at Little Lake, Western Oregon, U.S.A.: *Quaternary Research*, v. 56, p. 10–22, doi: 10.1006/qres.2001.2246.
- Hack, J.T., 1975, *Dynamic equilibrium and landscape evolution: Theories of landform development*.
- Hahm, W., and Riebe, C., 2014, Bedrock composition regulates mountain ecosystems and landscape evolution: *Proceedings of the National Academy of Sciences*, v. 111, p. 3338–3343, doi: 10.1073/pnas.1315667111.

- Hales, T.C., and Roering, J.J., 2007, Climatic controls on frost cracking and implications for the evolution of bedrock landscapes: *Journal of Geophysical Research*, v. 112, p. F02033, doi: 10.1029/2006JF000616.
- Harris, C., Kern-Luetsch, M., Murton, J., Font, M., Davies, M., and Smith, F., 2008, Solifluction processes on permafrost and non-permafrost slopes: results of a large-scale laboratory simulation: *Permafrost and Periglacial Processes*, v. 19, p. 359–378, doi: 10.1002/ppp.630.
- Harrison, S.P., Bartlein, P.J., Brewer, S., Prentice, I.C., Boyd, M., Hessler, I., Holmgren, K., Izumi, K., and Willis, K., 2013, Climate model benchmarking with glacial and mid-Holocene climates: *Climate Dynamics*, v. 43, p. 671–688, doi: 10.1007/s00382-013-1922-6.
- Heimsath, A.M., 2006, Eroding the land: steady-state and stochastic rates and processes through a cosmogenic lens: *Geological Society of America Special Papers*, v. 415, p. 111–129.
- Heimsath, A.M., Dietrich, W.E., Nishiizumi, K., and Finkel, R.C., 2001, Stochastic processes of soil production and transport: erosion rates, topographic variation and cosmogenic nuclides in the Oregon Coast Range: *Earth Surface Processes and Landforms*, v. 26, p. 531–552, doi: 10.1002/esp.209.
- Heimsath, A.M., Dietrich, W.E., Nishiizumi, K., and Finkel, R.C., 1997, The soil production function and landscape equilibrium: *Nature*, v. 388, p. 21–24, doi: 10.1144/SP312.8.
- Heimsath, A.M., E. Dietrich, W., Nishiizumi, K., and Finkel, R.C., 1999, Cosmogenic nuclides, topography, and the spatial variation of soil depth: *Geomorphology*, v. 27, p. 151–172, doi: 10.1016/S0169-555X(98)00095-6.
- Heller, P.L., and Dickinson, W.R., 1985, Submarine ramp facies model for delta-fed, sand-rich turbidite systems: *AAPG Bulletin*, v. 69, p. 960.
- Hendy, I., Kennett, J., Roark, E., and Ingram, B., 2002, Apparent synchronicity of submillennial scale climate events between Greenland and Santa Barbara Basin, California from 30–10ka: *Quaternary Science Reviews*, v. 21, p. 1167–1184, doi: 10.1016/S0277-3791(01)00138-X.
- Herman, F., Seward, D., Valla, P.G., Carter, A., Kohn, B., Willett, S.D., and Ehlers, T.A., 2013, Worldwide acceleration of mountain erosion under a cooling climate.: *Nature*, v. 504, p. 423–6, doi: 10.1038/nature12877.
- Hudiburg, T., Law, B., Turner, D.P., Campbell, J., Donato, D., and Duane, M., 2009, Carbon dynamics of Oregon and Northern California forests and potential land-based carbon storage: *Ecological Applications*, v. 19, p. 163–180, doi: 10.1890/07-2006.1.

- Hughes, M.W., Almond, P.C., and Roering, J.J., 2009, Increased sediment transport via bioturbation at the last glacial-interglacial transition: *Geology*, v. 37, p. 919–922, doi: 10.1130/G30159A.1.
- Humphreys, G., and Wilkinson, M., 2007, The soil production function: a brief history and its rediscovery: *Geoderma*, v. 139, p. 73–78.
- Huntington, E., Schuchert, C., Douglass, A.E., and Kullmer, C.J., 1914, *The Climatic Factor as Illustrated in Arid America*: Carnegie Institution of Washington, 341 p.
- Izumi, K., Bartlein, P.J., and Harrison, S.P., 2013, Consistent large-scale temperature responses in warm and cold climates: *Geophysical Research Letters*, v. 40, p. 1817–1823, doi: 10.1002/grl.50350.
- Jackson, R., Canadell, J., Ehleringer, J., Mooney, H., Sala, O., and ED, S., 1996, A global analysis of root distributions for terrestrial biomes: *Oecologia*, v. 108, p. 389–411.
- Jerolmack, D.J., and Paola, C., 2010, Shredding of environmental signals by sediment transport: *Geophysical Research Letters*, v. 37, p. n/a–n/a, doi: 10.1029/2010GL044638.
- Jouzel, J., Masson-Delmotte, V., Cattani, O., Dreyfus, G., Falourd, S., Hoffmann, G., Minster, B., Nouet, J., Barnola, J.M., Chappellaz, J., Fischer, H., Gallet, J.C., Johnsen, S., Leuenberger, M., et al., 2007, Orbital and millennial Antarctic climate variability over the past 800,000 years.: *Science (New York, N.Y.)*, v. 317, p. 793–6, doi: 10.1126/science.1141038.
- Kelsey, H.M., Ticknor, R.L., Bockheim, J.G., and Mitchell, E., 1996, Quaternary upper plate deformation in coastal Oregon: *Geological Society of America Bulletin*, v. 108, p. 843–860, doi: 10.1130/0016-7606(1996)108.
- Kirchner, J.W., Finkel, R.C., Riebe, C.S., Granger, D.E., Clayton, J.L., King, J.G., and Megahan, W.F., 2001, Mountain erosion over 10 yr, 10 k.y., and 10 m.y. time scales: *Geology*, v. 29, p. 591–594, doi: 10.1130/0091-7613(2001)029.
- Kirkby, M., 1995, A Model for Variations in Gelifluction Rates with Temperature and Topography: Implications for Global Change: *Geografiska Annaler. Series A, Physical Geography*, v. 77, p. 269–278.
- Kohl, C., and Nishiizumi, K., 1992, Chemical isolation of quartz for measurement of in-situ -produced cosmogenic nuclides: *Geochimica et Cosmochimica Acta*, v. 56, p. 3583–3587, doi: 10.1016/0016-7037(92)90401-4.
- Kuehn, S.C., and Negrini, R.M., 2010, A 250 k.y. record of Cascade arc pyroclastic volcanism from late Pleistocene lacustrine sediments near Summer Lake, Oregon, USA: *Geosphere*, v. 6, p. 397–429, doi: 10.1130/GES00515.1.

- Lal, D., 1991, Cosmic ray labeling of erosion surfaces: in situ nuclide production rates and erosion models: *Earth and Planetary Science Letters*, v. 104, p. 424–439, doi: 10.1016/0012-821X(91)90220-C.
- Leopold, L.B., 1976, Reversal of erosion cycle and climatic change: *Quaternary Research*, v. 6, p. 557–562, doi: 10.1016/0033-5894(76)90026-0.
- Lisiecki, L.E., and Raymo, M.E., 2005, A Pliocene-Pleistocene stack of 57 globally distributed benthic $\delta^{18}\text{O}$ records: *Paleoceanography*, v. 20, p. n/a–n/a, doi: 10.1029/2004PA001071.
- Lutz, H., 1960, Movement of rocks by uprooting of forest trees: *American Journal of Science*, v. 258, p. 752–756.
- Marshall, J.A., and Roering, J.J., 2014, Diagenetic variation in the Oregon Coast Range: Implications for rock strength, soil production, hillslope form, and landscape evolution: *Journal of Geophysical Research: Earth Surface*, v. 119, p. 1395–1417, doi: 10.1002/2013JF003004.
- Mason, J.A., and Knox, J.C., 1997, Age of colluvium indicates accelerated late Wisconsinan hillslope erosion in the Upper Mississippi Valley: *Geology*, v. 25, p. 267–270, doi: 10.1130/0091-7613(1997)025.
- Matsuoka, N., 2001, Solifluction rates, processes and landforms: a global review: *Earth-Science Reviews*, v. 55, p. 107–134, doi: 10.1016/S0012-8252(01)00057-5.
- Matsuoka, N., and Murton, J., 2008, Frost weathering: recent advances and future directions: *Permafrost and Periglacial Processes*, v. 19, p. 195–210, doi: 10.1002/ppp.620.
- McNeill, L.C., Goldfinger, C., Kulm, L.D., and Yeats, R.S., 2000, Tectonics of the Neogene Cascadia forearc basin: Investigations of a deformed late Miocene unconformity: *Geological Society of America Bulletin*, v. 112, p. 1209–1224, doi: 10.1130/0016-7606(2000)112.
- Molnar, P., 2004, Late Cenozoic Increase in Accumulation Rates of Terrestrial Sediment How Might Climate Change Have Affected Erosion Rates? *Annual Review of Earth and Planetary Sciences*, v. 32, p. 67–89, doi: 10.1146/annurev.earth.32.091003.143456.
- Montgomery, D.R., 2001, Slope distributions, threshold hillslopes, and steady-state topography: *American Journal of Science*, v. 301, p. 432–454, doi: 10.2475/ajs.301.4-5.432.
- Murray, A.S., and Wintle, A.G., 2003, The single aliquot regenerative dose protocol: potential for improvements in reliability: *Radiation Measurements*, v. 37, p. 377–381, doi: 10.1016/S1350-4487(03)00053-2.

- Nishiizumi, K., Imamura, M., Caffee, M.W., Southon, J.R., Finkel, R.C., and McAninch, J., 2007, Absolute calibration of ^{10}Be AMS standards: Nuclear Instruments and Methods in Physics Research Section B: Beam Interactions with Materials and Atoms, v. 258, p. 403–413, doi: 10.1016/j.nimb.2007.01.297.
- Orr, E.L., Orr, W.N., and Baldwin, E.M., 1992, Geology of Oregon. Kendall: Hunt, Dubuque, IA, p. 194–95.
- Owen, J.J., Amundson, R., Dietrich, W.E., Nishiizumi, K., Sutter, B., and Chong, G., 2011, The sensitivity of hillslope bedrock erosion to precipitation: Earth Surface Processes and Landforms, v. 36, p. 117–135, doi: 10.1002/esp.2083.
- Pederson, J., Smith, G., and Pazzaglia, F., 2001, Comparing the modern, Quaternary, and Neogene records of climate-controlled hillslope sedimentation in southeast Nevada: Geological Society of America Bulletin, v. 113, p. 305–319, doi: 10.1130/0016-7606(2001)113.
- Penck, A., 1910, Versuch einer Klimaklassifikation auf physio-geographischer Grundlage:.
- Phillips, J.D., 2009, Biological energy in landscape evolution: American Journal of Science, v. 309, p. 271–289, doi: 10.2475/04.2009.01.
- Reneau, S.L., and Dietrich, W.E., 1991, Erosion rates in the southern Oregon coast range: Evidence for an equilibrium between hillslope erosion and sediment yield: Earth Surface Processes and Landforms, v. 16, p. 307–322, doi: 10.1002/esp.3290160405.
- Retallack, G.J., 2008, Soils of the Past: An Introduction to Paleopedology: John Wiley & Sons, 416 p.
- Riebe, C.S., Kirchner, J.W., Granger, D.E., and Finkel, R.C., 2001a, Minimal climatic control on erosion rates in the Sierra Nevada, California: Geology, v. 29, p. 447–450, doi: 10.1130/0091-7613(2001)029.
- Riebe, C.S., Kirchner, J.W., Granger, D.E., and Finkel, R.C., 2001b, Strong tectonic and weak climatic control of long-term chemical weathering rates: Geology, v. 29, p. 511–514, doi: 10.1130/0091-7613(2001)029.
- Roering, J.J., 2008, How well can hillslope evolution models “explain” topography? Simulating soil transport and production with high-resolution topographic data: Geological Society of America Bulletin, v. 120, p. 1248–1262, doi: 10.1130/B26283.1.
- Roering, J.J., Kirchner, J.W., and Dietrich, W.E., 2005, Characterizing structural and lithologic controls on deep-seated landsliding: Implications for topographic relief

- and landscape evolution in the Oregon Coast Range, USA: *Geological Society of America Bulletin*, v. 117, p. 654, doi: 10.1130/B25567.1.
- Roering, J.J., Kirchner, J.W., and Dietrich, W.E., 1999, Evidence for nonlinear, diffusive sediment transport on hillslopes and implications for landscape morphology: *Water Resources Research*, v. 35, p. 853, doi: 10.1029/1998WR900090.
- Roering, J.J., Kirchner, J.W., Sklar, L.S., and Dietrich, W.E., 2001, Hillslope evolution by nonlinear creep and landsliding: An experimental study: *Geology*, v. 29, p. 143–146, doi: 10.1130/0091-7613(2001)029<0143:hebnca>2.0.co;2.
- Roering, J.J., Marshall, J., Booth, A.M., Mort, M., and Jin, Q., 2010, Evidence for biotic controls on topography and soil production: *Earth and Planetary Science Letters*, v. 298, p. 183–190, doi: 10.1016/j.epsl.2010.07.040.
- Roering, J.J., Perron, J.T., and Kirchner, J.W., 2007, Functional relationships between denudation and hillslope form and relief: *Earth and Planetary Science Letters*, v. 264, p. 245–258, doi: 10.1016/j.epsl.2007.09.035.
- Rogers, J., and Lovell, J., 1969, Tyee Formation: Undeformed turbidites and their lateral equivalents: *Mineralogy and paleogeography: Geological Society of America Bulletin*, v. 80, p. 9–22, doi: 10.1130/0016-7606(1969)80[2129:TFUTAT]2.0.CO;2.
- Rosenqvist, I.T., 1970, Formation of vivianite in holocene clay sediments: *Lithos*, v. 3, p. 327–334, doi: 10.1016/0024-4937(70)90039-3.
- Runyon, J., Waring, R.H., Goward, S.N., and Welles, J.M., 1994, Environmental Limits on Net Primary Production and Light-Use Efficiency Across the Oregon Transect: *Ecological Applications*, v. 4, p. 226–237, doi: 10.2307/1941929.
- Sarna-Wojcicki, A.M., Champion, D.E., and Davis, J.O., 1983, Holocene volcanism in the conterminous United States and the role of silicic volcanic ash layers in correlation of latest-Pleistocene and Holocene deposits: *Late Quaternary environments of the United States*, v. 2, p. 52–77.
- Saunders, I., and Young, A., 1983, Rates of surface processes on slopes, slope retreat and denudation: *Earth Surface Processes and Landforms*, v. 8, p. 473–501, doi: 10.1002/esp.3290080508.
- Schaller, M., Blanckenburg, F. von, Hovius, N., Veldkamp, A., van den Berg, M.W., and Kubik, P.W., 2004, Paleocorrosion Rates from Cosmogenic ^{10}Be in a 1.3 Ma Terrace Sequence: Response of the River Meuse to Changes in Climate and Rock Uplift: *The Journal of Geology*, v. 112, p. 127–144, doi: 10.1086/381654.

- Schaller, M., and Ehlers, T.A., 2006, Limits to quantifying climate driven changes in denudation rates with cosmogenic radionuclides: *Earth and Planetary Science Letters*, v. 248, p. 153–167, doi: 10.1016/j.epsl.2006.05.027.
- Schumer, R., Jerolmack, D., and McElroy, B., 2011, The stratigraphic filter and bias in measurement of geologic rates: *Geophysical Research Letters*, v. 38, p. n/a–n/a, doi: 10.1029/2011GL047118.
- Slim, M., Perron, J.T., Martel, S.J., and Singha, K., 2015, Topographic stress and rock fracture: a two-dimensional numerical model for arbitrary topography and preliminary comparison with borehole observations: *Earth Surface Processes and Landforms*, v. 40, p. 512–529, doi: 10.1002/esp.3646.
- Small, E.E., Anderson, R.S., and Hancock, G.S., 1999, Estimates of the rate of regolith production using and from an alpine hillslope: *Geomorphology*, v. 27, p. 131–150, doi: 10.1016/S0169-555X(98)00094-4.
- Smith, D.J., 1992, Long-term rates of contemporary solifluction in the Canadian Rocky Mountains: *Periglacial Geomorphology*. Wiley, Chichester, p. 203–221.
- Snively, P.D., Wagner, H.C., and MacLeod, N.S., 1964, Rhythmic-bedded eugeosynclinal deposits of the Tyee formation, Oregon Coast Range: *Kansas Geological Survey Bulletin*, v. 169, p. 461–480.
- Stock, J.D.J., and Dietrich, W.E., 2006, Erosion of steepland valleys by debris flows: *Geological Society of America ...*, v. 118, p. 1125–1148, doi: 10.1130/B25902.1.
- Sweeney, K.E., Roering, J.J., Almond, P., and Reckling, T., 2012, How steady are steady-state landscapes? Using visible-near-infrared soil spectroscopy to quantify erosional variability: *Geology*, v. 40, p. 807–810, doi: 10.1130/G33167.1.
- Tucker, G.E., McCoy, S.W., Whittaker, A.C., Roberts, G.P., Lancaster, S.T., and Phillips, R., 2011, Geomorphic significance of postglacial bedrock scarps on normal-fault footwalls: *Journal of Geophysical Research: Earth Surface*, v. 116, p. n/a–n/a, doi: 10.1029/2010JF001861.
- Tucker, G.E., and Slingerland, R., 1997, Drainage basin responses to climate change: *Water Resources Research*, v. 33, p. 2031–2047, doi: 10.1029/97WR00409.
- Vasconcelos, P.M., Brimhall, G.H., Becker, T.A., and Renne, P.R., 1994, analysis of supergene jarosite and alunite: Implications to the paleoweathering history of the western USA and West Africa: *Geochimica et Cosmochimica Acta*, v. 58, p. 401–420, doi: 10.1016/0016-7037(94)90473-1.
- Walder, J., and Hallet, B., 1985, A theoretical model of the fracture of rock during freezing: *Geological Society of America Bulletin*, v. 96, p. 336–346, doi: 10.1130/0016-7606(1985)96.

- Whipple, K.X., 2001, Fluvial landscape response time: how plausible is steady-state denudation? *American Journal of Science*, v. 301, p. 313–325, doi: 10.2475/ajs.301.4-5.313.
- Wilkinson, M.T., and Humphreys, G.S., 2005, Exploring pedogenesis via nuclide-based soil production rates and OSL-based bioturbation rates: *Australian Journal of Soil Research*, v. 43, p. 767, doi: 10.1071/SR04158.
- Willett, S., McCoy, S., Perron, J., Goren, L., and Chen, C., 2014, Dynamic Reorganization of River Basins: *Science*,.
- Worona, M.A., and Whitlock, C., 1995, Late Quaternary vegetation and climate history near Little Lake, central Coast Range, Oregon: *Geological Society of America Bulletin*, v. 107, p. 867–876, doi: 10.1130/0016-7606(1995)107.
- Yoo, K., Amundson, R., Heimsath, A.M., and Dietrich, W.E., 2005, Process-based model linking pocket gopher (*Thomomys bottae*) activity to sediment transport and soil thickness: *Geology*, v. 33, p. 917–920, doi: 10.1130/G21831.1.
- Zhang, P., Molnar, P., and Downs, W.R., 2001, Increased sedimentation rates and grain sizes 2-4 Myr ago due to the influence of climate change on erosion rates.: *Nature*, v. 410, p. 891–7, doi: 10.1038/35073504.